5-18-2007

Embedded Multilayer Thin Film Stacks as Polarizing Beam Splitters and Wave Retarders Operating under Condition of Frustrated Total Internal Reflection

Perla Siva Reddy
University of New Orleans

Embedded Multilayer Thin Film Stacks as Polarizing Beam Splitters and Wave Retarders Operating under Condition of Frustrated Total Internal Reflection

A Dissertation

Submitted to the Graduate Faculty of the
University of New Orleans
in partial fulfillment of the
requirements for the degree of

Doctor of Philosophy
in
Engineering and Applied Science
Electrical Engineering

by

Siva Reddy Perla

B. Tech. Jawaharlal Nehru Technological University, 2001
M. S. University of New Orleans, 2003

May, 2007

ACKNOWLEDGEMENTS

I would like to express my sincere gratitude towards my major professor Dr. Rasheed M. A. Azzam for his constant encouragement and invaluable guidance throughout my research career for the past 5 years. I would like to thank Dr. D. Charalampidis, Dr. A. Alsamman, Dr. J. Ioup and Dr. A. Puri for serving as my dissertation committee members. Many thanks for the faculty of the Electrical Engineering department for their academic and financial assistance. Finally, I would like to thank my parents and my beloved sister Saritha for all the encouragement and support they provided throughout my life.

TABLE OF CONTENTS

List of Tables

List of Figures

Abstract

The polarization properties of embedded centro-symmetric and periodic multilayer stacks under conditions of frustrated total internal reflection (FTIR) are considered. The centro-symmetric multilayer stack consists of a high-index center layer sandwiched between two identical low-index films and high-index – low-index bilayers repeated on both sides of the central trilayer maintaining the symmetry of the entire stack. The periodic multilayer consists of periodically repeated low-index – high-index bilayers. Each multilayer stack is embedded in a high-index prism.

Embedded centro-symmetric multilayer stacks are designed to function as efficient polarizers or polarizing beam splitters (PBSs) under conditions of FTIR over an extended range of incidence angles. For a given set of refractive indices, all possible solutions for the thicknesses of the layers that suppress the reflection of *p*-polarized light at a specified angle, and the associated reflectance of the system for the orthogonal *s* polarization, are determined. The angular and spectral sensitivities of polarizing multilayer stacks employing 3, 7, 11, 15 and 19 layers of BaF_2 and PbTe thin films embedded in a ZnS prism, operating at $\lambda = 10.6$ μm, are presented.

Embedded centro-symmetric multilayer stacks are also designed to function as complete-transmission quarter-wave or half-wave retardation (QWR or HWR) devices under conditions of FTIR. QWR and HWR designs at $\lambda = 1.55\ \mu m$ are presented that employ 11 and 7 layers of Si and SiO_2 thin films embedded in GaP and Si cube prisms, respectively. The angular and spectral sensitivities of these devices are also considered. Embedded centro-symmetric multilayer stacks under FTIR conditions are also designed to produce various 50%-50% beam splitters.

Embedded periodic multilayer stacks are designed to function as polarizers and PBSs at discrete multiple angles of incidence and wavelengths under condition of FTIR. For a given set of refractive indices, all possible solutions for the thicknesses of the layers that suppress the reflection of *p*-polarized light at a specified angle, and the associated reflectance of the system for the orthogonal *s* polarization, are determined. The angular and spectral sensitivities of polarizing multilayer stacks employing 4, 6, 8, 10, 12, 14, 16 and 18 layers of BaF_2 and PbTe thin films embedded in a ZnS prism, operating at $\lambda = 10.6\ \mu$m, are presented.

1. Introduction

Polarizers or polarizing beam splitters (PBS) and phase retarders are widely used in many applications in optics. An ideal linear polarizer is a device that transforms any state of polarization of light at its input to a linear state at its output. In polarizers either the transmitted or reflected light is used, whereas in PBS both the transmitted and reflected beams are utilized and both gain importance. Phase retarders are optical components that modify the state of polarization of light by introducing a specific differential phase shift between two orthogonal linear polarizations, without significantly affecting their relative amplitudes. QWR and HWR devices are of particular interest because incident linearly polarized light at an appropriate azimuth experiences $\pi/2$ or π phase shifts and emerges as circularly polarized light or linearly polarized light at a negative azimuth, respectively. The physical mechanisms by which polarizing action can be achieved are 1) thin film interference, and 2) other mechanisms like birefringence, dichroism, reflection, etc. A thin-film structure with alternate high- and low-index films, all one-quarter-wave thick, is widely used as a PBS. At oblique incidence selective polarization-dependent interference phenomenon takes place in these films. The low-index layers enhance the reflection of one linear polarization while the high-index layers act as phase adjusters. Thus high efficiency PBS and phase retarders are achieved using optical interference coatings.

In this work we show that high efficiency PBS and wave retarders can be achieved using frustrated total internal reflection (FTIR) by centro-symmetric and periodic multilayer stacks embedded in a high-index prism. Section 2 gives a brief review of literature. The procedure for designing PBS and wave retarders is detailed in Section 3. The results for the spectral and angular sensitivities of the PBS and wave retarders are presented in Section 4. Finally, Section 5 gives a brief summary of this work.

2. Review of Literature

2.1 Polarizing Beam Splitters

Thin film polarizers and polarizing beam splitters (PBS) are widely known[1-8] and are based on the destructive interference of light for one linear polarization (*p* or *s*) and the nearly fully constructive interference for the orthogonal polarization. The most important performance characteristics of a polarizer or a PBS are its spectral range, angular range, extinction ratios, and the transmittance or reflectance for the desired polarization. Considerable progress has recently been made in the design of broadband, wide-angle, polarizers and PBS. Mouchart[9] *et al*. showed that it is possible to broaden the angular field of MacNeille polarizers[10,11] at the expense of reducing the spectral bandwidth. Li and Dobrowolski[12] proposed a new method for the design of broadband and wide-angle visible PBS's based on the use of more than two materials. In a recent paper[13] (which is a major reference for this work) Li and Dobrowolski reviewed the earlier literature of polarizers and proposed a new high-performance PBS that employs FTIR and reflects the *p* polarization and transmits the *s* polarization. (In the conventional MacNeille design,[9,10] that operates at Brewster's angle the *p* polarization is transmitted and the *s* polarization is reflected.). The multilayer consists of a large number (27-81) of very thin films embedded in a high index prism. In this work we use two different types of multilayer structures: (I) a centro-symmetric multilayer stack (similar to that in Ref. 13) and (II) periodic multilayer stack. Also instead of using Herpin's equivalent-layer theory,[14,15] an explicit technique is introduced which is based on the full expressions of the complex-amplitude reflection coefficients of the multilayer structure. We also allow for either the *p* or *s* polarization to be reflected or transmitted and we do not resort to the very thin film approximation used in Ref. 13.

2.2 Wave Retarders

Quarter-wave and half-wave retarders (QWR and HWR) are widely used for the control and analysis of polarized light with numerous applications.[16,17] The desired differential phase shift between two orthogonal linear polarizations is commonly obtained when light is transmitted through a natural crystalline or form-birefringent plate, or in total internal reflection in the presence or absence of thin films.[18-22] External reflection retarders that use transparent single or multilayer thin films on a high-reflectance substrate have also been introduced.[23-28]

Previously, transparent multilayer thin films deposited on a transparent substrate were designed to function as quarter-wave plates in transmission at oblique incidence in air.[29] Quarter-wave differential phase shift can also be obtained in transmission through a tilted bilayer membrane with unequal throughput for the *p* and *s* polarizations at a high angle of incidence.[30] FTIR beam splitters that function as dual QWR in reflection and transmission using an embedded single layer or symmetric trilayer have also been reported recently.[31,32]

In this work we demonstrate that frustrated total internal reflection by a transparent centro-symmetric multilayer stack which is embedded in a high-index prism can function as: (1) quarter-wave retarder or half-wave retarder with high (near 100 %) transmission, good spectral response (over a 100-nm bandwidth in the near IR), and limited angular sensitivity, and (2) 50%-50% beam splitter achieving (a) no change of polarization in reflection and transmission, (b) no change of polarization in reflection and half-wave retardation in transmission, (c) HWR in reflection and no change of polarization in transmission, (d) HWR in reflection and transmission, (e) opposite quarter-wave retardation in reflection and transmission, and (f) same QWR in reflection and transmission. The spectral and angular sensitivities of some of these devices are also considered.

3. Design Procedure

3.1 Centro-symmetric multilayer stacks

The centro-symmetric multilayer stack, Figs. 1, 2 and 3, consists of a high-index center layer of refractive index n_2 sandwiched between two identical low-index films of refractive index n_1 and high-index – low-index ($n_2 - n_1$) bilayers repeated on both sides of the central trilayer maintaining the symmetry of the entire stack which is itself embedded in a high-index prism of refractive index n_0. All media are considered to be transparent, optically isotropic, and are separated by parallel-plane boundaries. We assume that $n_0 > n_1$, $n_2 \geq n_0$ and that light is incident from medium 0 at an angle ϕ_o which is greater than the critical angle [$\phi_{c01} = \arcsin(n_1/n_0)$] of the 01 interface, so that frustrated total internal reflection takes place.

Consider a monochromatic light beam traveling in an ambient medium (high-index prism) of refractive index n_0 and incident on an embedded centro-symmetric multilayer structure at an angle of incidence ϕ_0 with respect to the normal to the interfaces as shown in Figs. 1, 2 and 3. The complex-amplitude transmission and reflection coefficients T_ν and R_ν ($\nu = p, s$) of the multilayer stack for the *p* and *s* polarizations at an internal angle of incidence ϕ_0 are determined by the scattering matrix method[16]. A general expression for the complex-amplitude reflection coefficient (R_ν) for an *m*-layer centro-symmetric multilayer stack embedded in a high-index prism, as shown in Figs. 1, 2 and 3, can be expressed as:

$$R_\nu = \frac{a_n X_2^n + a_{n-1} X_2^{n-1} + \ldots + a_0}{b_n X_2^n + b_{n-1} X_2^{n-1} + \ldots + b_0}, \qquad (1)$$
$$\nu = p, s.$$

In Eq. (1) $n = (m\text{-}1)/2$, and $a_n, a_{n-1}, \ldots a_0; b_n, b_{n-1}, \ldots b_0$ are functions of the Fresnel interface reflection coefficients $r_{01v}, r_{12v},$ and X_1. X_1 and X_2 are complex exponential functions of film thickness given by

$$X_i = \exp(-j\pi Z_i \cos\phi_i), \tag{2}$$

where Z_i is the thickness of the i^{th} film normalized to the quarter-wave thickness at normal incidence, i.e,

$$Z_i = \frac{4 d_i n_i}{\lambda} \tag{3}$$

In Eq. (2) ϕ_i is the angle of refraction in the i^{th} layer, and in Eq. (3) n_i, d_i are the refractive index and metric thickness of the i^{th} layer, respectively, and λ is the vacuum wavelength of light.

The Fresnel complex-amplitude reflection coefficients of the *ij* interface for the *p* and *s* polarizations are given by[16]:

$$r_{ijp} = \frac{n_j \cos\phi_i - n_i \cos\phi_j}{n_j \cos\phi_i + n_i \cos\phi_j}, r_{ijs} = \frac{n_i \cos\phi_i - n_j \cos\phi_j}{n_i \cos\phi_i + n_j \cos\phi_j}. \tag{4}$$

When the refractive indices and angle of incidence are such that $n_1/n_0 < \sin\phi_0$, FTIR takes place at the 01 interface at ϕ_0 and the light field becomes evanescent in medium 1 (the low-index film). In this case, $\cos\phi_1$ is pure imaginary, and X_1 is real in the range $0 \le X_1 \le 1$. Because we

also choose $n_2 \geq n_0$, the angle of refraction ϕ_2 in the high-index layers is real, which makes X_2 a pure phase factor, so that $|X_2| = 1$.

3.1.1 Centro-symmetric multilayer stacks as PBS

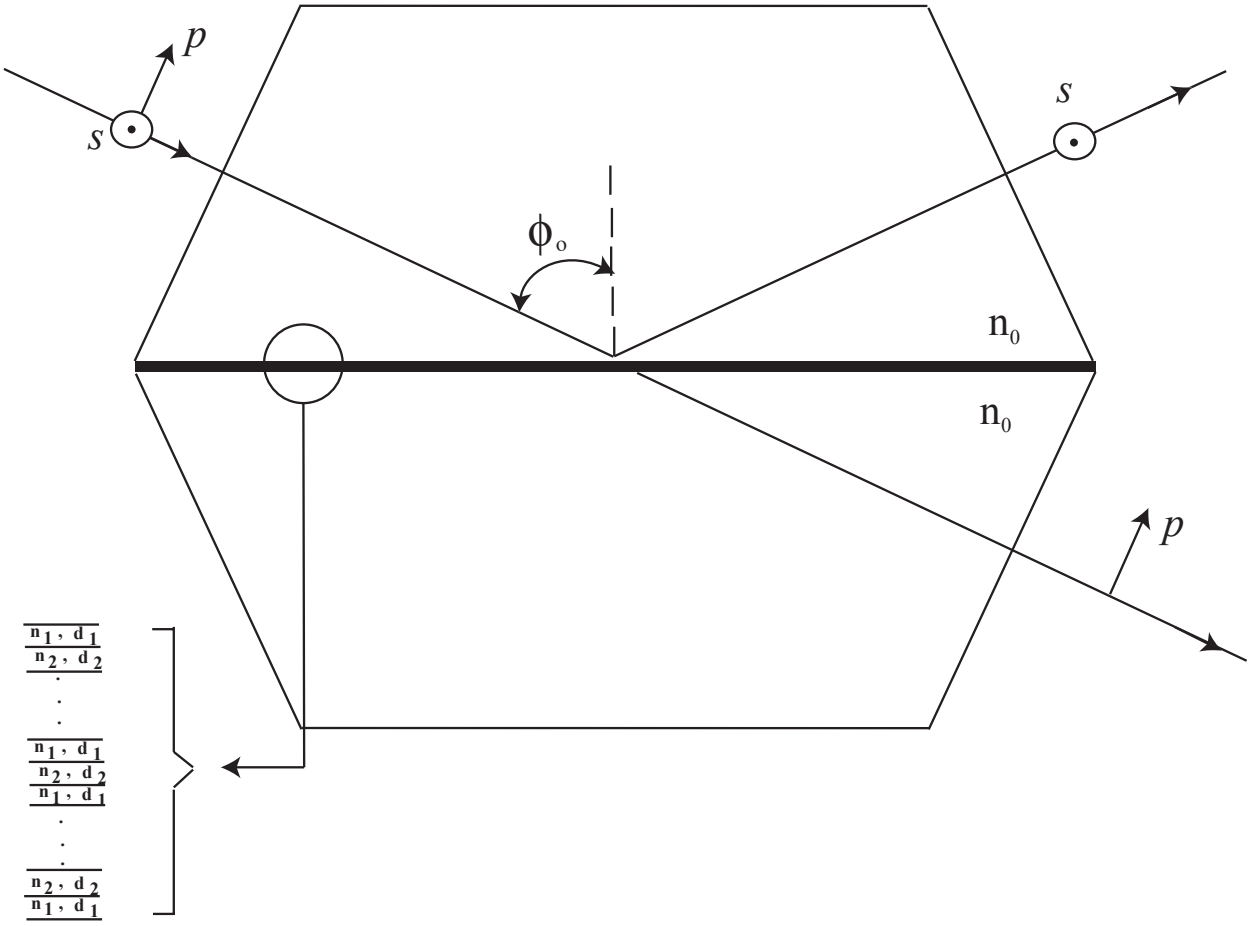

Figure 1 Embedded centro-symmetric multilayer thin-film device as polarizing beam splitter (PBS) operating under conditions of frustrated total internal reflection. *p* and *s* are the linear polarizations parallel and perpendicular to the plane of incidence, respectively, and ϕ_0 is the angle of incidence.

To suppress the ν polarization on reflection, we set $R_\nu = 0$ in Eq. (1) which gives

$$a_n X_2^n + a_{n-1} X_2^{n-1} + ... + a_0 = 0 \qquad (5)$$

Depending on the order *n* of the polynomial in Eq. (5) multiple roots for X_2 are obtained for designs with number of layers $m > 3$, corresponding to multiple solutions sets (X_1, X_2) that suppress the *v* polarization.

When the refractive indices and angle of incidence are such that $n_1/n_0 < \sin\phi_0$, FTIR takes place at the 01 interface at ϕ_0 and the light field becomes evanescent in medium 1 (the low-index film). In this case, $\cos\phi_1$ is pure imaginary, and X_1 is real in the range $0 \le X_1 \le 1$. Because we also choose $n_2 \ge n_0$, the angle of refraction ϕ_2 in the high-index layers is real, which makes X_2 a pure phase factor, so that $|X_2| = 1$. For each real value of X_1 in the range $0 \le X_1 \le 1$, we find that $|X_2| = 1$ for each root of Eq. (5). Therefore, there are infinite number of solution sets (X_1, X_2) that satisfy Eq. (5), so that $R_\nu = 0$. The corresponding solution sets of normalized film thicknesses (Z_1, Z_2) are determined subsequently using Eq. (2).

An acceptable design must have a high reflectance $R_{\nu'} = |R_\nu|^2$ for the unsuppressed orthogonal polarization ν'. In general, this reflectance increases as the normalized thickness Z_1 (of the low-index layers that support the evanescent field) and the angle of incidence ϕ_0 are increased.

3.1.2 Centro-symmetric multilayer stacks as complete transmission QWR and HWR devices

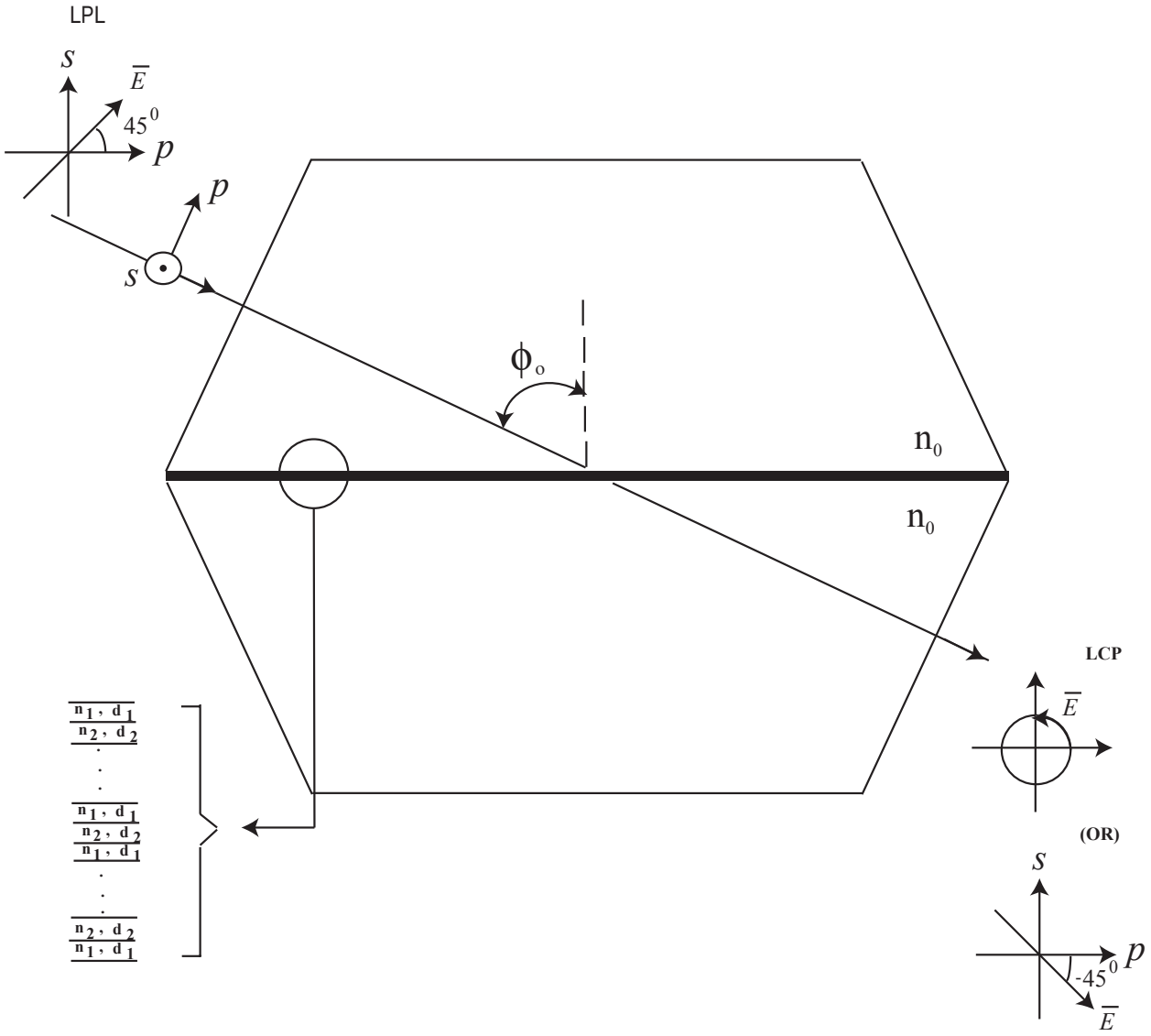

Figure 2 Embedded multilayer thin-film transmission device that operates under conditions of frustrated total internal reflection. *p* and *s* are the linear polarizations parallel and perpendicular to the plane of incidence, respectively, and ϕ_0 is the angle of incidence. This complete-transmission QWR or HWR transforms incident linearly polarized light (LPL) at 45° azimuth into circularly polarized light (CPL), or linearly polarized light at -45°azimuth, respectively, depending on the parameters of the multilayer stack and angle of incidence.

The complex-amplitude transmission and reflection coefficients T_ν and R_ν $(\nu = p,s)$ of the multilayer stack for the *p* and *s* polarizations at an internal angle of incidence ϕ_0 are determined by the scattering matrix method[16]. To achieve QWR and HWR with essentially complete transmission for the *p* and *s* polarizations, the following equations

$$T_p \pm jT_s = 0, \text{ (QWR)} \tag{6}$$

$$T_p + T_S = 0, \text{(HWR)} \tag{7}$$

are solved (by numerical iteration) subject to the constraint that

$$\left|R_p\right|^2 = \left|R_s\right|^2 \approx 0. \tag{8}$$

For an all-transparent structure, the condition

$$\left|R_\nu\right|^2 + \left|T_\nu\right|^2 = 1, \nu = p,s, \tag{9}$$

is satisfied. In our thin film optics calculations we follow the Nebraska (Muller) conventions.[33] In evaluating the Fresnel interface reflection coefficients for the *p* and *s* polarizations and the complex exponential functions of film thickness, only physically meaningful square roots should be selected to avoid erroneous results.[34,35]

3.1.3 Centro-symmetric multilayer stacks as 50%-50% beam splitters (BS)

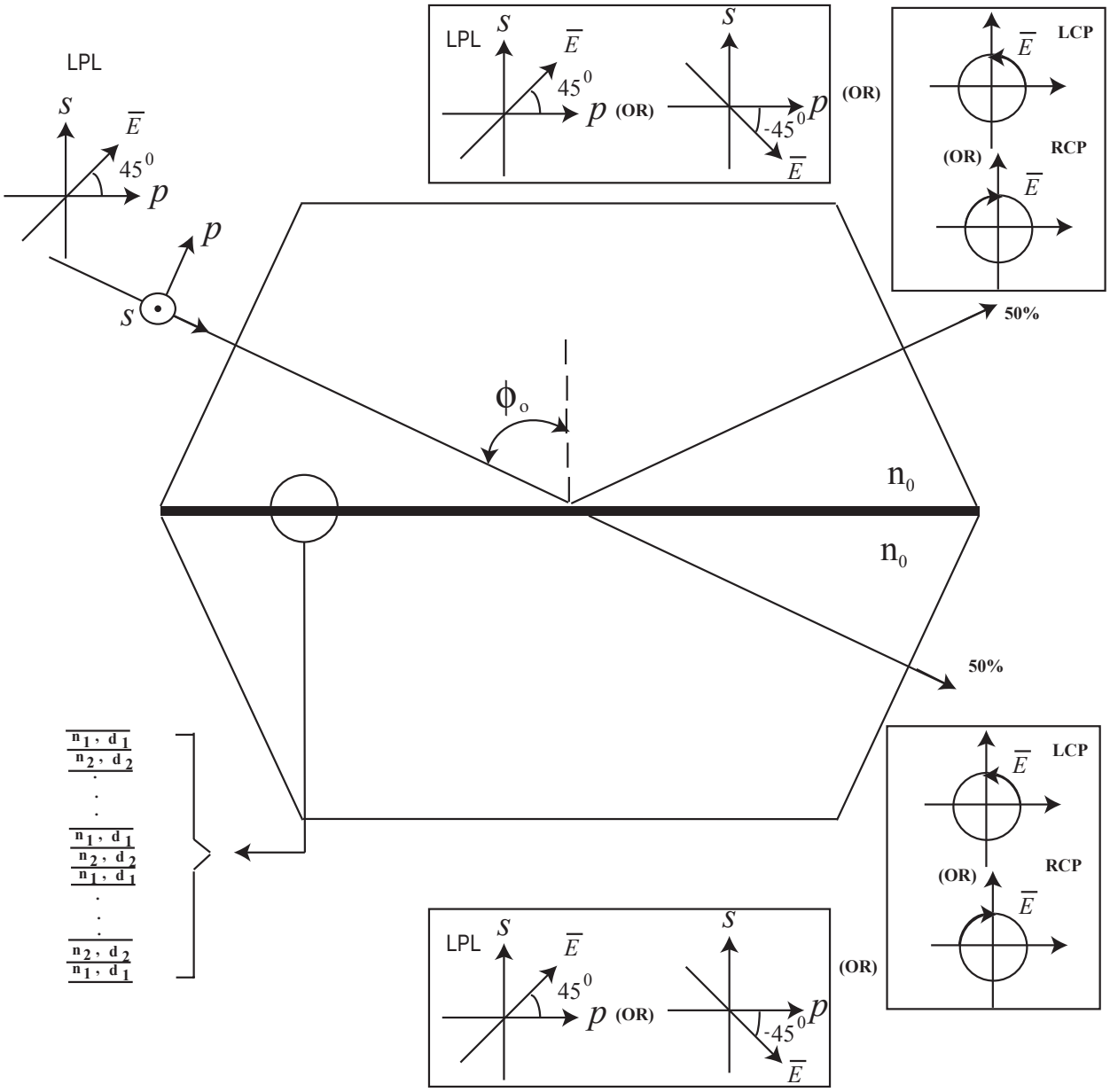

Figure 3 Embedded multilayer thin-film 50%-50% beam splitter operating under conditions of FTIR. *p* and *s* are the linear polarizations parallel and perpendicular to the plane of incidence, respectively, and ϕ_0 is the angle of incidence. This 50%-50% beam splitter transforms incident linearly polarized light (LPL) at 45° azimuth into circularly polarized light (CPL) of opposite or same handedness, or linearly polarized light at +45° or -45°azimuth in reflected and transmitted beams and with equal throughput for the *p* and *s* polarizations, depending on the parameters of the multilayer stack and angle of incidence.

To achieve the list of retarders listed in Table 1 with equal throughput (50%-50%) for the *p* and *s* polarizations, the following equations:

$$R_p \mp R_s = 0, \text{ (PIBS, HWR)} \tag{10}$$

$$R_p \pm jR_s = 0, \text{ (QWR)} \tag{11}$$

are solved (by numerical iteration) subject to the following constraints:

$$\left|R_p\right|^2 = \left|R_s\right|^2 = \left|T_p\right|^2 = \left|T_s\right|^2 \approx 0.5 \tag{12}$$

and

$$\Delta_r = 0/180 \text{ (PIBS/HWR) and } \Delta_t = 0/180 \text{ (PIBS/HWR)} \tag{13}$$

(or)

$$\Delta_r = \pm 90/270 \text{ (QWR) and } \Delta_t = \pm\ 90/270 \quad \text{(QWR)} \tag{14}$$

When the refractive indices and angle of incidence are such that $n_1/n_0 < \sin\phi_0$, FTIR takes place at the 01 interface at ϕ_0 and the light field becomes evanescent in medium 1 (the low-index film). In this case, $\cos\phi_1$ is pure imaginary, and X_1 is real in the range $0 \le X_1 \le 1$. Because we also choose $n_2 \ge n_0$, the angle of refraction ϕ_2 in the middle layer is real, which makes X_2 a pure phase factor, so that $|X_2| = 1$. For each real value of X_1 in the range $0 \le X_1 \le 1$, we look for solutions (X_1, X_2) that satisfy Eqs. (10) or (11) subject to the constraints in Eqs. (12) and (13) or Eqs. (12) and (14), respectively, such that $|X_2| = 1$. Depending on the order *n* of the numerator polynomials in Eqs. (10) or (11) multiple roots for X_2 are obtained. The corresponding solution

sets of normalized film thicknesses (Z_1, Z_2) are determined subsequently using Eq. (3). For the results presented in Section 4.3, the solution set (X_1, X_2) that satisfied Eqs. (10) or (11) with the best numerical accuracy was chosen.

Table 1. List of various 50%-50% beam splitters

$\Delta_r = (\Delta_{rp} - \Delta_{rs})$	$\Delta_t = (\Delta_{tp} - \Delta_{ts})$
0	0
0	180^o
180^o	0
180^o	180^o
$\pm 90^o/270^o$	$\pm 90^o/270^o$

3.2 Periodic multilayer stacks

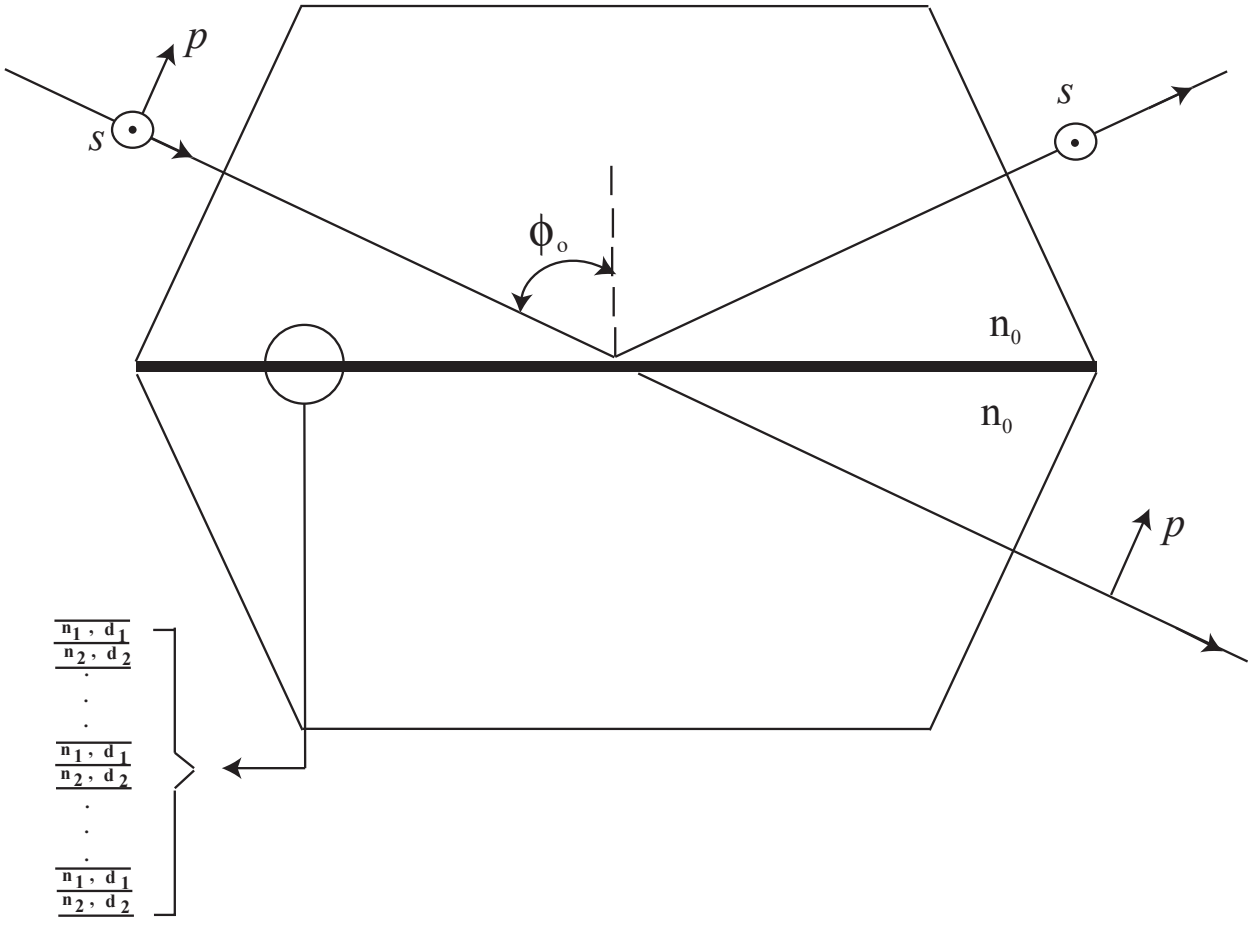

Figure 4 Embedded periodic multilayer thin-film device as polarizing beam splitter (PBS) operating under conditions of frustrated total internal reflection. *p* and *s* are the linear polarizations parallel and perpendicular to the plane of incidence, respectively, and ϕ_0 is the angle of incidence.

The multilayer PBS, Fig. 4, consists of periodically repeated low-index (n_1) – high-index (n_2) bilayers embedded in a high-index prism of refractive index n_0. All media are considered to be transparent, optically isotropic, and separated by parallel-plane boundaries. We assume that $n_0 > n_1$, $n_2 \geq n_0$ and that light is incident from medium 0 at an angle of ϕ_0 which is greater than the critical angle [$\phi_{c01} = \arcsin(n_1/n_0)$] of the 01 interface, so that frustrated total internal reflection takes place.

Consider a monochromatic light beam traveling in an ambient medium (high-index prism) of refractive index n_0 and incident on an embedded periodic multilayer structure at an angle of incidence ϕ_0 with respect to the normal to the interfaces, as shown in Fig. 4. The complex-amplitude transmission and reflection coefficients T_ν and R_ν ($\nu = p, s$) of the multilayer stack for the p and s polarizations at an internal angle of incidence ϕ_0 are determined by the scattering matrix method[16]. A general expression for the complex-amplitude reflection coefficient (R_ν) for an m- layer periodic multilayer stack with a bilayer as a period embedded in a high-index prism, as shown in Fig. 4, can be expressed as:

$$R_\nu = \frac{a_n X_2^n + a_{n-1} X_2^{n-1} + \ldots + a_0}{b_n X_2^n + b_{n-1} X_2^{n-1} + \ldots + b_0}, \qquad (15)$$
$$\nu = p, s.$$

In Eq. (15) n = m/2, and a_n, a_{n-1},… a_0; b_n, b_{n-1}, … b_0 are functions of the Fresnel interface reflection and transmission coefficients $r_{01\nu}$, $r_{12\nu}$, $r_{20\nu}$ and X_1. X_1 and X_2 are complex exponential functions of film thickness given by:

$$X_i = \exp(-j\pi Z_i \cos\phi_i), \tag{16}$$

where Z_i is the thickness of the i^{th} film normalized to the quarter-wave thickness at normal incidence, i.e,

$$Z_i = \frac{4d_i n_i}{\lambda}. \tag{17}$$

In Eq. (16) ϕ_i is the angle of refraction in the i^{th} layer, and in Eq. (17) n_i, d_i are the refractive index and metric thickness of the i^{th} layer, respectively, and λ is the vacuum wavelength of light. The Fresnel complex-amplitude reflection and transmission coefficients of the *ij* interface for the *p* and *s* polarizations are given by[16]:

$$r_{ijp} = \frac{n_j \cos\phi_i - n_i \cos\phi_j}{n_j \cos\phi_i + n_i \cos\phi_j},\ r_{ijs} = \frac{n_i \cos\phi_i - n_j \cos\phi_j}{n_i \cos\phi_i + n_j \cos\phi_j} \tag{18}$$

$$t_{ijp} = \frac{2n_i \cos\phi_i}{n_j \cos\phi_i + n_i \cos\phi_j},\ t_{ijs} = \frac{2n_i \cos\phi_i}{n_i \cos\phi_i + n_j \cos\phi_j}. \tag{19}$$

To suppress the ν polarization on reflection, we set $R_\nu = 0$ in Eq. (15) which gives

$$a_n X_2^n + a_{n-1} X_2^{n-1} + \ldots + a_0 = 0. \tag{20}$$

Depending on the order *n* of the polynomial in Eq. (20) multiple roots for X_2 are obtained for designs with number of layers $m > 2$, corresponding to multiple solutions sets (X_1, X_2) that suppress the *v* polarization. No solution set (X_1, X_2) exists that satisfies Eq. (20) for $m = 2$.

When the refractive indices and angle of incidence are such that $n_1/n_0 < \sin\phi_0$, FTIR takes place at the 01 interface at ϕ_0 and the light field becomes evanescent in medium 1 (the low-index film). In this case, $\cos\phi_1$ is pure imaginary, and X_1 is real in the range $0 \le X_1 \le 1$. Because we also choose $n_2 \ge n_0$, the angle of refraction ϕ_2 in the high-index layers is real, which makes X_2 a pure phase factor, so that $|X_2| = 1$. For each real value of X_1 in the range $0 \le X_1 \le 1$, we find that $|X_2| = 1$ for (n-1) roots of Eq. (20). Therefore, there are infinite number of solution sets (X_1, X_2) that satisfy Eq. (20), so that $R_\nu = 0$. The corresponding solution sets of normalized film thicknesses (Z_1, Z_2) are determined subsequently using Eq. (17).

An acceptable design must have a high reflectance $R_{\nu'} = |R_{\nu'}|^2$ for the unsuppressed orthogonal polarization ν'. In general, this reflectance increases as the normalized thickness Z_1 (of the low-index layers that support the evanescent field) and the angle of incidence ϕ_0 are increased.

4. Results

4.1 Centro-symmetric multilayer stacks as PBS

Various multilayer designs obtained by solving Eq. (5), their angular and spectral sensitivities are presented here. Figures 5, 6 and 7 show Z_2 versus Z_1 such that $R_p = 0$ at angles of incidence ϕ_0 from 45° to 55° in steps of 1° for various centro-symmetric multilayer stacks with 3, 7, 11, 15 and 19 layers of BaF_2 and PbTe thin films embedded in a Cleartran[36] (ZnS) prism.

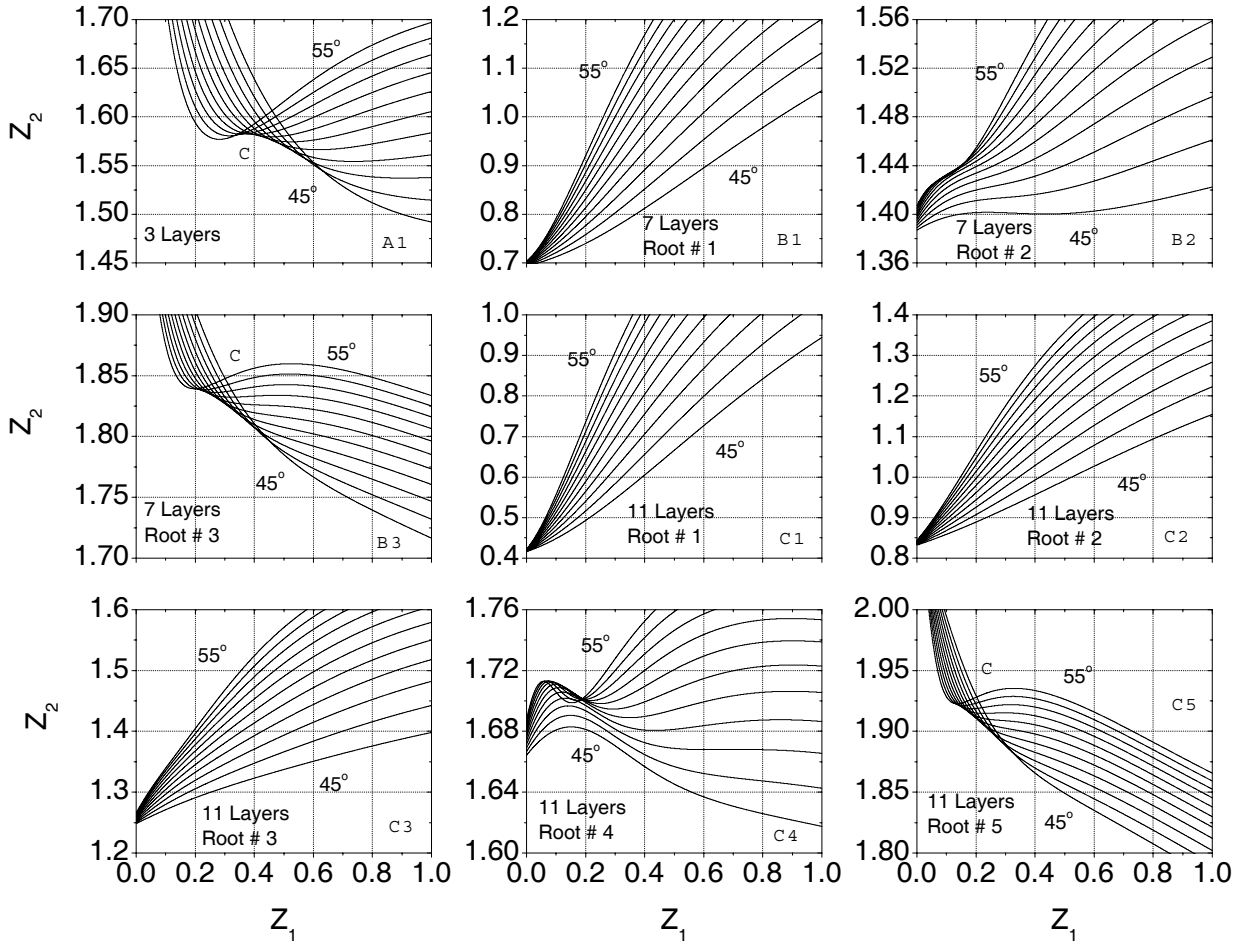

Figure 5 Z_2 versus Z_1 such that $R_p = 0$ at angles of incidence ϕ_0 from 45° to 55° in steps of 1° for centro-symmetric multilayer stacks with BaF_2 and PbTe thin films embedded in a ZnS substrate with refractive indices $n_0 = 2.1919$ (ZnS), $n_1 = 1.3926$ (BaF_2), and $n_2 = 5.6314$ (PbTe) in the IR at $\lambda = 10.6$ μm. Panel A1 corresponds to a trilayer design, Panels B1, B2 and B3 correspond to 7-layer design while Panels C1, C2, C3, C4 and C5 correspond to 11-layer design.

The refractive indices of ZnS (n_0 = 2.1919), BaF_2 (n_1 = 1.3926), and PbTe (n_2 = 5.6314) are calculated using published dispersion relations.[37] In Fig. 5, Panel A1 corresponds to the trilayer design with one root; Panels B1, B2 and B3 correspond to the 7-layer design with 3 roots, while Panels C1, C2, C3, C4 and C5 correspond to the 11-layer design with 5 roots.

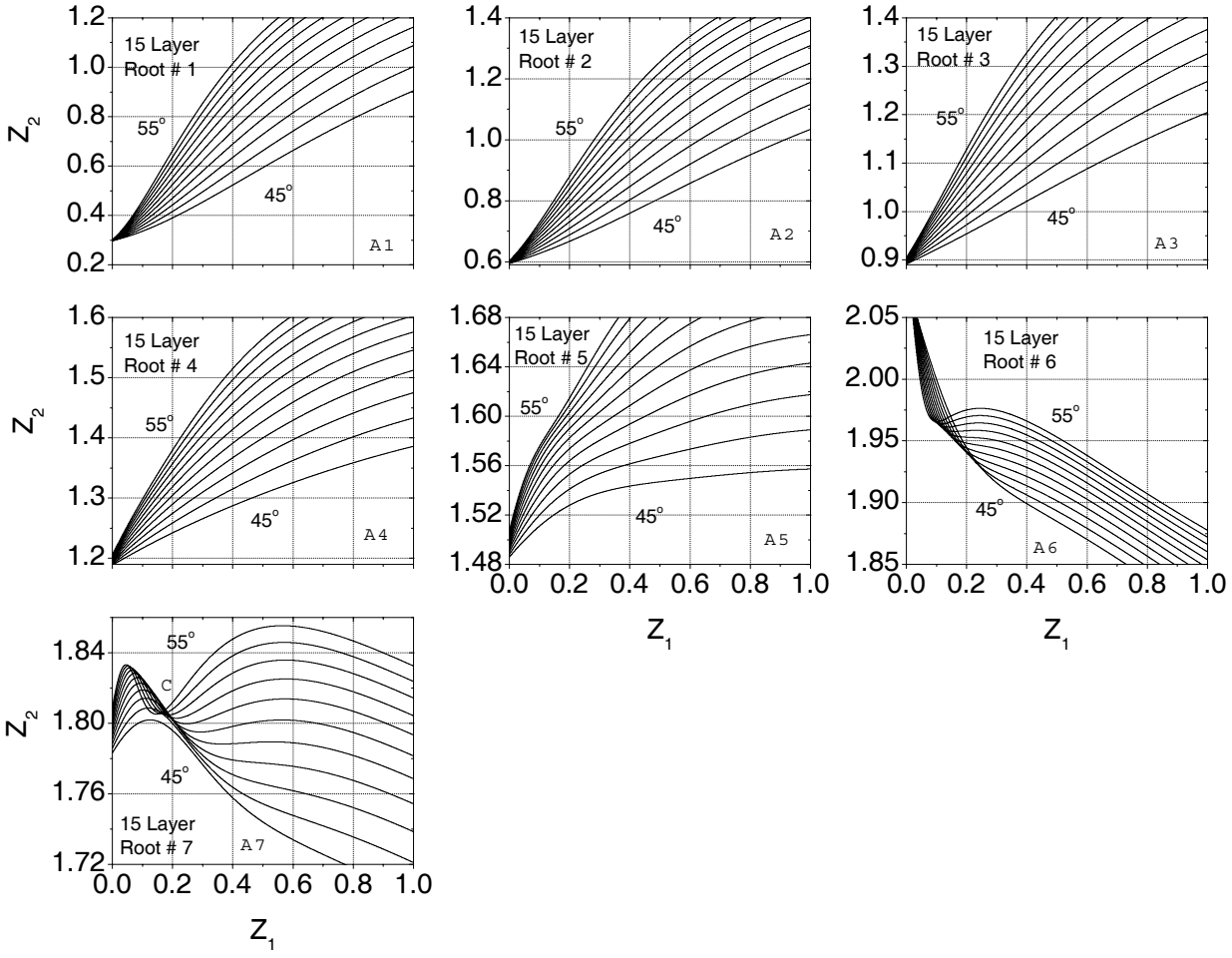

Figure 6 Z_2 versus Z_1 such that $R_p = 0$ at angles of incidence ϕ_0 from 45° to 55° in steps of 1° for the same material system as described in the caption of Fig. 5 for a 15-layer centro-symmetric design.

Figure 6 shows the corresponding results for the 15-layer design with 7 roots, while Fig. 7 shows the results for 19-layer design with 9 roots. Every point (Z_1, Z_2) on each curve in Figs. 5-7

represents a thickness solution that achieves a polarizer ($R_p = 0$) at the angle of incidence marked by that curve.

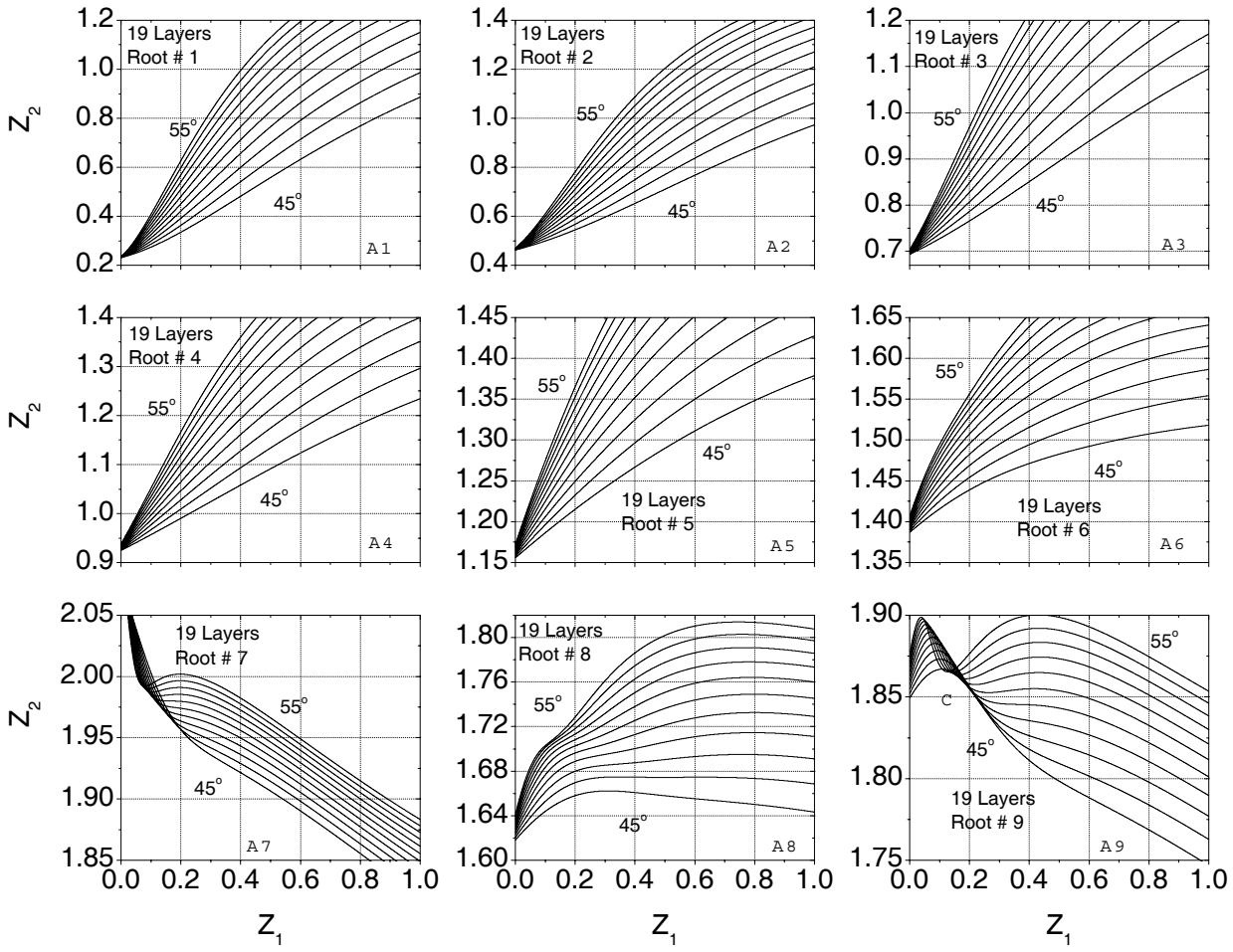

Figure 7 Z_2 versus Z_1 such that $R_p = 0$ at angles of incidence ϕ_0 from 45° to 55° in steps of 1° for the same material system as described in the caption of Fig. 5 for a 19-layer centro-symmetric design.

For designs with 3 to 19 layers, the Z_2-vs-Z_1 curves that correspond to some roots are clustered and mutually intersecting in a small region of the Z_2-vs-Z_1 plane. By selecting an intersection point (Z_1, Z_2) of two curves in this cluster we obtain an $R_p = 0$ polarizer at two angles of incidence simultaneously. For the results presented in Sections 4.1.1 and 4.1.2 we choose, for

each design with 3 to 19 layers, the intersection point of the 50° and 55° curves that correspond to the root with the highest root number (Panel A1 of Fig. 5, Panel B3 of Fig. 5, Panel C5 of Fig. 5, Panel A7 of Fig. 6, and Panel A9 of Fig. 7 for the 3, 7, 11, 15 and 19-layer designs, respectively). The point of intersection of the 50° and 55° curves for the root with the highest root number yields a design with $R_p \approx 0$ and high reflectance $|R_s|^2$ for all angles of incidence from 45° to 55°. Figures 5-7 are magnified so that the details are more apparent. Table 2 lists the normalized and metric film thicknesses (Z_1, Z_2) and (d_1, d_2) obtained by the above procedure for the 3, 7, 11, 15 and 19-layer designs.

Table 2 Normalized (Z_1, Z_2) and metric (d_1, d_2) thicknesses corresponding to the point of intersection of the 50° and 55° Z_2-vs-Z_1 curves in Panel A1 of Fig 5, Panel B3 of Fig. 5, Panel C5 of Figure 5, Panel A7 of Fig. 6, and Panel A9 of Fig. 7 for the 3, 7, 11, 15 and 19-layer designs, respectively.

# of Layers	Z_1	Z_2	d_1 (μm)	d_2 (μm)
3	0.377275	1.588134	0.71792	0.74734
7	0.234571	1.840903	0.44637	0.86628
11	0.188795	1.701440	0.35926	0.80066
15	0.173570	1.807341	0.33029	0.85049
19	0.149774	1.866958	0.28501	0.87855

4.1.1 Angular sensitivity

This specific comparison between different multilayer designs is based on the thickness solutions (Z_1, Z_2) ↔ (d_1, d_2) listed in Table 2. For the angle sensitivity, the metric film thicknesses (d_1, d_2) and wavelength λ = 10.6 μm for each multilayer design are kept constant and the angle of incidence ϕ_0 is varied from 46° to 56°. Panels A1 and A2 of Fig. 8 show a comparison between the extinction ratios in reflection and transmission (ER_r and ER_t in dB), respectively, as a function of angle of incidence ϕ_o for the 3, 7, 11, 15 and 19-layer designs. The 15- and the 19-layer designs achieve ER_r and ER_t > 30 dB over a 10° internal field of view (from 46° to 56°).

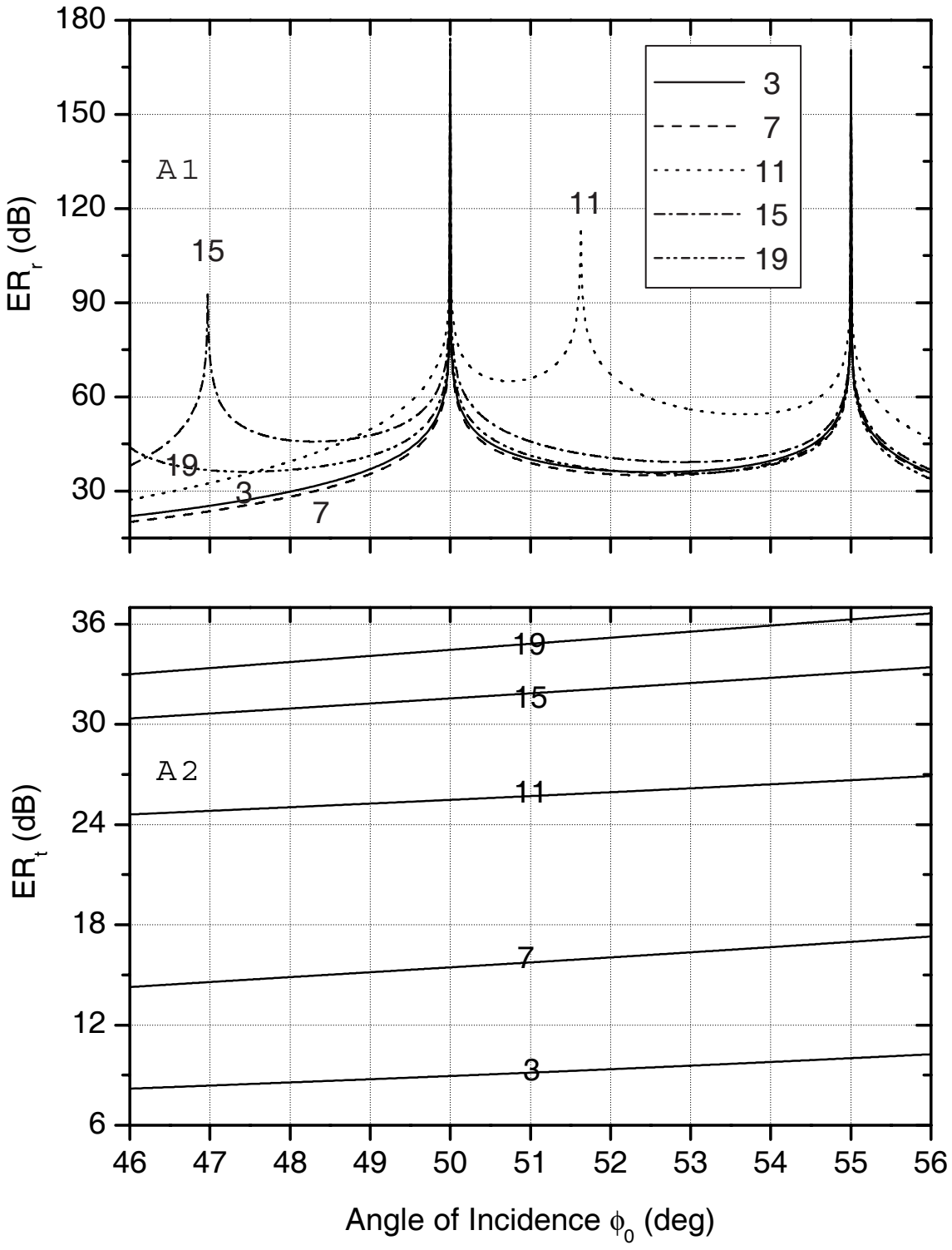

Figure 8 Extinction ratios in reflection and transmission (ER_r and ER_t) in dB for various centro-symmetric multilayer stacks with 3-19 layers embedded in a ZnS substrate are plotted versus the angle of incidence ϕ_0 from 46^o to 56^o. The material system is the same as given in the caption of Fig. 5 and the metric film thicknesses associated with different multilayer stack designs are listed in Table 2.

If one accounts for the refraction of light from air to the high-index ZnS substrate, the angular bandwidth in air is more than double that indicated in Fig. 8. The extinction ratio ER_r is > 150 dB at 50° and 55° for all designs because each thickness solution set corresponds to (Z_1 ,Z_2) at the point of intersection of the 50° and 55° curves. Table 3 lists the discrete angles at which ER_r in Panel A1 of Fig. 8 reaches a peak.

Table 3 Discrete angles at which the extinction ratio in reflection (ER_r) reaches a peak in Panel A1 of Fig. 8.

# of Layers	ϕ_0 (deg)	ER_r (dB)	ER_t (dB)
3	50°	162	8.9
	55°	168	10
7	50°	168	15.4
	55°	168	16.9
11	50°	180	25.4
	51.63°	114	25.8
	55°	170	26.6
15	46.97°	92	30.6
	50°	173	31.5
	55°	171	33.1
19	50°	161	34.4
	55°	159	36.2

Panels A1, A2, A3, A4 and A5 of Fig. 9 show the intensity reflectances $|R_p|^2$ and $|R_s|^2$ as a function of the angle of incidence ϕ_0 from 46° to 56° for 3-, 7-, 11-, 15- and 19-layer designs, respectively. All the parameters in this plot correspond to those in Fig. 8. As the number of layers increase, $|R_s|^2$ increases from 84% to 99.98% while $|R_p|^2$ remains < 0.01 over a 10° internal field of view (46° to 56°). The 15-layer design achieves $|R_p|^2 < 0.00025$ and $|R_s|^2 > 0.999$ while the 19-layer design achieves $|R_p|^2 < 0.0005$ and $|R_s|^2 > 0.9995$ over a 10° field of view (from 46° to 56°). Hence good PBS with high extinction ratios (> 30 dB) in both reflection and transmission are achieved over a good range of incidence angles.

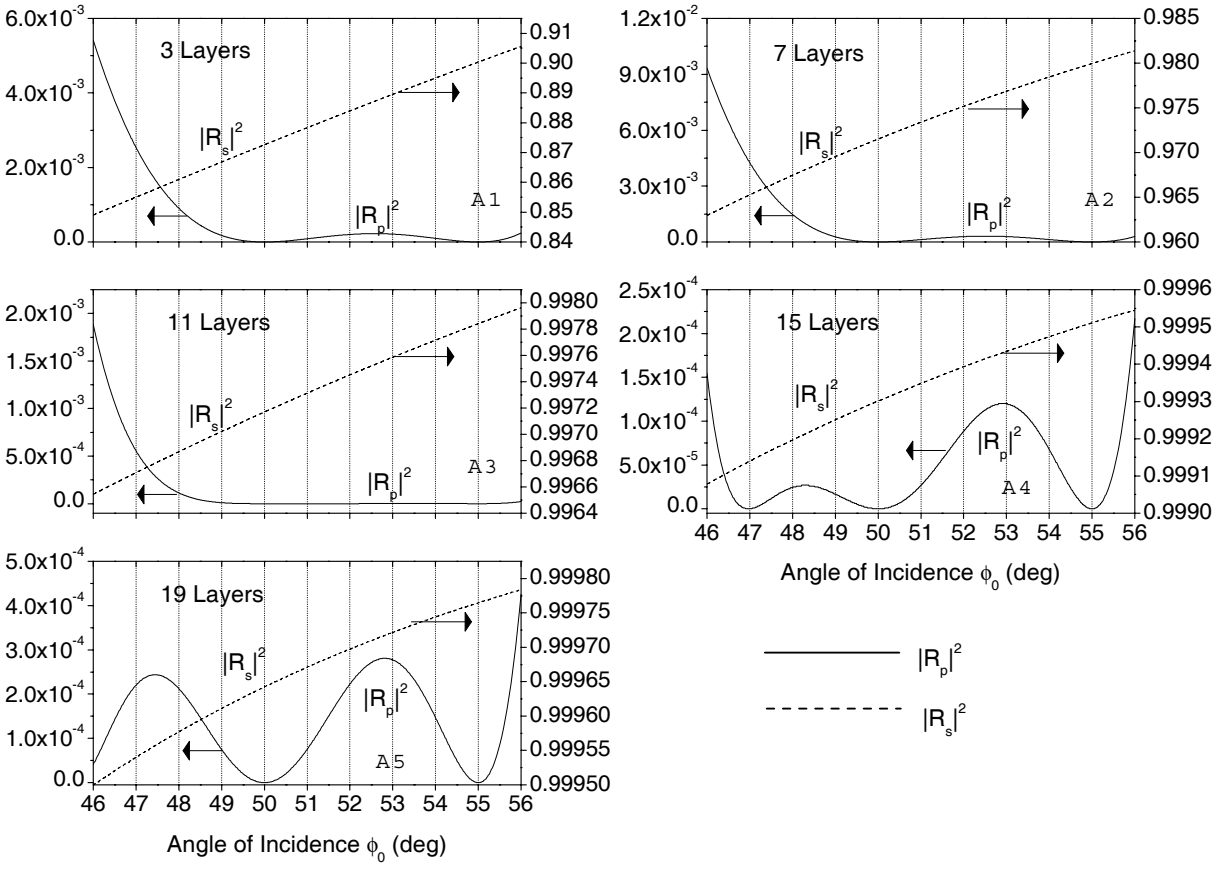

Figure 9 Reflectances $|R_p|^2$ and $|R_s|^2$ for various centro-symmetric multilayer stacks with 3-19 layers embedded in a ZnS substrate are plotted versus the angle of incidence ϕ_0 from 46° to 56°.The material system is the same as given in the caption of Fig. 5 and the metric film thicknesses associated with different multilayer stack designs are listed in Table 2.

4.1.2 Spectral sensitivity

The spectral sensitivities of the multilayer designs obtained in Section 4.1.1 are now analyzed. For the spectral sensitivity, the metric film thicknesses (d_1, d_2) and the angle of incidence $\phi_0 = 50^o$ for each multilayer design are kept constant and the wavelength λ is scanned from 8 to 12 μm. The dispersion of all the materials in this spectral region is accounted for.[37] Panels A1, A2, A3, A4 and A5 of Fig. 10 show the ER in reflection and transmission as a function of the wavelength λ for the 3, 7, 11, 15 and 19-layer designs, respectively. The left and right Y-axes of each panel of Fig. 10 represent ER_r and ER_t, respectively.

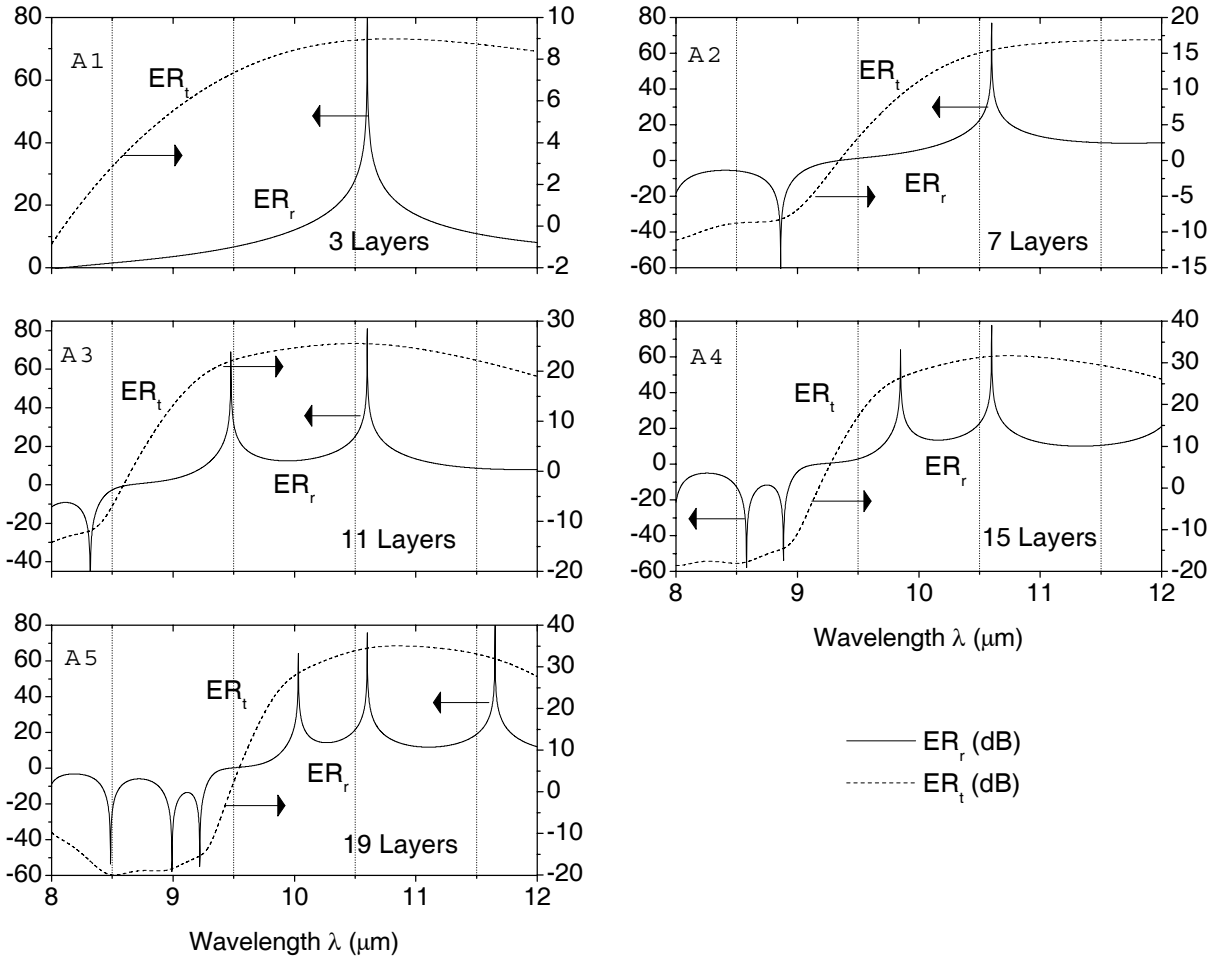

Figure 10 Extinction ratios in reflection and transmission (ER_r and ER_t) in dB for various centro-symmetric multilayer stacks with 3-19 layers embedded in a ZnS substrate are plotted versus wavelength $8 \leq \lambda \leq 12$ μm. The material system is the same as given in the caption of Fig. 5 and the metric film thicknesses associated with different multilayer stack designs are listed in Table 2.

All parameters for each panel in Fig. 10 are the same as those in Fig. 9. All the designs with 3-19 layers have a peak in ER_r at λ = 10.6 μm, which is the design wavelength. These devices also function as R_p = 0 polarizers, at additional discrete wavelengths other than the design wavelength. An interesting feature of these plots in Fig. 10 is that designs with a higher number of layers (>3) function as *orthogonal* polarizers (R_s = 0) or PBS at other discrete wavelengths in the spectral range $8 \leq \lambda \leq 12$ μm. Table 4 lists all the discrete wavelengths at which ER_r in Fig. 10 reaches a positive or negative peak.

Table 4 Discrete wavelengths at which the extinction ratio in reflection (ER_r) of Fig. 10 reaches a positive or negative peak.

# of Layers	λ (μm)	ER_r (dB)	ER_t (dB)
3	10.6	82.43	8.95
7	8.862	-66.08	-8.21
	10.6	77.05	15.44
11	8.318	-60.53	-11.87
	9.477	69.06	22.05
	10.6	81.08	25.48
15	8.582	-57.91	-17.72
	8.886	-53.9	-14.48
	9.85	63.92	26.44
	10.6	77.62	31.55
19	8.486	-53.73	-19.94
	8.991	-57.91	-18.51
	9.22	-55.02	-15.44
	10.032	64.28	28.48
	10.6	75.73	34.46
	11.652	80.66	31.92

Panels A1, A2, A3, A4 and A5 of Fig. 11 show the intensity reflectances $|R_p|^2$ and $|R_s|^2$ as a function of wavelength λ from 8 to 12 μm for 3-, 7-, 11-, 15- and 19-layer designs, respectively. All parameters for each panel in Fig. 11 are the same as those in Fig. 10. The $|R_p|^2$ curves of all the designs with 3-19 layers dip to zero at λ = 10.6 μm, which is the design wavelength. The 11-, 15- and 19-layer designs function as effective *s*-reflection polarizers with *s* reflectance $|R_s|^2 > 99\%$ over a 2 to 3 μm spectral bandwidth. The associated *p* reflectance is not low enough in these spectral regions to qualify these devices for polarizing beam splitters. The 19-layer design functions as an effective *s*-reflection polarizer with $|R_s|^2 > 99\%$ over $9.5 < \lambda < 12$ μm and also as a *p*-reflection polarizer with $|R_p|^2 > 99\%$ over $8.2 < \lambda < 9$ μm. With an increase in the number of layers in each design the number of wavelengths at which these devices act as polarizers or polarizing beam splitters increase.

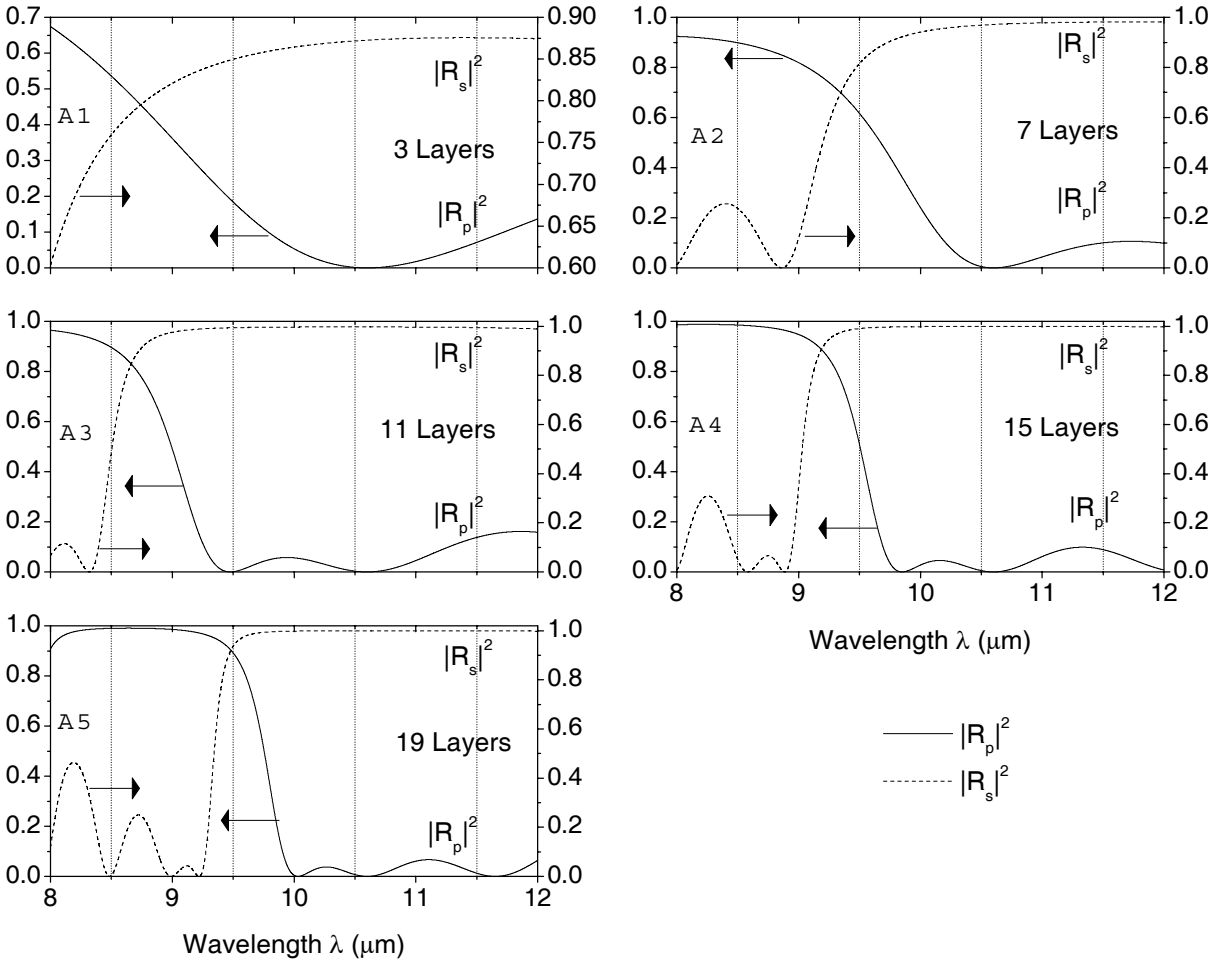

Figure 11 Reflectances $|R_p|^2$ and $|R_s|^2$ for various centro-symmetric multilayer stacks with 3-19 layers embedded in a ZnS substrate are plotted versus wavelength $8 \leq \lambda \leq 12$ μm. The material system is the same as given in the caption of Fig. 5 and the metric film thicknesses associated with different multilayer stack designs are listed in Table 2.

4.2 Centro-symmetric multilayer stacks as complete transmission QWR and HWR devices

4.2.1 IR QWR device using an embedded SiO_2-Si multilayer stack in GaP prism

The design procedure is outlined in Section 3.1.2. The results obtained for centro-symmetric multilayer stacks achieving QWR and HWR with complete transmission are presented here. The angular, spectral and thickness sensitivities are also considered.

A specific QWR cube design $(\phi_0 = 45^o)$ at the lightwave-communications wavelength of $\lambda = 1.55\ \mu m$ uses a centro-symmetric 11-layer stack of Si (n_0 = 3.4777) and SiO_2 (n_1 = 1.4444) thin films embedded in a high-index GaP (n_2 = 3.0535) prism. The angle of incidence $\phi_0 = 45^o$ is above the critical angle of the 0-1 interface $\phi_{crit} = 28.23^o$, so that FTIR takes place. With the design parameters listed in Table 5 we calculate $|T_p|^2 = |T_s|^2 = 0.999999$ and $\Delta_t = 90.0005^o$.

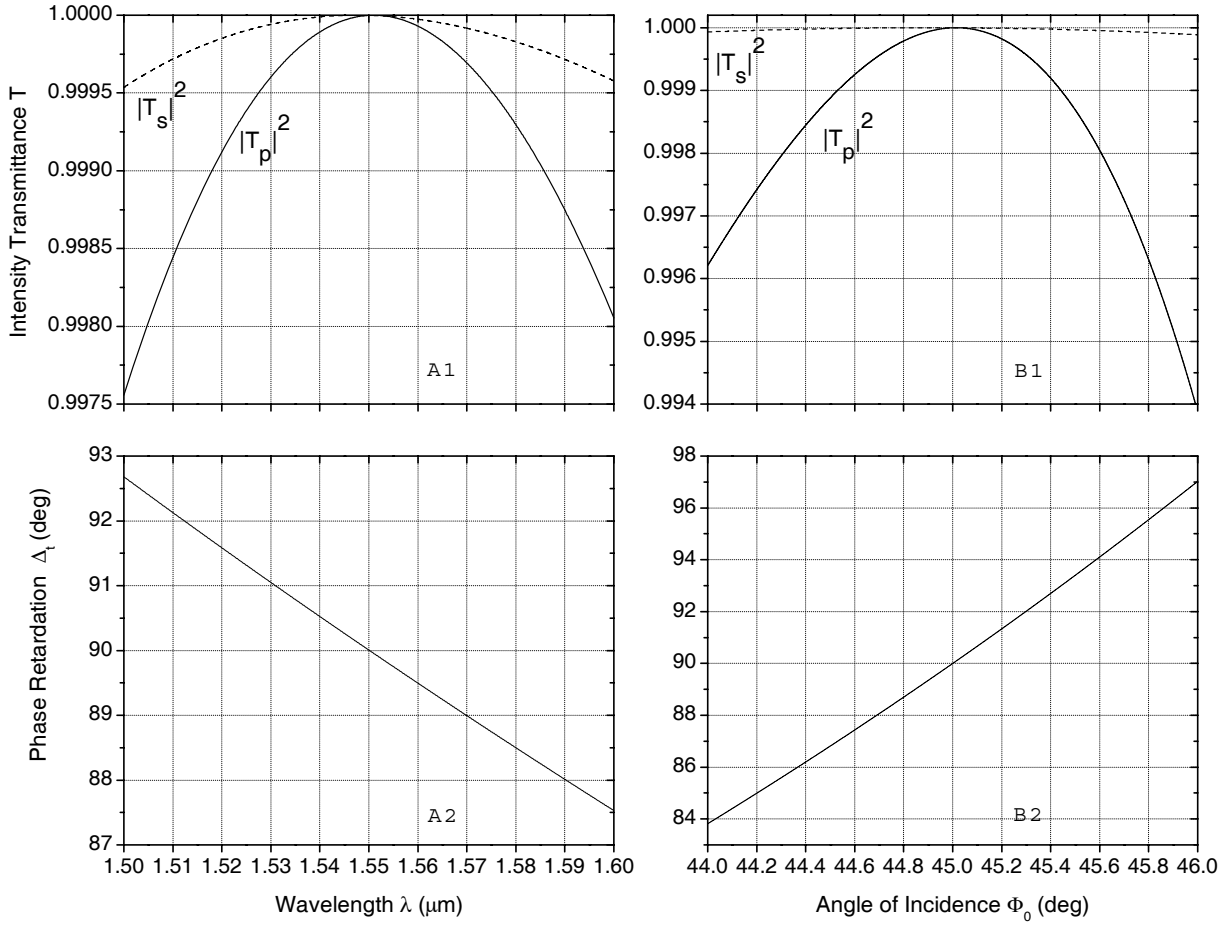

Figure 12 Panels (A1, A2) and (B1, B2) show the spectral and angular sensitivities, respectively, of a QWR cube design that operates at λ=1.55 μm and $\phi_0 = 45^o$. The design uses an 11-layer stack of Si (n_0 = 3.4777) and SiO_2 (n_1 = 1.4444) thin films embedded in a high-index GaP (n_2 = 3.0535) prism. The thicknesses of the SiO_2 and Si thin films are 17.5 *nm* and 67.1 *nm*, respectively. Both the *p* and *s* transmittances $|T_p|^2$ and $|T_s|^2$ and the differential transmission phase shift Δ_t are represented in this figure.

Table 5 Normalized (Z_1, Z_2) and metric (d_1, d_2) thicknesses corresponding to the complete transmission QWR and HWR devices presented in Section 4.2

Device	Z_1	Z_2	d_1 (nm)	d_2 (nm)
QWR	0.065103	0.601902	17.5	67.1
HWR	0.164135	2.001336	44.0	223.0

It is of interest to consider the spectral and angular sensitivities of the above QWR design. For the spectral sensitivity, the film thicknesses d_1 = 17.5 nm, d_2 = 67.1 nm and the angle of incidence $\phi_0 = 45^o$ are kept constant, and the wavelength λ is scanned over a 100-nm range from 1.5 to 1.6 μm.The dispersion of all materials in this spectral region is accounted for.[37,38] For the angle sensitivity, the film thicknesses d_1 = 17.5 nm, d_2 = 67.1 nm and the wavelength $\lambda = 1.55 \mu m$ are kept constant, and the internal angle of incidence ϕ_0 is varied by $\pm$ 1^o.

Panel A1 of Fig. 12 shows that $|T_p|^2$ and $|T_s|^2$ remain > 99.75 % over the 100-nm spectral region with a locally flat maximum (100 % transmission) at the design wavelength λ = 1.55 μm, hence the amplitude diattenuation in transmission is < 0.2 %. Panel A2 of Fig. 12 shows that the differential phase shift Δ_t deviates from 90^o by < $\pm$ 3^o over the 100-nm spectral range. Panels B1 and B2 of Fig. 12 show $|T_p|^2$, $|T_s|^2$ and Δ_t as functions of the angle of incidence ϕ_0. $|T_p|^2$ and $|T_s|^2$ remain high (> 99.4%) while Δ_t deviates from 90^o by <$\pm$ 7^o for $\pm$ 1^o change in the internal angle of incidence around $\phi_0 = 45^o$. The field of view in air is larger than that in prism by a factor of 3.

We now consider the sensitivity of this QWR to film-thickness errors by keeping the wavelength $\lambda = 1.55 \mu m$ and angle of incidence $\phi_0 = 45^o$ constant, and varying the thickness d_i of the i^{th} film (i = 1, 2, …., 11) by $\pm$ 5 % around its design value. (The films are numbered starting from the medium of incidence.) The resulting small shifts in the transmittances $|T_p|^2$ and $|T_s|^2$ (which are parabolic) and in the differential phase shift Δ_t (which are linear) are represented in

Fig. 13. The left Panels A1, A2, and A3 of Fig. 13 show the effect of thickness errors of the odd-numbered low-index (SiO_2) films, whereas the right Panels B1, B2, and B3 show the effect of errors in thickness of the even-numbered high-index (Si) films. Because of the symmetry of the design stack, thickness errors for films that are symmetrically located above and below the center layer (e.g., 1 and 11, 2 and 10, and 3 and 9) produce identical shifts in the retarder's response. The effect of simultaneous errors in the thicknesses of all films can be determined, to first order in retardance or second order in transmittances, by superposition of the results shown in Fig. 13.

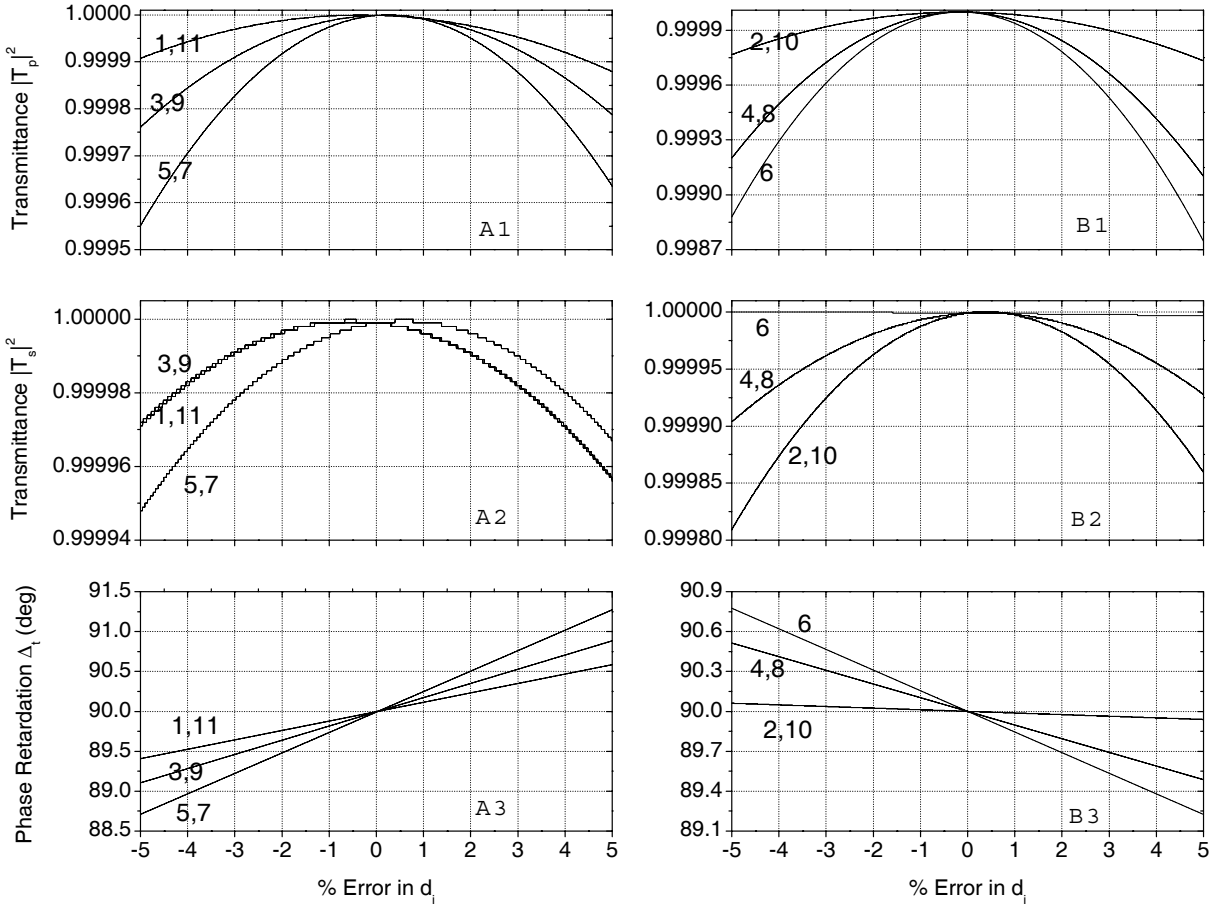

Figure 13 Panels (A1, A2, A3) and (B1, B2, B3) show the sensitivities of the QWR cube design that operates at λ = 1.55 μm and $\phi_0 = 45^o$ to errors of thickness of the odd- and even-numbered films, respectively. Both the *p* and *s* transmittances $|T_p|^2$ and $|T_s|^2$ and the differential transmission phase shift Δ_t are represented in this figure. The design uses an 11-layer stack of Si (n_0 = 3.4777) and SiO_2 (n_1 = 1.4444) thin films embedded in a high-index GaP (n_2 = 3.0535) prism. The thicknesses of the SiO_2 and Si thin films are changed by ± 5 % around the design values of 17.5 nm and 67.1 nm, respectively.

4.2.2 IR HWR device using an embedded SiO_2-Si multilayer stack in Si prism

An HWR cube design at $\lambda = 1.55\ \mu m$ uses a centro-symmetric 7-layer stack of Si (n_2 = 3.4777) and SiO_2 (n_1 = 1.4444) thin films embedded in a high-index Si (n_0 = 3.4777) prism. The angle of incidence ($\phi_0 = 45^o$) is above the critical angle of the 0-1 interface ($\phi_{crit} = 24.54^{\circ}$), hence FTIR takes place. With the design parameters listed in Table 5 we calculate $|T_p|^2 = |T_s|^2 = 0.999999$ and $\Delta_t = 179.98^{\circ}$.

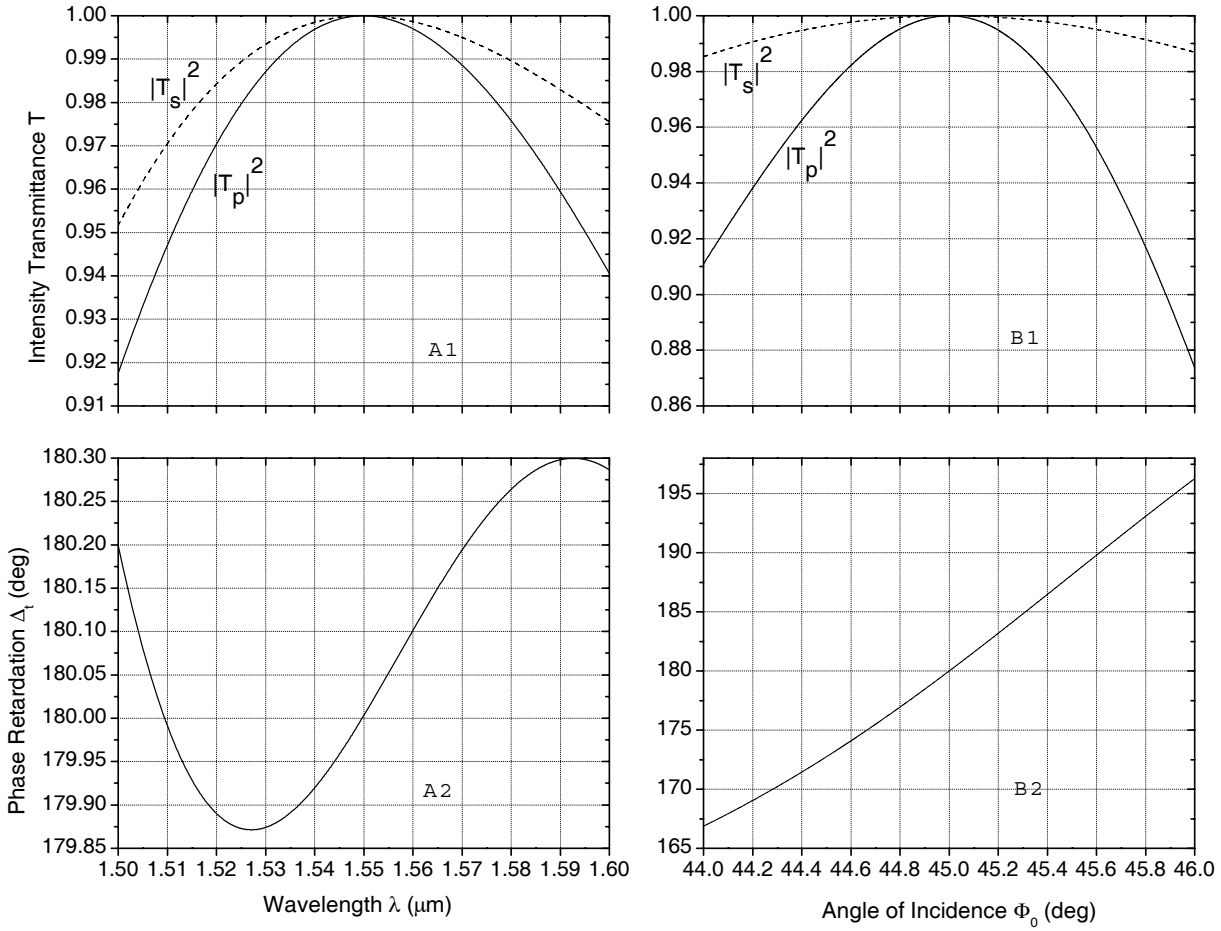

Figure 14 Panels (A1, A2) and (B1, B2) show the spectral and angular sensitivities, respectively, for an HWR cube design that operates at λ = 1.55 μm and $\phi_0 = 45^{\circ}$ that uses a centro-symmetric 7-layer stack of Si (n_2 = 3.4777) and SiO_2 (n_1 = 1.4444) thin films embedded in a Si prism (n_0 = 3.4777). The design thicknesses of the SiO_2 and Si thin films are d_1 =44.0 nm and d_2 = 223.0 nm, respectively. Both the *p* and *s* transmittances $|T_p|^2$ and $|T_s|^2$ and the differential transmission phase shift Δ_t are represented in this figure.

Figure 14 shows the spectral and angular sensitivities of the HWR design. The dispersion of Si and SiO_2 in the 100-nm spectral region is accounted for.[37,38] Panel A1 of Fig. 14 shows that $|T_p|^2$ and $|T_s|^2$ remain > 91 % over the 100-nm spectral region with a locally flat maximum (= 100 %) at the design wavelength $\lambda = 1.55\,\mu m$. The amplitude diattenuation is < 3 %. Panel A2 of Fig. 14 shows that Δ_t deviates from 180^o by $\leq \pm 0.3^o$ over the 100-nm spectral range. Panels B1 and B2 of Fig. 14 show $|T_p|^2$, $|T_s|^2$ and Δ_t as functions of ϕ_0. $|T_s|^2$ remains high (> 98 %), whereas $|T_p|^2$ dips to 87.5 %, as the angle of incidence is changed by $\pm 1^o$. The differential transmission phase shift Δ_t deviates from 180^o by $< \pm 17^o$ (< 10 %) for $\pm 1^o$ change in the internal angle of incidence around $\phi_0 = 45^o$. The field of view of the HWR in air is wider (by a factor n_0 > 3), if one accounts for light refraction from air to Si at the entrance face of the prism.

The sensitivity of this HWR design to film-thickness errors is considered by holding the wavelength $\lambda = 1.55\,\mu m$ and angle of incidence $\phi_0 = 45^o$ constant, and by varying each film thickness d_i (i = 1, 2, …., 7) by ± 5 % around its design values. The resulting shifts in the transmittances $|T_p|^2$ and $|T_s|^2$ (which are parabolic) are represented by Panels A1 and B1 of Fig. 15, and the corresponding shifts in the differential phase shift Δ_t (which are linear) are shown in Panels A2 and B2 of Fig. 15. Given the symmetry of the design stack, errors of thickness of films that are symmetrically located on opposite sides of the center layer produce identical effects. The result of introducing simultaneous errors in the thicknesses of all films can be determined, to first order in reflectances and second order in transmittances, by superposition using the results shown in Fig. 15.

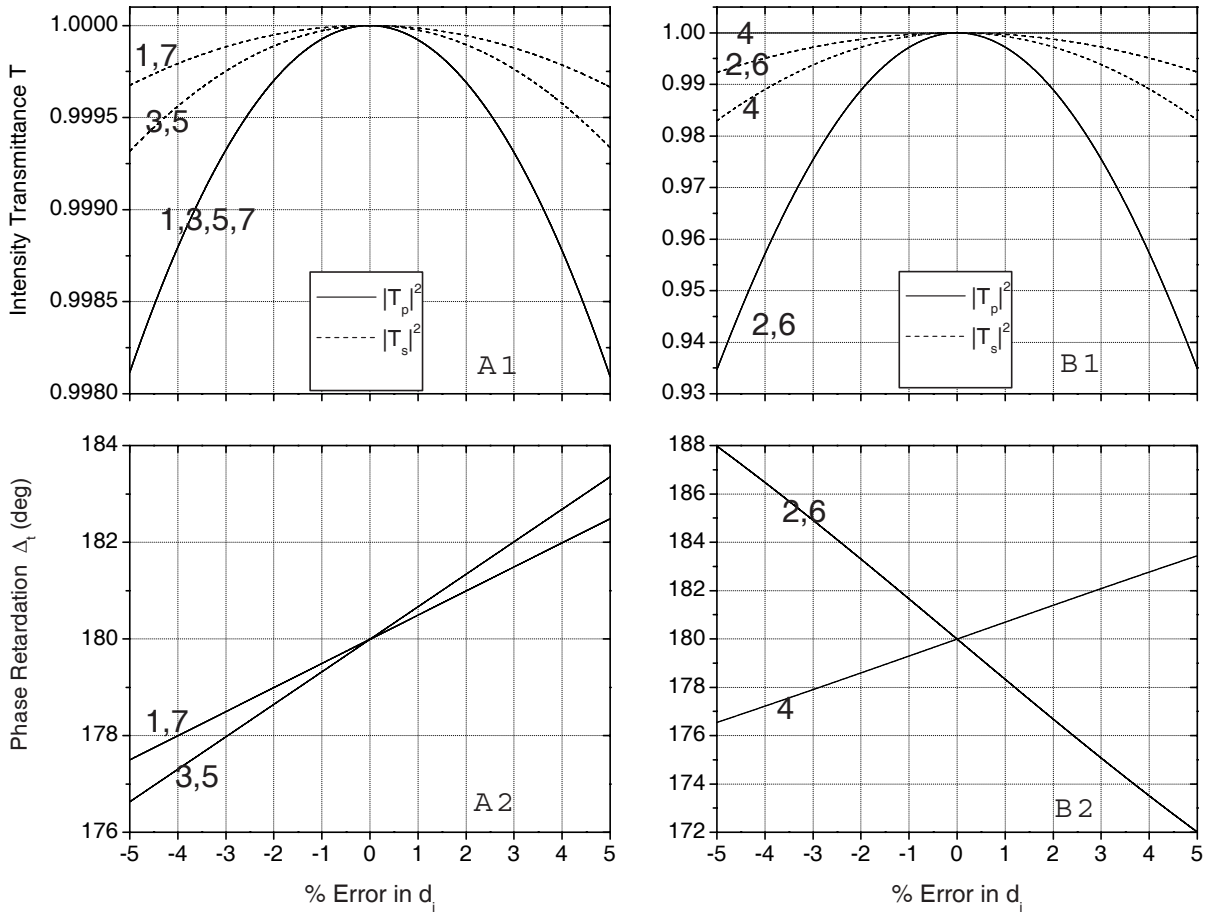

Figure 15 Transmittances $|T_p|^2$ and $|T_s|^2$ for *p*- and *s*-polarized light and differential transmission phase shift Δ_t of an HWR cube design, that operates at $\lambda = 1.55$ μm and $\phi_0 = 45^o$, are plotted versus the error of thickness of each film. The design uses a 7-layer stack of Si ($n_0 = 3.4777$) and SiO_2 ($n_1 = 1.4444$) thin films embedded in a high-index Si ($n_2 = 3.4777$) prism. The thicknesses of the SiO_2 and Si thin films are changed by $\pm$ 5 % around the design values of 44.0 nm and 223.0 nm, respectively.

4.3 Centro-symmetric multilayer stacks as 50%-50% beam splitters

The design procedure is outlined in Section 3.1.3. The results obtained for various centro-symmetric multilayer 50%-50% beam splitters listed in Table 1 are presented here. The angular and spectral sensitivities of some of the devices are also considered. Table 6 lists various monochromatic cube designs in the visible, near-infrared and at the CO_2 laser wavelength.

Table 6 50%-50% beam splitter cube designs in the visible, near-infrared and CO_2 laser wavelength

# of Layers	n_0	n_1	n_2	$\|R_p\|^2$	$\|R_s\|^2$	Δ_r	Δ_t	Z_1	Z_2
$\|R_p\|^2 = \|R_s\|^2 = \|T_p\|^2 = \|T_s\|^2 \approx 0.5; \Delta_r = 0^o$ and $\Delta_t = 0^o$; $\lambda = 10.6$ μ m; $\phi_0 = 45^o$									
15	3.2919	1.5251	5.6315	0.49908	0.49908	0	-0.01176	0.223961	1.120375
15	2.6817	1.2975	3.2919	0.499341	0.499341	0	-0.00844	0.354839	1.251386
19	2.1919	1.3765	4.0038	0.498492	0.498492	0	-0.00857	0.704937	0.809739
$\|R_p\|^2 = \|R_s\|^2 = \|T_p\|^2 = \|T_s\|^2 \approx 0.5; \Delta_r = 0^o$ and $\Delta_t = 180^o$; $\lambda = 10.6$ μ m; $\phi_0 = 45^o$									
3	4.0038	1.2975	4.0038	0.501783	0.501783	0	-180.027	0.161472	2.307135
15	3.4177	1.2289	3.4177	0.498157	0.498157	0	-180.013	0.060328	2.605541
15	2.1919	1.2853	2.6705	0.499078	0.499078	0	-180.011	0.628729	1.135609
19	4.0038	1.2975	5.6315	0.499729	0.499729	0	-180.107	0.096582	1.517991
19	2.4026	1.5251	4.0038	0.500165	0.500165	0	-179.992	0.766485	0.774465
$\|R_p\|^2 = \|R_s\|^2 = \|T_p\|^2 = \|T_s\|^2 \approx 0.5; \Delta_r = 180^o$ and $\Delta_t = 0^o$; $\lambda = 10.6$ μ m; $\phi_0 = 45^o$									
15	2.4026	1.2289	5.6315	0.49908	0.49908	180	0.014662	0.113143	0.765634
$\|R_p\|^2 = \|R_s\|^2 = \|T_p\|^2 = \|T_s\|^2 \approx 0.5; \Delta_r = 180^o$ and $\Delta_t = 180^o$; $\lambda = 10.6$ μ m; $\phi_0 = 45^o$									
19	2.1919	1.3765	5.6315	0.499115	0.499115	-180	-180.056	0.441946	0.549033
15	2.1919	1.2975	5.6315	0.499757	0.499757	180	179.8184	0.364796	0.887992
19	2.1919	1.3765	5.6315	0.499115	0.499115	-180	-180.056	0.441946	0.549033
$\|R_p\|^2 = \|R_s\|^2 = \|T_p\|^2 = \|T_s\|^2 \approx 0.5; \Delta_r = 0^o$ and $\Delta_t = 0^o$; $\lambda = 1.55$ μ m; $\phi_0 = 45^o$									
15	2.2710	1.3827	2.7332	0.501649	0.501649	0	-0.00051	0.883346	1.143537
15	2.2710	1.3193	2.4555	0.501745	0.501745	0	-0.02347	0.84304	1.128708
$\|R_p\|^2 = \|R_s\|^2 = \|T_p\|^2 = \|T_s\|^2 \approx 0.5; \Delta_r = 0^o$ and $\Delta_t = 180^o$; $\lambda = 1.55$ μ m; $\phi_0 = 45^o$									
15	2.7332	1.3568	3.0535	0.501154	0.501154	0	180.0194	0.447349	1.406845
15	2.4555	1.3827	3.0535	0.501635	0.501635	0	-179.996	0.518109	1.177792
$\|R_p\|^2 = \|R_s\|^2 = \|T_p\|^2 = \|T_s\|^2 \approx 0.5; \Delta_r = 0^o$ and $\Delta_t = 0^o$; $\lambda = 0.633$ μ m; $\phi_0 = 45^o$									
15	2.5283	1.4732	2.7276	0.499148	0.499148	0	-0.0207	0.857317	1.125254
19	2.7276	1.4732	2.9886	0.498596	0.498596	0	0.015666	0.535905	1.488865
$\|R_p\|^2 = \|R_s\|^2 = \|T_p\|^2 = \|T_s\|^2 \approx 0.5; \Delta_r = 0^o$ and $\Delta_t = 180^o$; $\lambda = 0.633$ μ m; $\phi_0 = 45^o$									
11	2.5906	1.4880	2.7276	0.501496	0.501496	0	-179.999	0.84387	1.392062
11	2.5283	1.5565	2.7276	0.499852	0.499852	0	179.9951	1.129887	1.170361
11	2.3504	1.4328	2.5283	0.499415	0.499415	0	179.9748	1.078233	1.204307
15	2.6398	1.4732	2.7276	0.500591	0.500591	0	179.8986	0.86237	1.379663
15	2.1055	1.3245	2.3504	0.501734	0.501734	0	-180.022	1.024262	0.794393
19	2.5906	1.3245	2.9886	0.500675	0.500675	0	-180.057	0.473696	1.565004
19	2.5728	1.3245	2.9886	0.500471	0.500471	0	-180.163	0.480052	1.546358

Table 6 continued…

$\lvert R_p\rvert^2 = \lvert R_s\rvert^2 = \lvert T_p\rvert^2 = \lvert T_s\rvert^2 \approx 0.5; \Delta_r$ =-90° and Δ_t =90°; λ = 10.6 μ m; ϕ_0 =45°									
7	3.2919	1.2289	4.0038	0.499805	0.499805	-90	89.91616	0.192835	1.65936
7	2.4026	1.2853	2.6817	0.501552	0.501552	-90	90.06921	0.634811	1.372146
7	2.1919	1.2975	2.402	0.500867	0.500867	-90	90.09664	0.979812	1.184854
11	2.1919	1.2975	5.6315	0.500025	0.500025	-90	90.0197	0.297014	0.933023
11	2.6705	1.6247	4.0038	0.50001	0.50001	-90	90.01103	0.599676	0.705015
15	2.6817	1.5845	3.4177	0.500747	0.500747	-90	90.15455	0.726915	1.177706
15	2.6817	1.2853	3.4177	0.500643	0.500643	-90	90.18617	0.334382	1.213735
15	2.4026	1.4540	3.4177	0.501643	0.501643	-90	90.29479	0.704173	1.052177
19	4.0038	1.5251	5.6315	0.498192	0.498192	-90	89.97159	0.137287	1.441707
19	3.4177	1.5251	5.6315	0.499186	0.499186	-90	89.97817	0.17862	1.115979
$\lvert R_p\rvert^2 = \lvert R_s\rvert^2 = \lvert T_p\rvert^2 = \lvert T_s\rvert^2 \approx 0.5; \Delta_r$ =-90° and Δ_t =90°; λ = 1.55 μ m; ϕ_0 =45°									
7	3.0535	1.4660	3.4777	0.500666	0.500666	-90	90.06338	0.430118	1.50383
7	2.7332	1.4660	3.0535	0.501409	0.501409	-90	89.92518	0.640199	1.366176
7	2.4555	1.4260	3.4777	0.499162	0.499162	-90	90.02917	0.518429	1.004559
7	2.2710	1.3827	3.4777	0.500523	0.500523	-90	89.94589	0.588979	0.697851
15	2.4555	1.3827	3.0535	0.501418	0.501418	-90	89.83067	0.622599	1.296565
15	2.2710	1.3827	3.0535	0.500372	0.500372	-90	90.13153	0.773497	1.07054
$\lvert R_p\rvert^2 = \lvert R_s\rvert^2 = \lvert T_p\rvert^2 = \lvert T_s\rvert^2 \approx 0.5; \Delta_r$ =-90° and Δ_t =90°; λ = 0.633 μ m; ϕ_0 =45°									
15	2.6398	1.4880	2.9886	0.500048	0.500048	-90	90.1086	0.736006	1.255242
15	2.5906	1.4576	2.9886	0.499266	0.499266	-90	90.176	0.684477	1.096744
15	2.5728	1.4328	2.9886	0.499512	0.499512	-90	90.10218	0.649959	1.106903
15	2.5283	1.3615	2.9886	0.49854	0.49854	-90	90.14496	0.555528	1.141683
$\lvert R_p\rvert^2 = \lvert R_s\rvert^2 = \lvert T_p\rvert^2 = \lvert T_s\rvert^2 \approx 0.5; \Delta_r$ =-90° and Δ_t =-90°; λ =10.6 μ m; ϕ_0 =45°									
7	2.6705	1.6247	4.0038	0.498731	0.498731	-90	-89.9782	0.562143	0.747104
11	3.4177	1.3765	4.0038	0.498686	0.498686	-90	-89.9887	0.247714	1.737035
19	3.2919	1.6247	5.6315	0.499703	0.499703	-90	-90.0106	0.267305	0.998882
19	2.4026	1.4540	5.6315	0.498884	0.498884	-90	-89.9687	0.307323	0.810862
19	2.6817	1.2289	4.0038	0.498217	0.498217	-90	-89.7005	0.236034	1.113749
19	2.6705	1.2289	4.0038	0.500829	0.500829	-90	-89.7088	0.238398	1.108369
$\lvert R_p\rvert^2 = \lvert R_s\rvert^2 = \lvert T_p\rvert^2 = \lvert T_s\rvert^2 \approx 0.5; \Delta_r$ =-90° and Δ_t =-90°; λ =1.55 μ m; ϕ_0 =45°									
7	2.2710	1.3568	3.4777	0.501304	0.501304	-90	-90.0069	0.503804	0.774306
15	2.4555	1.4443	2.5812	0.501941	0.501941	-90	-89.7613	1.070813	1.217802
19	2.5812	1.3827	3.4777	0.499941	0.499941	-90	-90.0069	0.461541	1.351135
19	2.4555	1.3193	3.4777	0.499728	0.499728	-90	-89.9778	0.440251	1.312026
19	2.2710	1.3568	2.5812	0.501898	0.501898	-90	-89.8111	0.899423	0.961746
$\lvert R_p\rvert^2 = \lvert R_s\rvert^2 = \lvert T_p\rvert^2 = \lvert T_s\rvert^2 \approx 0.5; \Delta_r$ =-90° and Δ_t =-90°; λ =0.633 μ m; ϕ_0 =45°									
11	2.5906	1.5565	2.9886	0.500532	0.500532	-90	-89.8612	0.934084	1.17168
11	2.3504	1.4732	2.7276	0.500979	0.500979	-90	-90.1449	1.145647	1.041564

4.3.1 50%-50% IR polarization-independent beam splitters (PIBS) using an embedded KBr-Ge multilayer stack in Si prism

A beam splitter that reflects and refracts light simultaneously without change of polarization is defined as a polarization independent beam splitter (PIBS). A specific PIBS design operating at the CO_2 laser wavelength $\lambda = 10.6\ \mu$m and at an angle of incidence $\phi_0 = 60^o$ uses a centro-symmetric 15-layer stack of Ge (n_0 = 4.0038) and KBr (n_1 = 1.5251) thin films embedded in a high-index Si (n_2 = 3.4177) prism. The angle of incidence $\phi_0 = 60^o$ is above the critical angle of the 0-1 interface $\phi_{crit} = 26.50^o$, so that FTIR takes place. The solution sets for the normalized thicknesses are listed in Table 7.

Table 7 Normalized (Z_1, Z_2) thicknesses corresponding to the 50%-50% beam splitters presented in Sections 4.3.1, 4.3.2, 4.3.3 and 4.3.4

# of Layers	ϕ_0	n_0	n_1	n_2	$\|R_p\|2$	$\|R_s\|2$	Δ_r	Δ_t	Z_1	Z_2
15	60°	3.4177	1.5251	4.0038	0.498647	0.498647	0	-0.01	0.119278	2.277189
15	45°	3.4177	1.2289	3.4177	0.498157	0.498157	0	179.99	0.060328	2.605541
15	45°	2.4026	1.2289	5.6315	0.49908	0.49908	180	0.01	0.113143	0.765634
7	60°	2.1919	1.5251	5.6315	0.500553	0.500553	180	180.00	0.185617	0.591113

The spectral and angular sensitivities of the above PIBS design are considered now. For the spectral sensitivity, the film thicknesses d_1 = 207.2 *nm*, d_2 = 1507.2 *nm* and the angle of incidence $\phi_0 = 60^o$ are kept constant, and the wavelength λ is scanned over a 100-*nm* range from 10 to 11 μm. The dispersion of all materials in this spectral region is accounted for[37]. For the angle sensitivity, the film thicknesses d_1 = 207.25 *nm*, d_2 = 1507.2 *nm* and the wavelength $\lambda = 10.6 \mu m$ are kept constant, and the internal angle of incidence ϕ_0 is varied by $\pm 1^o$.

Panel A1 of Fig. 16 shows that $|R_p|^2$ and $|R_s|^2$ vary from 0.0 to 0.65 over the 100-*nm* spectral region with 50% reflectance at the design wavelength λ = 10.6 μm. Panel A2 of Fig. 16

shows that the differential phase shifts Δ_r, Δ_t deviate from 0^o by < 14^o over the 100-nm spectral range. Panels B1 and B2 of Fig. 16 show $|R_p|^2$, $|R_s|^2$ Δ_r and Δ_t as functions of the angle of incidence ϕ_0. $|R_p|^2$ and $|R_s|^2$ vary from 0.2 to 0.6 while Δ_r, Δ_t deviate from 0^o by $< \pm 17.5^o$ for $\pm 1^o$ change in the internal angle of incidence around $\phi_0 = 60^o$.

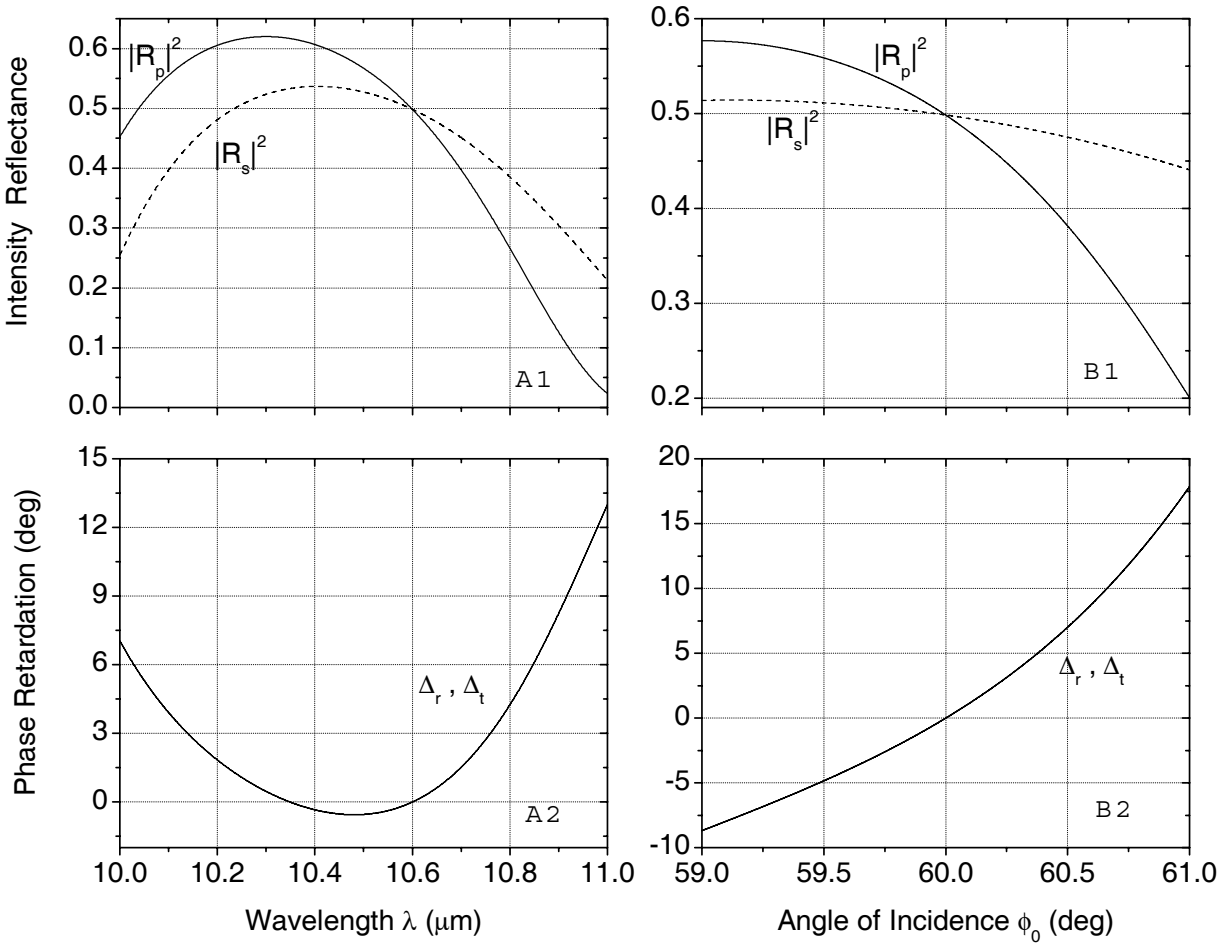

Figure 16 Panels (A1, A2) and (B1, B2) show the spectral and angular sensitivities, respectively, of 50%-50% PIBS that operates at λ =10.6 μm and $\phi_0 = 60^o$. The design uses a 15-layer stack of Ge (n_0 = 4.0038) and KBr (n_1 = 1.5251) thin films embedded in a high-index Si (n_2 = 3.4177) prism. The thicknesses of the KBr and Ge thin films are 207.2 *nm* and 1507.2 *nm*, respectively. Both the *p* and *s* reflectances $|R_p|^2$ and $|R_s|^2$ and the differential reflection and transmission phase shifts Δ_r and Δ_t are represented in this figure.

4.3.2 50%-50% IR beam splitters with no change of polarization in reflection and HWR in transmission using an embedded NaF-Si Multilayer stack in a Si prism

A 50%-50% beam splitter cube with no change of polarization ($\Delta_r = 0^o$) in reflection and HWR ($\Delta_t = 180^o$) in transmission, operating at the CO_2 laser wavelength $\lambda = 10.6\ \mu$m uses a centro-symmetric 15-layer stack of Si ($n_0 = 3.4177$) and NaF ($n_1 = 1.2289$) thin films embedded in a high-index Si ($n_2 = 3.4177$) prism. (The refractive indices of Si and NaF are calculated to 4 decimal places using published dispersion relations[37]) The angle of incidence $\phi_0 = 45^o$ is above the critical angle of the 0-1 interface $\phi_{crit} = 21.07^o$, so that FTIR takes place. The solution sets for the normalized thicknesses are listed in Table 7.

Figure 17 shows the spectral and angular sensitivities of the above design. Panel A1 of Fig. 17 shows that $|R_p|^2$ and $|R_s|^2$ vary from 0.1 to 0.6 over the 50-*nm* spectral region with 50% reflectance at the design wavelength $\lambda = 10.6\,\mu m$. Panel A2 of Fig. 17 shows that the differential phase shift Δ_r deviate from 0^o by $< 2.5^o$ over 50-nm spectral range $10.5 \le \lambda \le 11\ \mu$m. Panel A3 of Fig. 17 shows that the differential phase shift Δ_t deviate from 180^o by $< 8^o$ over 50-nm spectral range $10.5 \le \lambda \le 11\ \mu$m. Panels B1, B2 and B3 of Fig. 17 show $|R_p|^2$, $|R_s|^2$, Δ_r and Δ_t as functions of the angle of incidence ϕ_0. $|R_p|^2$ and $|R_s|^2$ vary from 0.24 to 0.64 with 50% reflectance at $\phi_0 = 45^o$ while Δ_r and Δ_t deviate from 0^o and 180^o, respectively, by $< 18^o$ for $\pm 1^o$ change in the internal angle of incidence around $\phi_0 = 45^o$. The field of view of the above 50%-50% beam splitter in air is wider (by a factor $n_0 > 3$), if light refraction from air to Si at the entrance face of the prism is accounted for using Snell's law.

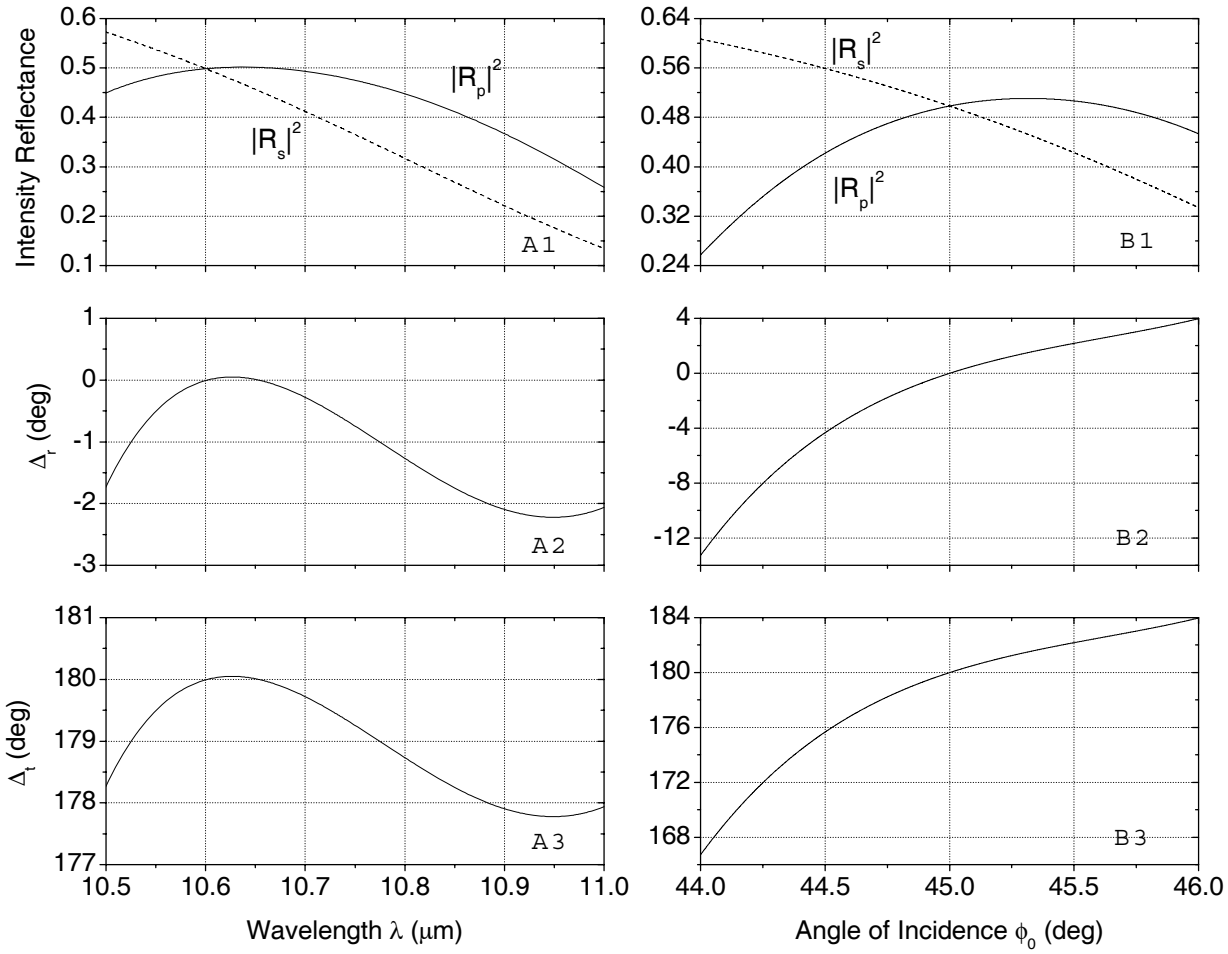

Figure 17 Panels (A1, A2, A3) and (B1, B2, B3) show the spectral and angular sensitivities, respectively, of 50%-50% BS that achieves $\Delta_r = 0^o$ and $\Delta_r = 180^o$at the operating wavelength λ =10.6 μm and $\phi_0 = 45^o$. The design uses a 15-layer stack of Si ($n_0 = 3.4177$) and NaF ($n_1 = 1.2289$) thin films embedded in a high-index Si ($n_2 = 3.4177$) prism. The thicknesses of the NaF and Si thin films are 130.091 *nm* and 2020.27 *nm*, respectively. Both the *p* and *s* reflectances $|R_p|^2$ and $|R_s|^2$ and the differential reflection and transmission phase shifts Δ_r and Δ_t are represented in this figure.

4.3.3 50%-50% IR beam splitters with HWR in reflection and no change of polarization in transmission using an embedded NaF-PbTe multilayer stack in a ZnSe prism.

This specific 50%-50% beam splitter cube with HWR in reflection ($\Delta_r = 180^o$) and no change of polarization ($\Delta_t = 0^o$) in transmission, operating at the CO_2 laser wavelength $\lambda = 10.6$ μm uses a centro-symmetric 15-layer stack of PbTe ($n_0 = 5.6315$) and NaF ($n_1 = 1.2289$) thin

films embedded in a high-index ZnSe (n_2 = 2.4026) prism. (The refractive indices of ZnSe, NaF and PbTe are calculated to 4 decimal places using published dispersion relations[37]) The angle of incidence $\phi_0 = 45^o$ is above the critical angle of the 0-1 interface $\phi_{crit} = 30.76^o$, so that FTIR takes place. The solution sets for the normalized thicknesses are listed in Table 7.

Figure 18 shows the spectral and angular sensitivities of the above design. Panel A1 of Fig. 18 shows that $|R_p|^2$ and $|R_s|^2$ vary from 0.24 to 0.65 over the 100-nm spectral region with 50% reflectance at the design wavelength $\lambda = 10.6\,\mu m$. Panels A2 and A3 of Fig. 18 show that the differential phase shifts Δ_r and Δ_t deviate from 180° and 0°, respectively, by < 18° over 100-*nm* spectral range $10 \le \lambda \le 11\,\mu$m. Panels B1, B2 and B3 of Fig. 18 show $|R_p|^2$, $|R_s|^2$, Δ_r and Δ_t as functions of the angle of incidence ϕ_0. $|R_p|^2$ varies from 0.35 to 0.60 while $|R_s|^2$ remains relatively flat at 0.5 with each of the curves having 50% reflectance at $\phi_0 = 45^o$. Δ_r and Δ_t deviate from 180° and 0°, respectively, by < $\pm 16^o$ for $\pm 1^o$ change in the internal angle of incidence around $\phi_0 = 45^o$. The differential reflection and transmission phase shifts show a linear profile with change in the internal angle of incidence around $\phi_0 = 45^o$. The field of view of the above 50%-50% beam splitter in air is wider (by a factor n_0 > 2), if light refraction from air to ZnSe at the entrance face of the prism is accounted for using Snell's law. 50%-50% beam splitters with half-wave retardation in reflection and no change of polarization in transmission can find valuable applications in Michelson interferometer. This beam splitter when used in a Michelson interferometer renders its operation totally independent of the source polarization.[39] In effect, the two recombining beams (at the detector) are of equal intensity and have the same polarization as that of the incident beam.

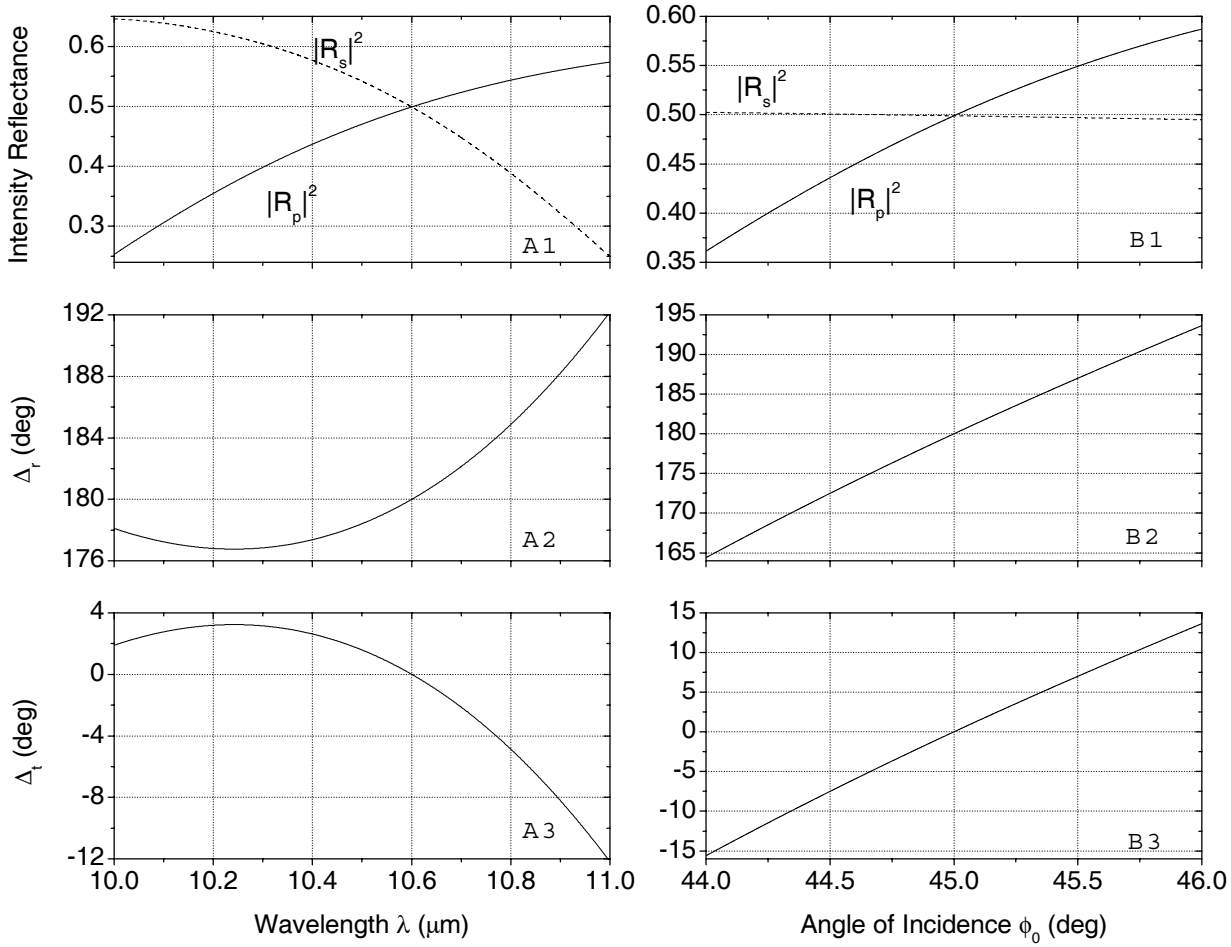

Figure 18 Panels (A1, A2, A3) and (B1, B2, B3) show the spectral and angular sensitivities, respectively, of 50%-50% BS that achieves $\Delta_r = 180^o$ and $\Delta_r = 0^o$at the operating wavelength λ =10.6 μm and $\phi_0 = 45^o$. The design uses a 15-layer stack of PbTe (n_0 = 5.6315) and NaF (n_1 = 1.2289) thin films embedded in a high-index ZnSe (n_2 = 2.4026) prism The thicknesses of the NaF and PbTe thin films are 243.98 nm and 360.28 *nm*, respectively. Both the *p* and *s* reflectances $|R_p|^2$ and $|R_s|^2$ and the differential reflection and transmission phase shifts Δ_r and Δ_t are represented in this figure.

4.3.4 50%-50% IR beam splitters with HWR in reflection and transmission using KBr-PbTe multilayer stack embedded in a ZnS prism

This specific 50%-50% beam splitter design with HWR ($\Delta_r = \Delta_t = 180^o$) in reflection and transmission operating at an angle of incidence $\phi_0 = 60^o$ and at the CO_2 laser wavelength $\lambda =$ 10.6 μm uses a centro-symmetric 7-layer stack of PbTe (n_0 = 5.6315) and KBr (n_1 = 1.5251)

thin films embedded in a high-index ZnS (n_2 = 2.1919) prism (The refractive indices of ZnS, PbF_2 and PbTe are calculated to 4 decimal places using published dispersion relations[37]). The angle of incidence ϕ_0 = 60° is above the critical angle of the 0-1 interface ϕ_{crit} = 44.08°, so that FTIR takes place. The solution sets for the normalized and metric thicknesses are listed in Table 7.

Figure19 shows the spectral and angular sensitivities of the above design. Panel A1 of Fig. 19 shows that $|R_p|^2$ and $|R_s|^2$ vary from 0.35 to 0.65 over the 100-nm spectral region with 50% reflectance at the design wavelength λ = 10.6 μm. Panel A2 and A3 of Fig. 19 show the differential phase shifts Δ_r and Δ_t that deviate from 180° by < ± 12° over 100-*nm* spectral range $10 \le \lambda \le 11$ μm. Panels B1, B2 and B3 of Fig. 19 show $|R_p|^2$, $|R_s|^2$, Δ_r and Δ_t as functions of the angle of incidence ϕ_0. $|R_p|^2$ varies from 0.46 to 0.54 while $|R_s|^2$ remains relatively flat at 0.5 with 50% reflectance at ϕ_0 = 60° for each of the curves. Δ_r and Δ_t deviate from 180° by < ± 6° for ± 1° change in the internal angle of incidence around $\phi_0 = 60°$. The field of view of the above 50%-50% beam splitter in air is wider (by a factor n_0 > 2), if light refraction from air to ZnS at the entrance face of the prism is accounted for using Snell's law.

4.3.5 50%-50% IR beam splitters with dual QWR in reflection and transmission.

50%-50% beam splitters that produce equal and opposite QWR in reflection and transmission have been reported recently[31]. In this work dual QWR retardation with similar and opposite signs in reflection and transmission is achieved. Table 6 lists a number of these monochromatic cube beam splitters.

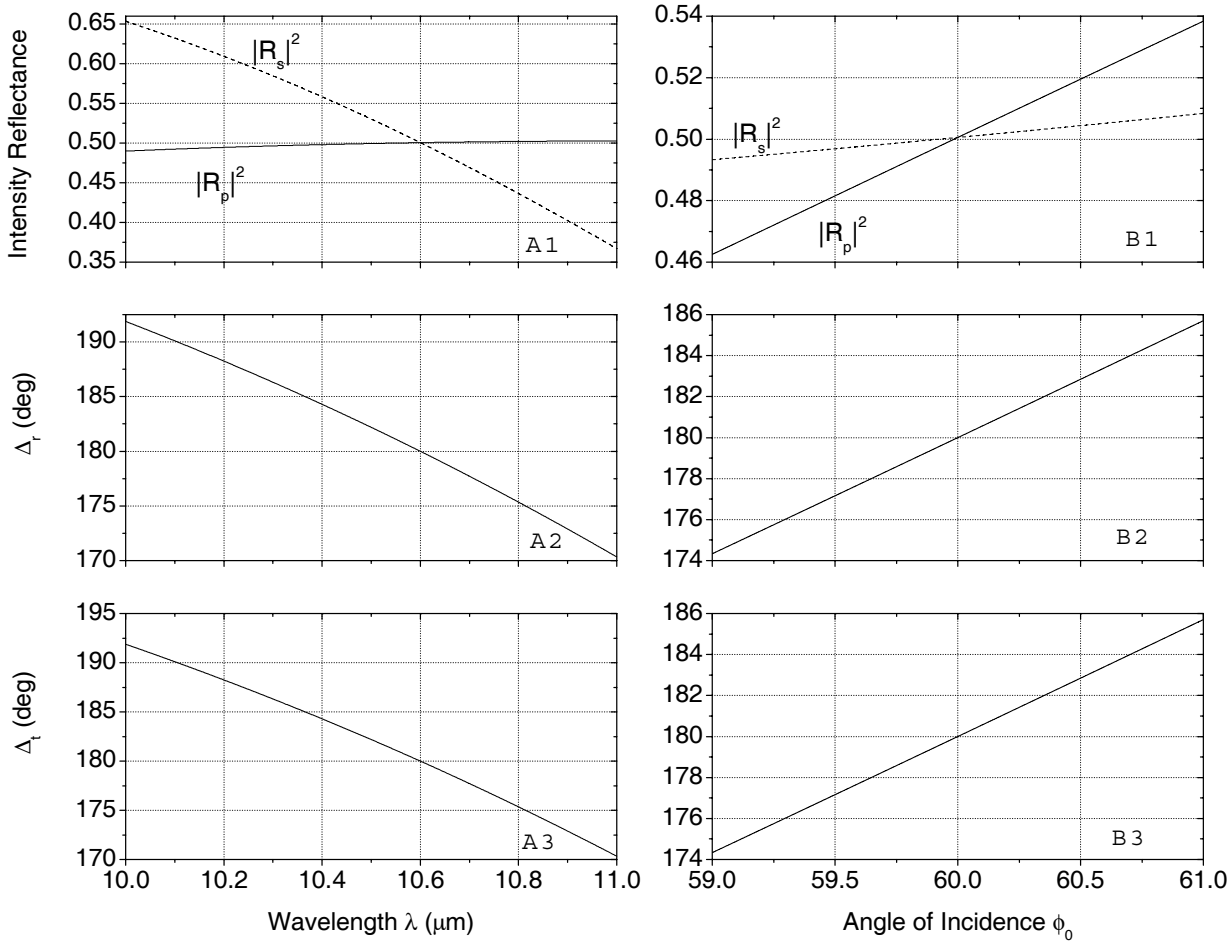

Figure 19 Panels (A1, A2, A3) and (B1, B2, B3) show the spectral and angular sensitivities, respectively, of a 50%-50% BS that achieves $\Delta_r = 180^o$ and $\Delta_r = 180^o$at the operating wavelength λ=10.6 μm and $\phi_0 = 60^o$. The design uses a 7-layer stack of PbTe (n_0 = 5.6315) and KBr (n_1 = 1.5251) thin films embedded in a high-index ZnS (n_2 = 2.1919) prism. The thicknesses of the KBr and PbTe thin films are 322.52 nm and 278.15 *nm*, respectively. Both the *p* and *s* reflectances $|R_p|^2$ and $|R_s|^2$ and the differential reflection and transmission phase shifts Δ_r and Δ_t are represented in this figure.

4.4 Periodic multilayer stacks as polarizers and PBS

The periodic multilayer PBS, Fig. 4, consists of periodically repeated low-index (n_1) – high-index (n_2) bilayers embedded in a high-index prism of refractive index n_0. The design procedure is outlined in Section 3.2. Various multilayer designs obtained by solving Eq. (20), their angular and spectral sensitivities are presented here.

4.4.1 BaF_2-PbTe Multilayer Polarizers Operating at $\lambda = 10.6$ μm

Figures 20, 21, 22, 23, 24 and 25 show Z_2 versus Z_1 such that $R_p = 0$ at angles of incidence ϕ_0 from 45° to 55° in steps of 1° for various periodic multilayer stacks with 4, 6, 8, 10, 12, 14, 16 and 18 layers of BaF_2 and PbTe thin films embedded in a ZnS substrate with refractive indices[37] $n_0 = 2.1919$ (ZnS), $n_1 = 1.3926$ (BaF_2), and $n_2 = 5.6314$ (PbTe) in the IR.

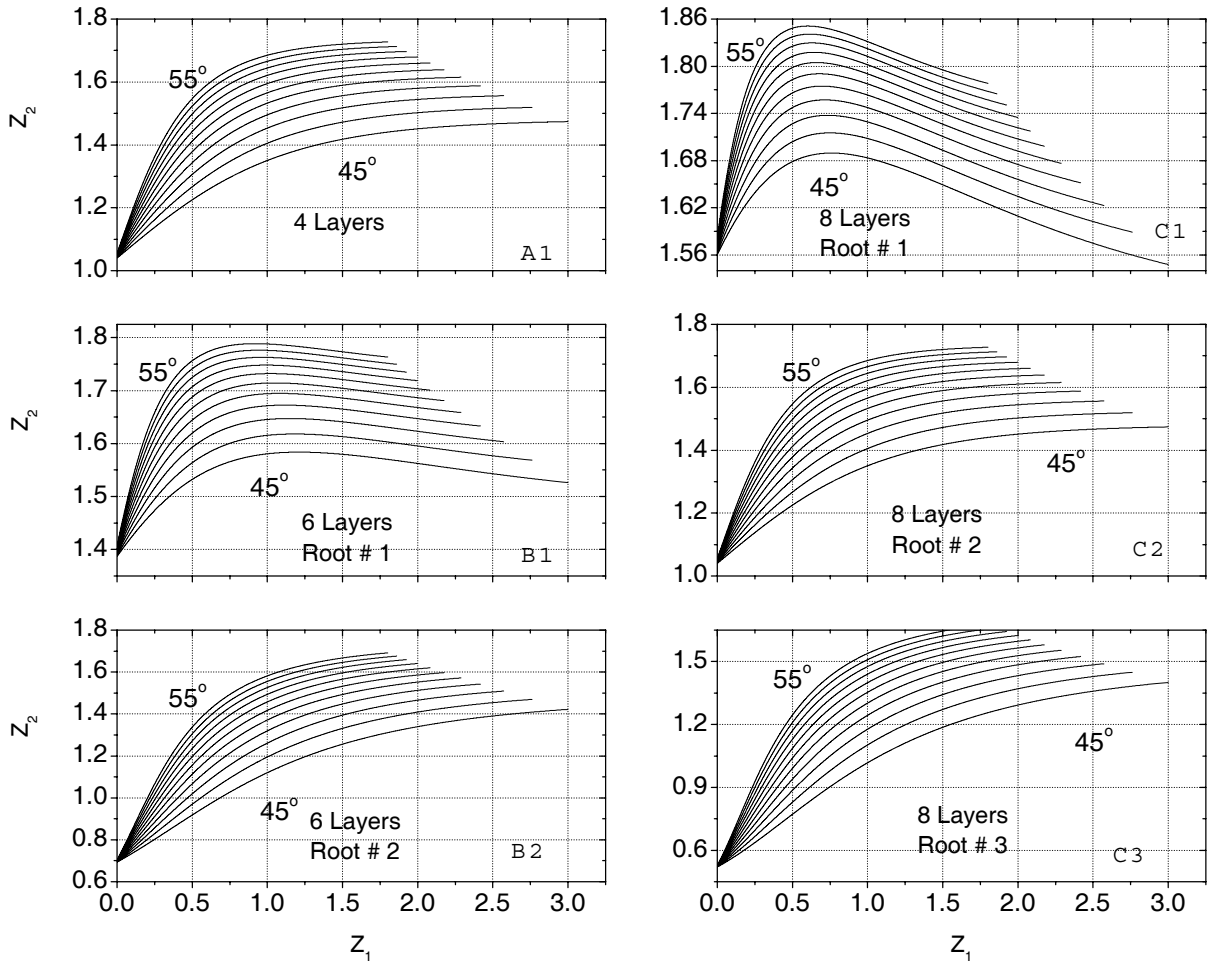

Figure 20 Z_2 versus Z_1 such that $R_p = 0$ at angles of incidence ϕ_0 from 45° to 55° in steps of 1° for periodic multilayer stacks with BaF_2 and PbTe thin films embedded in a ZnS substrate with refractive indices $n_0 = 2.1919$ (ZnS), $n_1 = 1.3926$ (BaF_2), and $n_2 = 5.6314$ (PbTe) in the IR at $\lambda = 10.6$ μm. Panel A1 corresponds to the 4-layer design with one root, Panels B1 and B2 correspond to the 6-layer design with 2 roots, while Panels C1, C2, and C3 correspond to the 8-layer design with 3 roots.

In Fig. 20, Panel A1 corresponds to the 4-layer design with one root, Panels B1 and B2 correspond to the 6-layer design with 2 roots, while Panels C1, C2, and C3 correspond to the 8-layer design with 3 roots. Figures 21, 22, 23, 24 and 25 show the corresponding results for the 10-, 12-, 14-, 16- and 18-layer designs with 4, 5, 6, 7 and 8 roots, respectively. Every point (Z_1, Z_2) on each curve in Figs. 20-25 represents a thickness solution that achieves a polarizer ($R_p = 0$) at the angle of incidence marked by that curve.

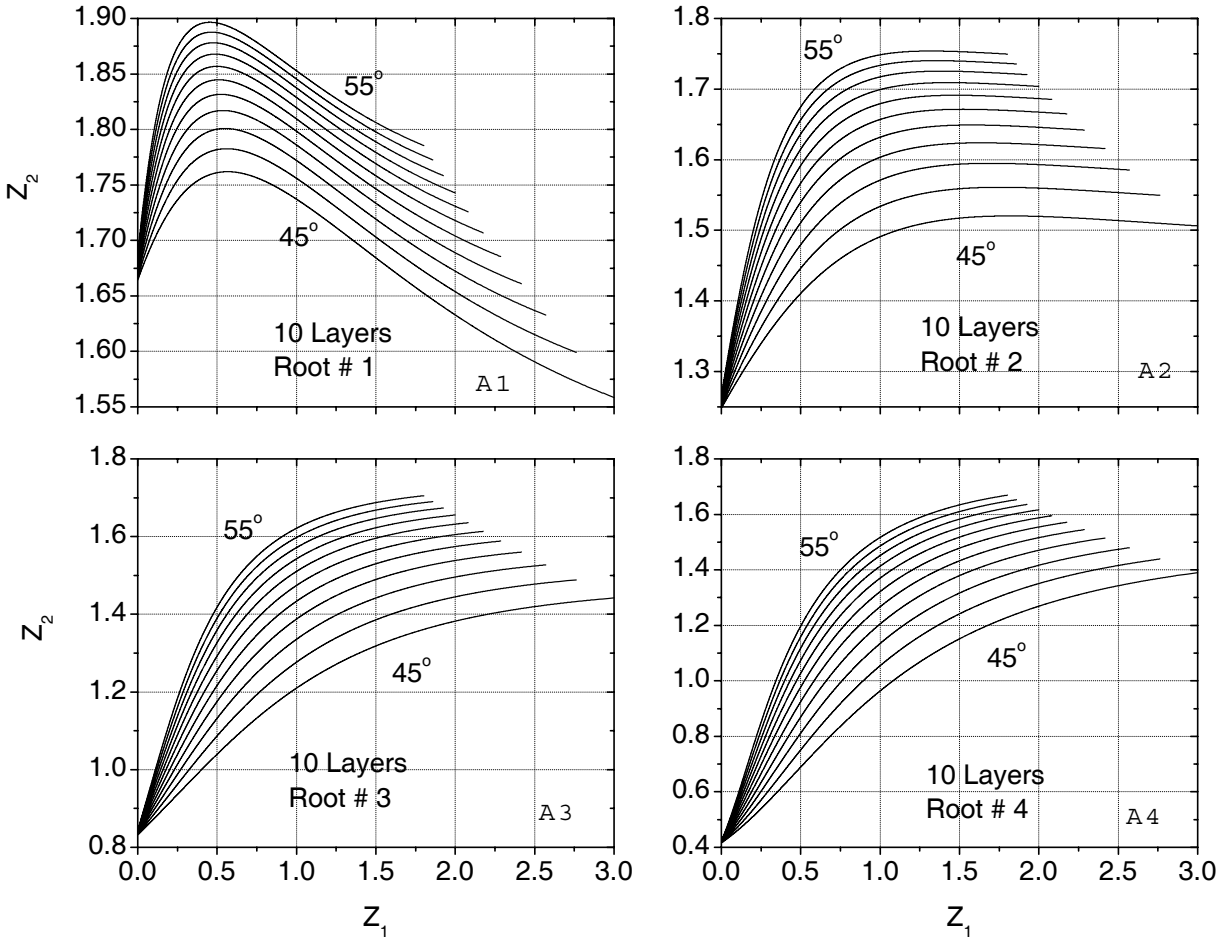

Figure 21 Z_2 versus Z_1 such that $R_p = 0$ at angles of incidence ϕ_0 from 45° to 55° in steps of 1° for the same material system as described in the caption of Fig. 20 for a 10-layer periodic multilayer design with 4 roots.

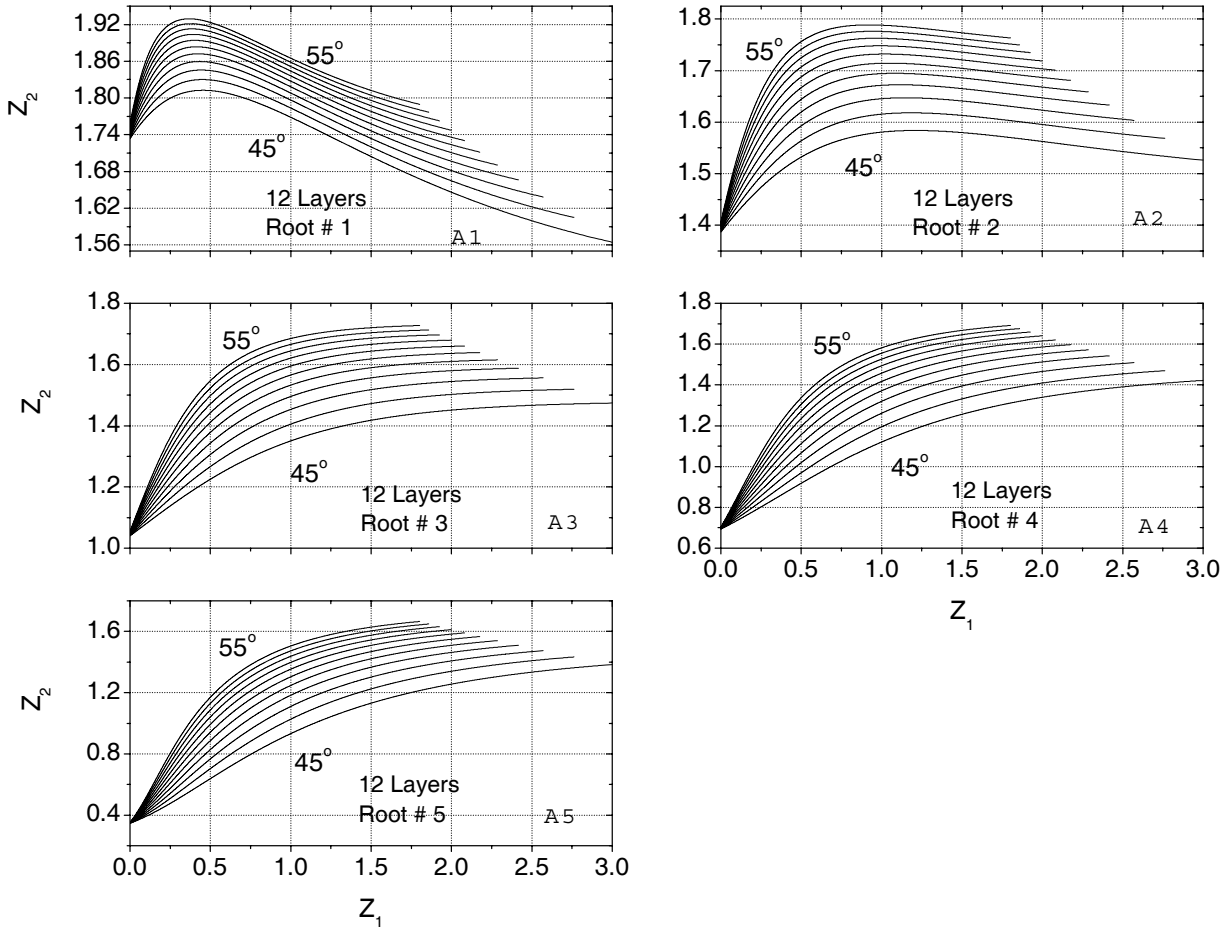

Figure 22 Z_2 versus Z_1 such that $R_p = 0$ at angles of incidence ϕ_0 from 45° to 55° in steps of 1° for the same material system as described in the caption of Fig. 20 for a 12-layer periodic multilayer design with 5 roots.

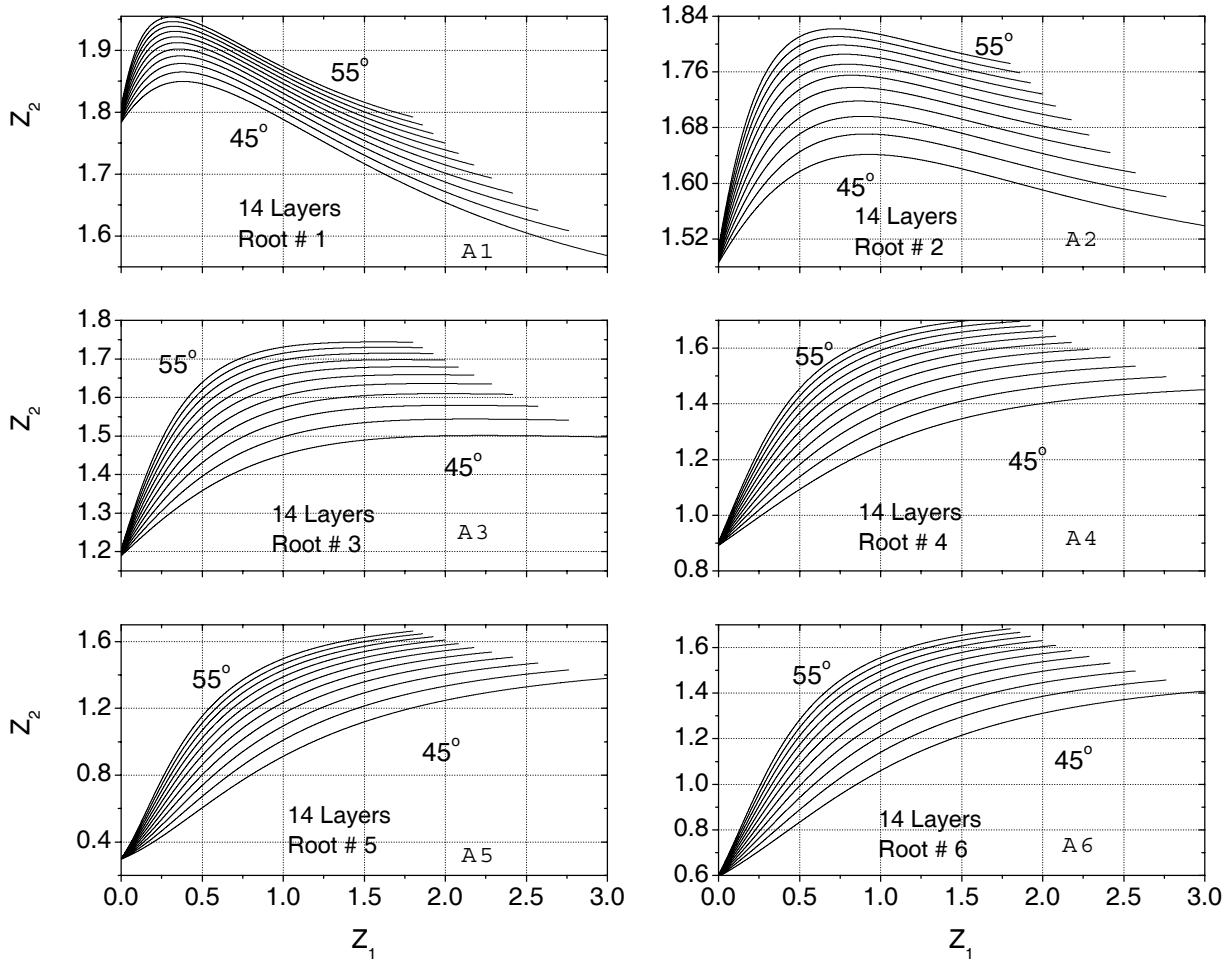

Figure 23 Z_2 versus Z_1 such that $R_p = 0$ at angles of incidence ϕ_0 from 45° to 55° in steps of 1° for the same material system as described in the caption of Fig. 20 for a 14-layer periodic multilayer design with 6 roots.

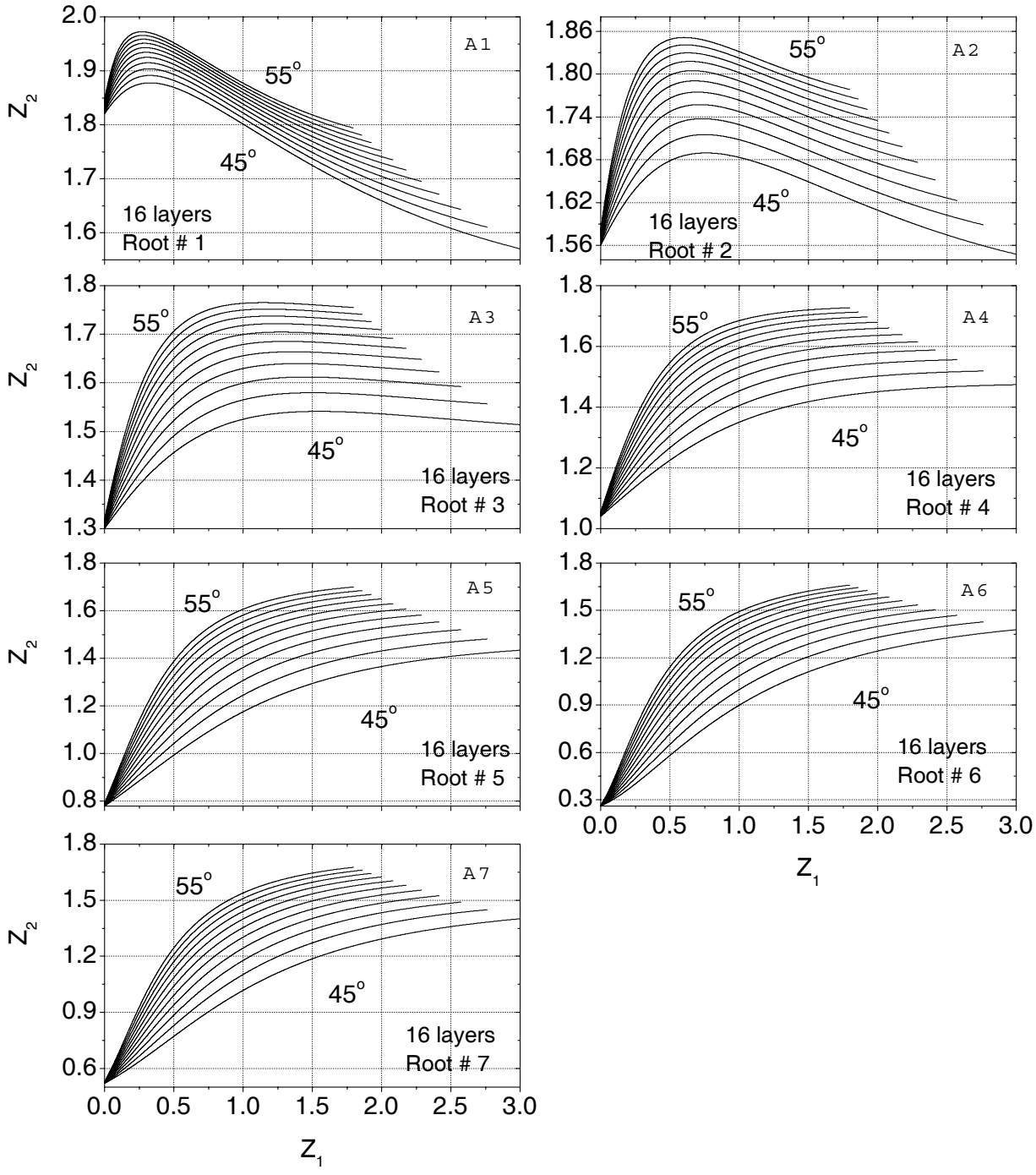

Figure 24 Z_2 versus Z_1 such that $R_p = 0$ at angles of incidence ϕ_0 from 45° to 55° in steps of 1° for the same material system as described in the caption of Fig. 20 for a 16-layer periodic multilayer design with 7 roots.

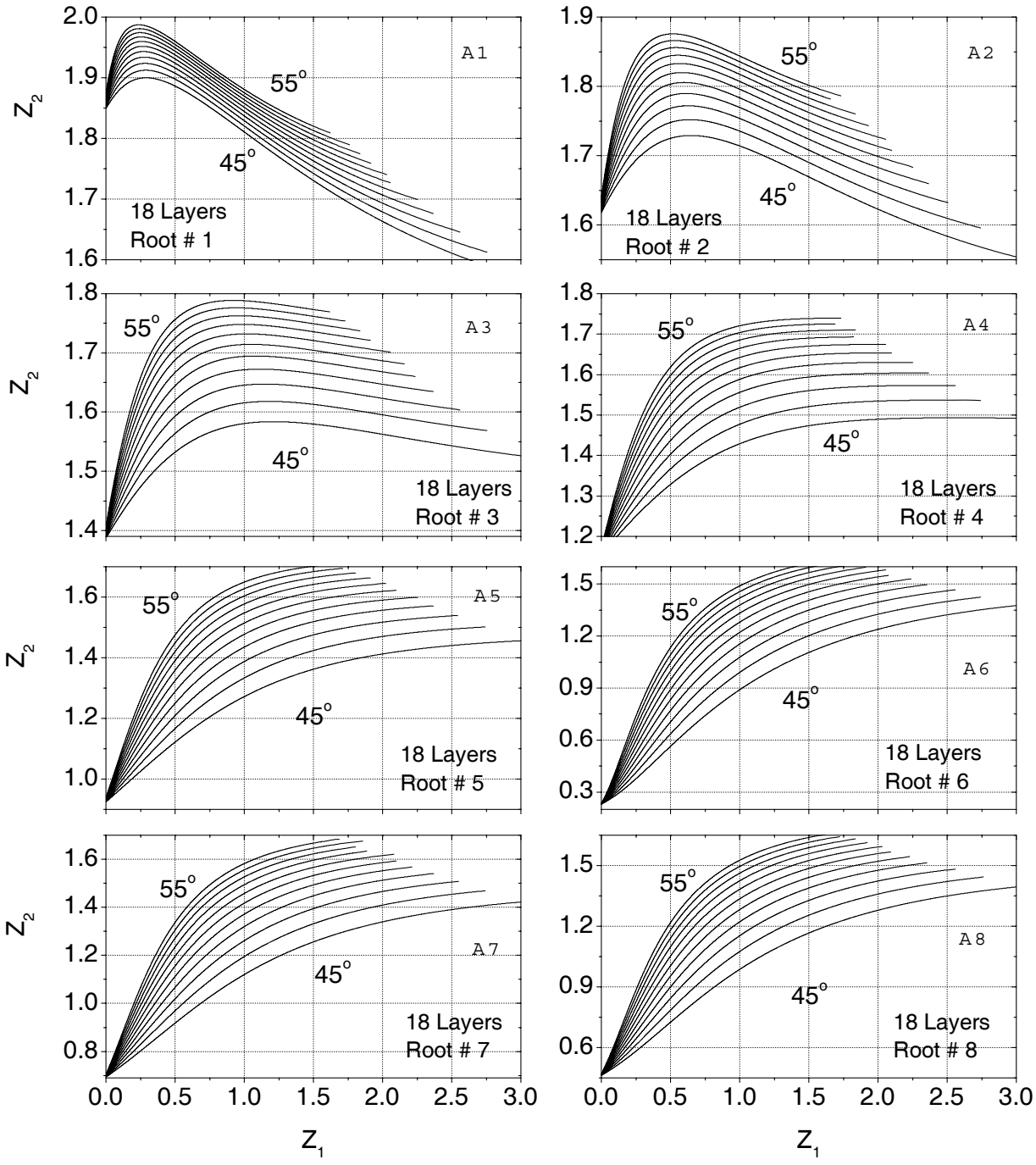

Figure 25 Z_2 versus Z_1 such that $R_p = 0$ at angles of incidence ϕ_0 from 45° to 55° in steps of 1° for the same material system as described in the caption of Fig. 20 for an 18-layer periodic multilayer design with 8 roots.

4.4.2 Angular sensitivity

In order to analyze the angular sensitivity of the embedded periodic multilayer devices, a specific thickness solution point (Z_1, Z_2) on the 45° curve with fixed normalized thickness for the low-index film $Z_1 = 2.0$ that yields high orthogonal *s* reflectance ($|R_s|^2 > 99.99\%$) was chosen for each root of each design from each panel in Figs. 20-25.

Table 8 Normalized (Z_1, Z_2) and metric (d_1, d_2) thicknesses corresponding to fixed $Z_1 = 2.0$ on each of the 45° curves in each panel of Figs. 20-25 for each root of the 4, 6, 8, 10, 12, 14, 16 and 18-layer designs.

# of Layers	Root #	Z_1	Z_2	d_1 (μm)	d_2 (μm)
4	1	2.0	1.45102	3.80583	0.68281
6	1	2.0	1.56250	3.80583	0.73527
	2	2.0	1.33954	3.80583	0.63035
8	1	2.0	1.60944	3.80583	0.75736
	2	2.0	1.45102	3.80583	0.68281
	3	2.0	1.29260	3.80583	0.60826
10	1	2.0	1.63282	3.80583	0.76836
	2	2.0	1.51971	3.80583	0.71514
	3	2.0	1.38232	3.80583	0.65048
	4	2.0	1.26922	3.80583	0.59726
12	1	2.0	1.64600	3.80583	0.77456
	2	2.0	1.56250	3.80583	0.73527
	3	2.0	1.45102	3.80583	0.68281
	4	2.0	1.25604	3.80583	0.59106
	5	2.0	1.33954	3.80583	0.63035
14	1	2.0	1.65412	3.80583	0.77838
	2	2.0	1.59040	3.80583	0.74840
	3	2.0	1.50044	3.80583	0.70607
	4	2.0	1.40160	3.80583	0.65955
	5	2.0	1.24792	3.80583	0.58724
	6	2.0	1.31164	3.80583	0.61722
16	1	2.0	1.65946	3.80583	0.78000
	2	2.0	1.60944	3.80583	0.75736
	3	2.0	1.53617	3.80583	0.72288
	4	2.0	1.45102	3.80583	0.68281
	5	2.0	1.24258	3.80583	0.58472
	6	2.0	1.36587	3.80583	0.64274
	7	2.0	1.29260	3.80583	0.60826

Table 8 continued…

18	1	2.0	1.66315	3.80583	0.78263
	2	2.0	1.62293	3.80583	0.76371
	3	2.0	1.56250	3.80583	0.73527
	4	2.0	1.48957	3.80583	0.70095
	5	2.0	1.41246	3.80583	0.66467
	6	2.0	1.23889	3.80583	0.58299
	7	2.0	1.33954	3.80583	0.63035
	8	2.0	1.27911	3.80583	0.60191

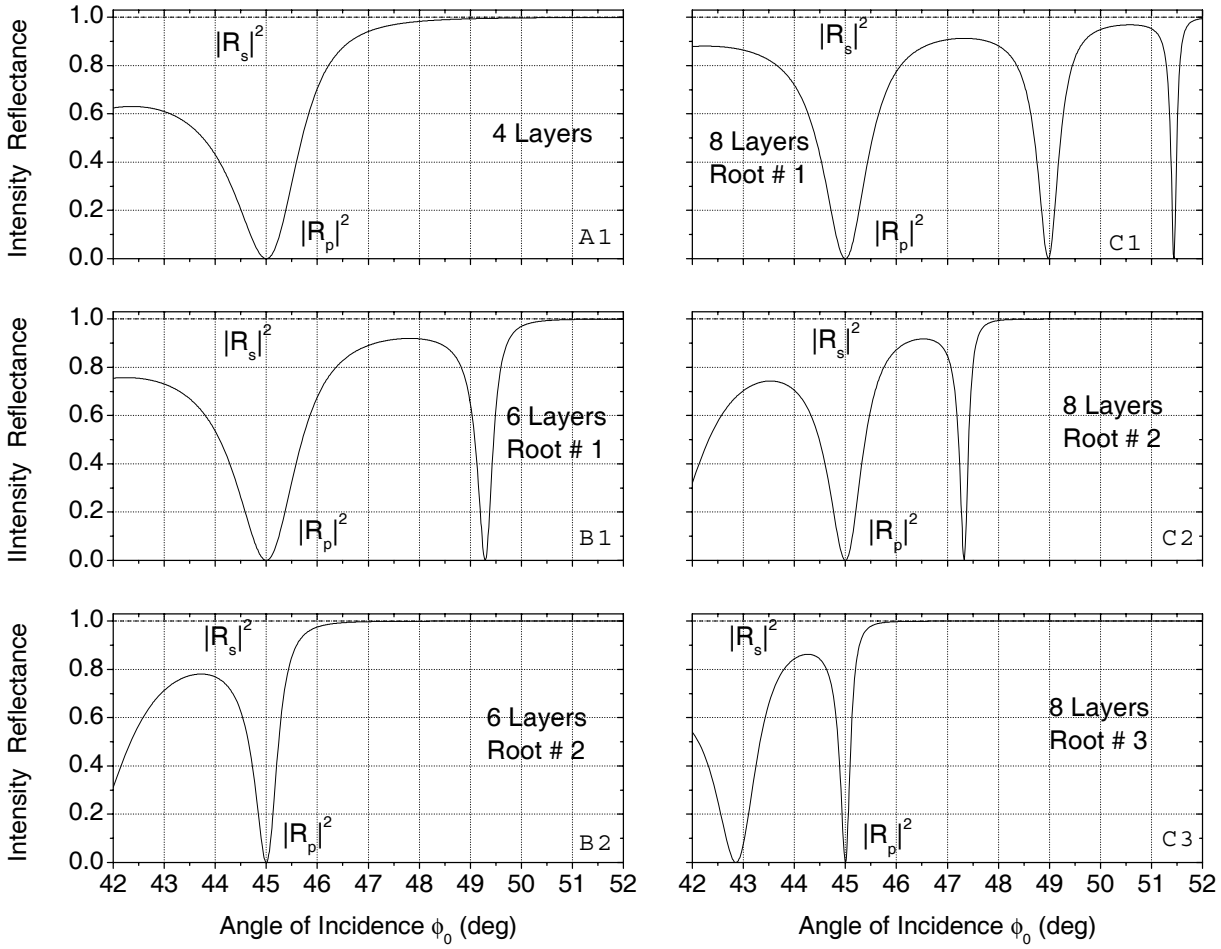

Figure 26 Reflectances $|R_p|^2$ and $|R_s|^2$ are plotted versus the angle of incidence ϕ_0 from 42° to 52° for periodic multilayer stacks with 4, 6 and 8 layers. Panel A1 corresponds to the 4-layer design with one root, Panels B1 and B2 correspond to the 6-layer design with 2 roots while Panels C1, C2, and C3 correspond to the 8-layer design with 3 roots. The material system is the same as given in the caption of Fig. 20 and the metric film thicknesses associated with different multilayer stack designs are listed in Table 8.

Table 8 lists the normalized and metric film thicknesses (Z_1, Z_2) and (d_1, d_2) obtained by the above procedure for the 4, 6, 8, 10, 12, 14, 16 and 18-layer designs. For the angle sensitivity, the metric film thicknesses (d_1, d_2) (obtained from Table 1) and wavelength $\lambda = 10.6$ μm for each root of each multilayer design are kept constant and the angle of incidence ϕ_0 is varied from 42° to 52°.

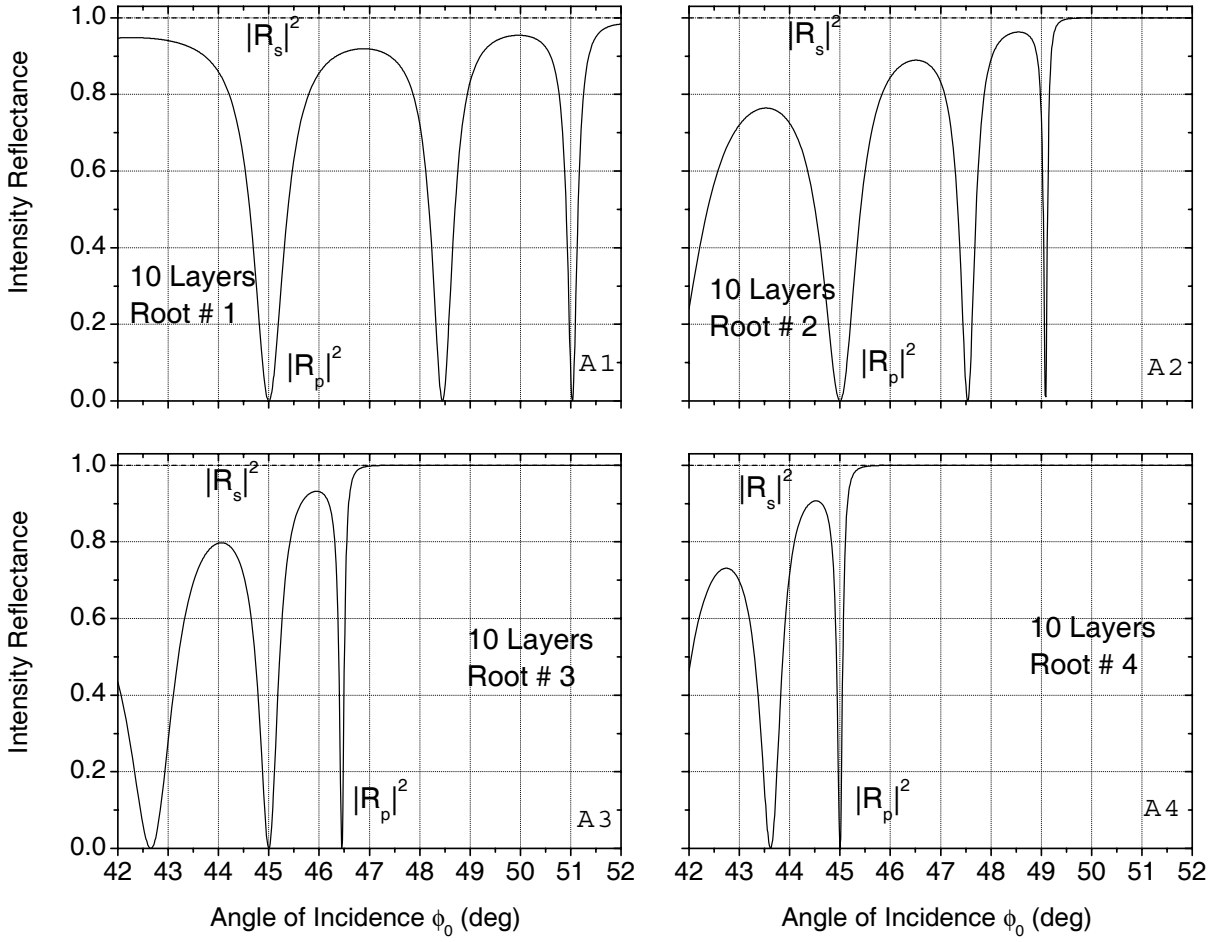

Figure 27 Reflectances $|R_p|^2$ and $|R_s|^2$ are plotted versus the angle of incidence ϕ_0 from 42° to 52° for a 10-layer periodic multilayer design. The material system is the same as given in the caption of Fig. 20 and the associated metric film thicknesses are listed in Table 8.

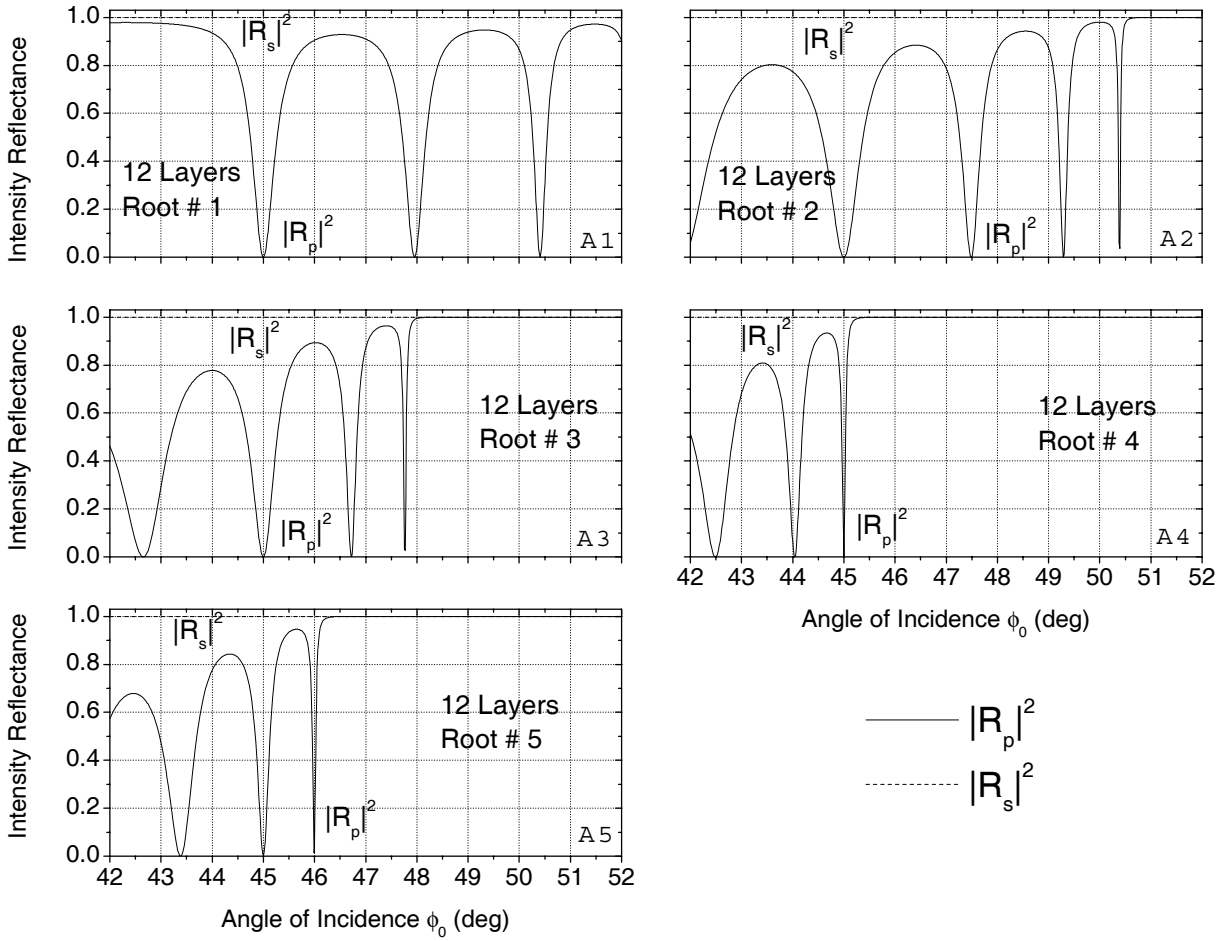

Figure 28 Reflectances $|R_p|^2$ and $|R_s|^2$ are plotted versus the angle of incidence ϕ_0 from 42° to 52° for a 12-layer periodic multilayer design. The material system is the same as given in the caption of Fig. 20 and the associated metric film thicknesses are listed in Table 8.

Figures 26, 27, 28, 29, 30 and 31 show plots for the *p* and *s* reflectances as a function of angle of incidence ϕ_0 for various multilayer stack designs with 4-to-18 layers. In Fig. 26, Panel A1 corresponds to the 4-layer design with one root, Panels B1 and B2 correspond to the 6-layer design with 2 roots, while Panels C1, C2, and C3 correspond to the 8-layer design with 3 roots. Figures 27, 28, 29, 30 and 31 show the corresponding results for the 10-, 12-, 14-, 16- and 18-layer designs with 4, 5, 6, 7 and 8 roots, respectively.

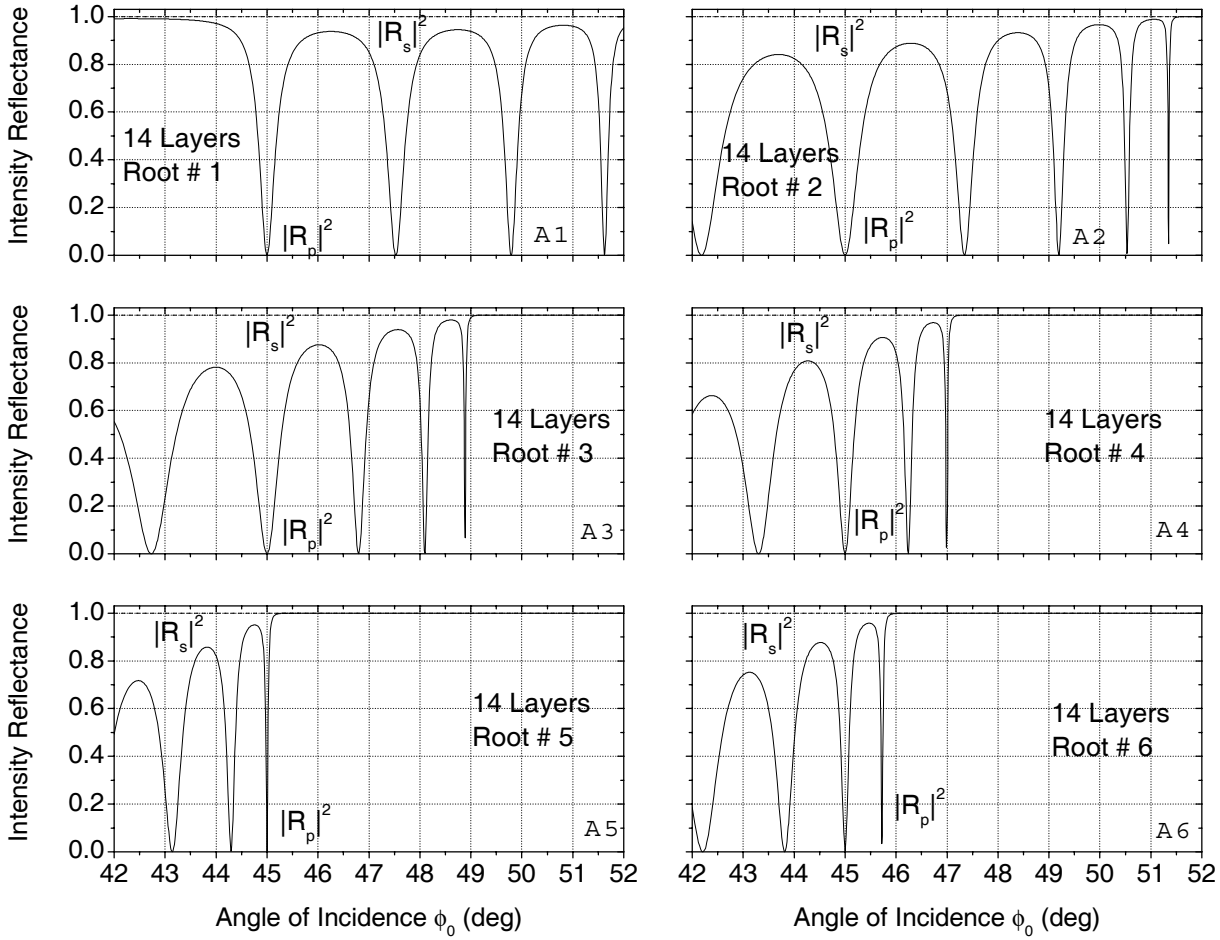

Figure 29 Reflectances $|R_p|^2$ and $|R_s|^2$ are plotted versus the angle of incidence ϕ_0 from 42° to 52° for a 14-layer periodic multilayer design. The material system is the same as given in the caption of Fig. 20 and the associated metric film thicknesses are listed in Table 8.

As the number of layers increase, $|R_s|^2$ remains dead flat at 1 while $|R_p|^2$ shows an oscillating behavior over a 10° internal field of view (42° to 52°). All the $|R_p|^2$ curves in each panel of Figs. 26 to 31 dip to zero at $\phi_0 = 45°$ because the associated film thickness solution set (d_1, d_2) $\leftrightarrow$ (Z_2 ,Z_1) lies on the 45° Z_2 vs Z_1 curve in the corresponding panel in Figs. 20 to 25. Hence, all the designs function as effective *s*-reflection polarizers ($|R_s|^2 > 99.9\%$) at several discrete angles in the range 42°-to-52° inside the prism.

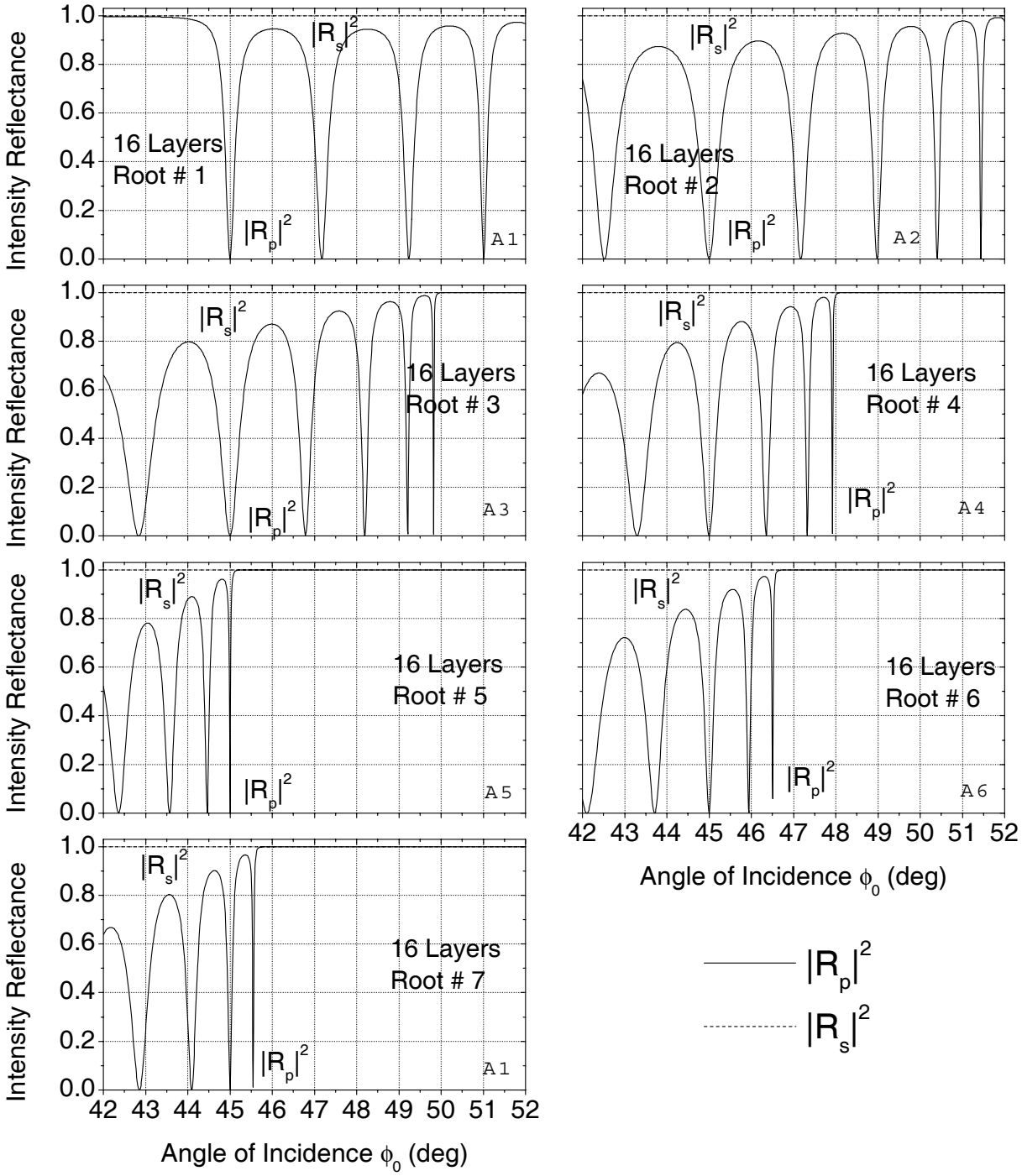

Figure 30 Reflectances $|R_p|^2$ and $|R_s|^2$ are plotted versus the angle of incidence ϕ_0 from 42° to 52° for a 16-layer periodic multilayer design. The material system is the same as given in the caption of Fig. 20 and the associated metric film thicknesses are listed in Table 8.

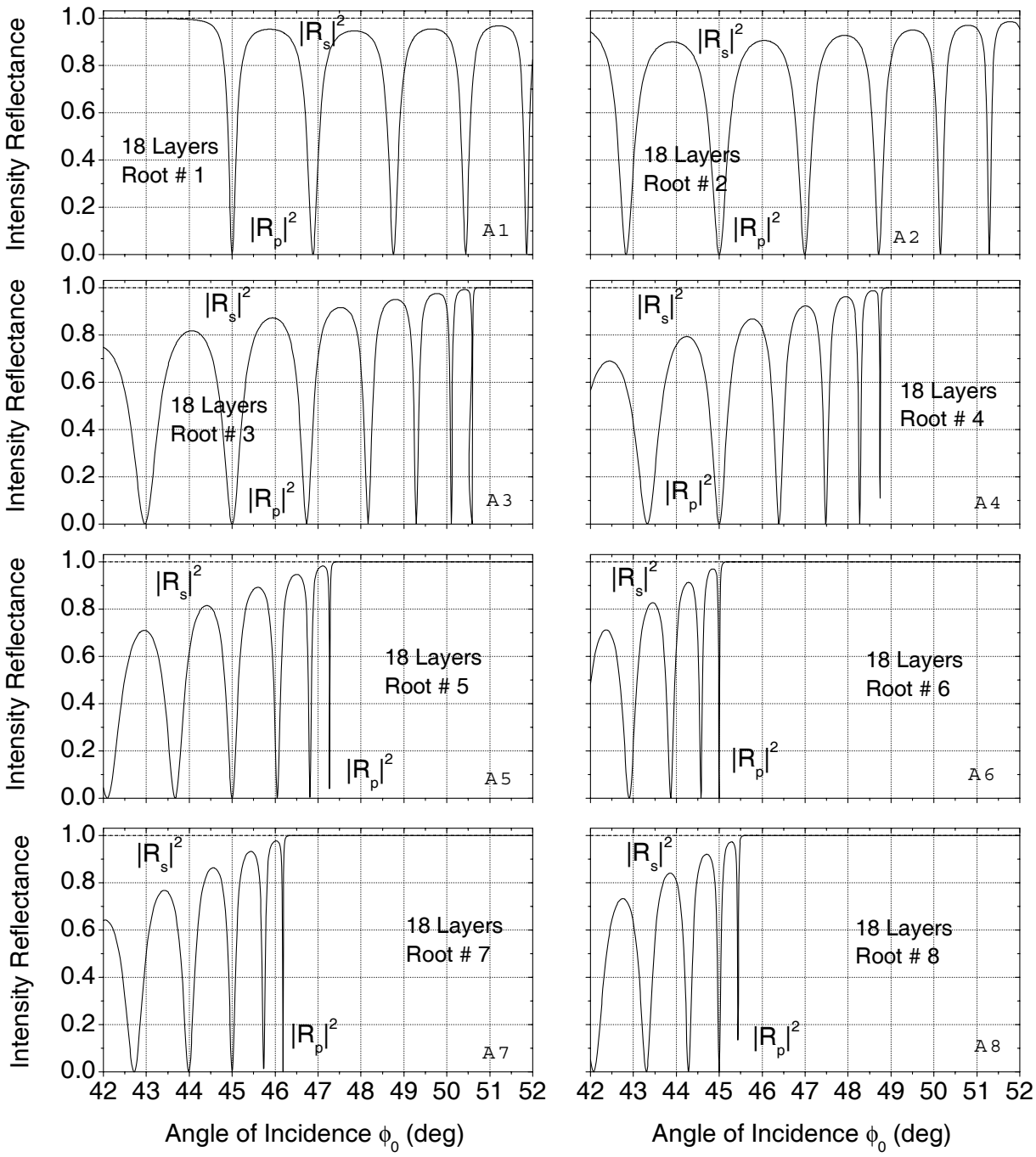

Figure 31 Reflectances $|R_p|^2$ and $|R_s|^2$ are plotted versus the angle of incidence ϕ_0 from 42° to 52° for a 18-layer periodic multilayer design. The material system is the same as given in the caption of Fig. 20 and the associated metric film thicknesses are listed in Table 8.

Designs with number of layers > 4 also function as polarizing beam splitters with extinction ratios > 30 dB in reflection and transmission at discrete multiple angles of incidence in the range $42^o < \phi_0 < 52^o$. Table 9 lists the ERs in reflection and transmission at all the discrete angles at which $|R_p|^2$ in each panel in Figs. 26 to 31 dips to zero.

Table 9 Discrete angles at which $|R_p|^2$ in each panel in Figs. 26 to 31 dips to zero.

# of Layers	Root #	ϕ_0 (deg)	ER_r (dB)	ER_t (dB)
4	1	45.00°	257.95	43.44
6	1	45.00°	259.71	65.77
		49.29°	49.55	74.14
	2	45.00°	247.52	69.38
8	1	45.00°	279.80	88.05
		49.98°	39.30	98.52
		51.44°	35.88	104.5
	2	45.00°	251.89	92.51
		47.33°	32.58	98.32
	3	42.85°	41.76	89.43
		45.00°	238.69	94.70
10	1	45.00°	244.49	110.42
		48.45°	44.28	121.91
		51.03°	32.09	129.84
	2	45.00°	252.51	115.03
		47.54°	38.44	123.11
		49.09°	19.69	127.75
	3	42.66°	42.64	111.12
		45.00°	247.20	118.53
		46.45°	28.97	122.92
	4	43.62°	49.52	115.79
		45.00°	237.7	119.91
12	1	45.00°	245.1	132.90
		47.95°	36.98	144.80
		50.41°	39.63	154.01
	2	42.00°	12.19	124.53
		45.00°	240.25	137.35
		47.49°	39.71	147.01
		49.29°	43.53	153.60
		50.39°	14.44	157.33
	3	42.65°	42.39	132.40
		45.00°	241.35	141.59
		46.72°	38.15	147.96
		47.77°	15.73	151.62
	4	42.49°	44.50	136.06
		44.04°	74.06	141.67
		45.00°	227.24	145.05
	5	43.38°	45.43	138.18
		45.00°	241.51	144.15
		45.99°	18.61	147.61

Table 9 continued…

14	1	45.00°	216.35	155.46
		47.53°	36.75	167.45
		49.79°	41.90	177.46
		51.62°	28.65	185.13
	2	42.18°	48.35	145.71
		45.00°	220.28	159.63
		47.34°	34.85	170.36
		49.19°	28.95	178.35
		50.53°	21.58	183.90
		51.35°	13.14	187.02
	3	42.73°	57.40	153.65
		45.00°	223.05	164.20
		46.80°	34.69	172.15
		48.10°	29.55	177.65
		48.89	11.72	180.60
	4	43.30°	42.50	160.18
		45.00°	227.78	167.66
		46.24°	47.59	172.92
		46.99°	15.70	175.90
	5	43.14°	45.65	162.52
		44.29°	28.25	167.28
		45.00°	224.52	170.16
	6	42.21°	45.65	157.60
		43.81°	33.83	164.55
		45.00°	243.79	169.53
		45.72°	14.55	172.33
16	1	45.00°	206.67	178.07
		47.17°	35.85	189.91
		49.24°	37.55	200.52
		51.01°	40.75	209.12
	2	42.52°	48.44	167.89
		45.00°	206.48	181.95
		47.17°	48.19	193.44
		48.98°	33.28	202.50
		50.41°	24.04	209.35
		51.44°	29.87	214.11
	3	42.84°	75.01	174.94
		45.00°	203.75	186.61
		46.79°	36.25	195.76
		48.19°	30.43	202.62
		49.21°	21.51	207.44
		49.82°	22.55	210.26

Table 9 continued…

16	4	43.30°	37.76	181.93
		45.00°	200.65	190.66
		46.35°	45.40	197.32
		47.33°	26.56	202.00
		47.92°	20.63	204.74
	5	42.36°	46.84	182.82
		43.57°	46.85	188.62
		44.46°	33.94	192.78
		45.00°	199.45	195.26
	6	42.11°	39.06	178.95
		43.71°	44.59	187.09
		45.00°	198.85	193.41
		45.94°	27.55	197.88
		46.51°	12.24	200.29
	7	42.85°	35.74	184.50
		44.09°	32.40	190.51
		45.00°	198.22	194.80
		45.55°	19.62	197.30
18	1	45.00°	191.02	200.72
		46.88°	66.54	212.32
		48.76°	36.87	223.25
		50.44°	31.71	232.55
		51.86°	26.33	240.11
	2	42.83°	49.7	190.45
		45.00°	191.94	204.32
		46.99°	45.05	216.28
		48.72°	35.79	226.13
		50.16°	27.13	233.95
		51.29°	29.29	239.90
	3	42.97°	44.90	196.44
		45.00°	192.84	208.92
		46.73°	33.36	219.00
		48.17°	28.55	227.03
		49.29°	40.01	233.06
		50.10°	31.56	237.31
		50.59°	29.53	239.83
	4	43.32°	37.18	203.45
		45.00°	192.01	213.34
		46.39°	51.58	221.17
		47.48°	25.78	227.10
		48.27°	25.84	231.31
		48.75°	9.61	233.32

Table 9 continued…

18	5	42.09°	43.67	200.00
		43.67°	58.25	209.28
		45.00°	189.61	216.76
		46.05°	32.39	222.50
		46.81°	24.13	226.52
		47.27°	13.85	228.78
	6	42.90°	45.48	209.34
		43.87°	32.01	214.50
		44.57°	26.80	218.13
		45.00°	185.47	220.35
	7	42.72°	36.12	206.40
		43.99°	35.08	213.48
		45.00°	187.36	218.95
		45.73°	18.65	222.75
		46.18°	37.64	225.16
	8	42.07°	40.46	204.20
		43.30°	52.76	210.98
		44.28°	27.55	216.22
		45.00°	185.87	220.01
		45.43°	8.69	221.60

4.4.3 Spectral sensitivity

The spectral sensitivities of the multilayer designs obtained in Section 4.4.2 are now analyzed. For the spectral sensitivity, the metric film thicknesses (d_1, d_2) (obtained from Table 8) and the angle of incidence $\phi_0 = 45^o$ for each root of each multilayer design are kept constant and the wavelength λ is scanned from 8 to 12 μm. The dispersion of all the materials in this spectral region is accounted for.[37] Figures 32, 33, 34, 35, 36 and 37 show plots for the *p* and *s* reflectances as a function of wavelength λ for various multilayer designs with 4-18 layers. In Fig. 32, Panel A1 corresponds to the 4-layer design with one root; Panels B1 and B2 correspond to the 6-layer design with 2 roots, while Panels C1, C2, and C3 correspond to the 8-layer design with 3 roots. Figures 33, 34, 35, 36 and 37 show the corresponding results for the 10-, 12-, 14-, 16- and 18-layer designs with 4, 5, 6, 7 and 8 roots, respectively. As the number of layers increase, $|R_s|^2$ remains dead flat at 1 while $|R_p|^2$ an oscillating nature over a 4 μm bandwidth

(8< λ <12 μ m). Hence broadband *s*-reflection polarizers ($|R_s|^2$ > 99.9%) over a 4 μ m bandwidth (8< λ <12 μ m) are readily achieved. For the Root # 1 of 14, 16 and 18 layer designs (Panel A1 of Figs. 35, 36 and 37) $|R_s|^2$ dips to zero thus yielding *orthogonal* polarizers (R_s = 0) or PBS at discrete wavelengths in the spectral range 8< λ <12 μ m. All the $|R_p|^2$ curves in each panel of Figs. 32-37 dip to zero at λ = 10.6 μ m, which is the design wavelength. Table 10 lists the ERs in reflection and transmission at all the discrete wavelengths at which $|R_p|^2$ or $|R_s|^2$ in each panel in Figs. 32 -37 dip to zero.

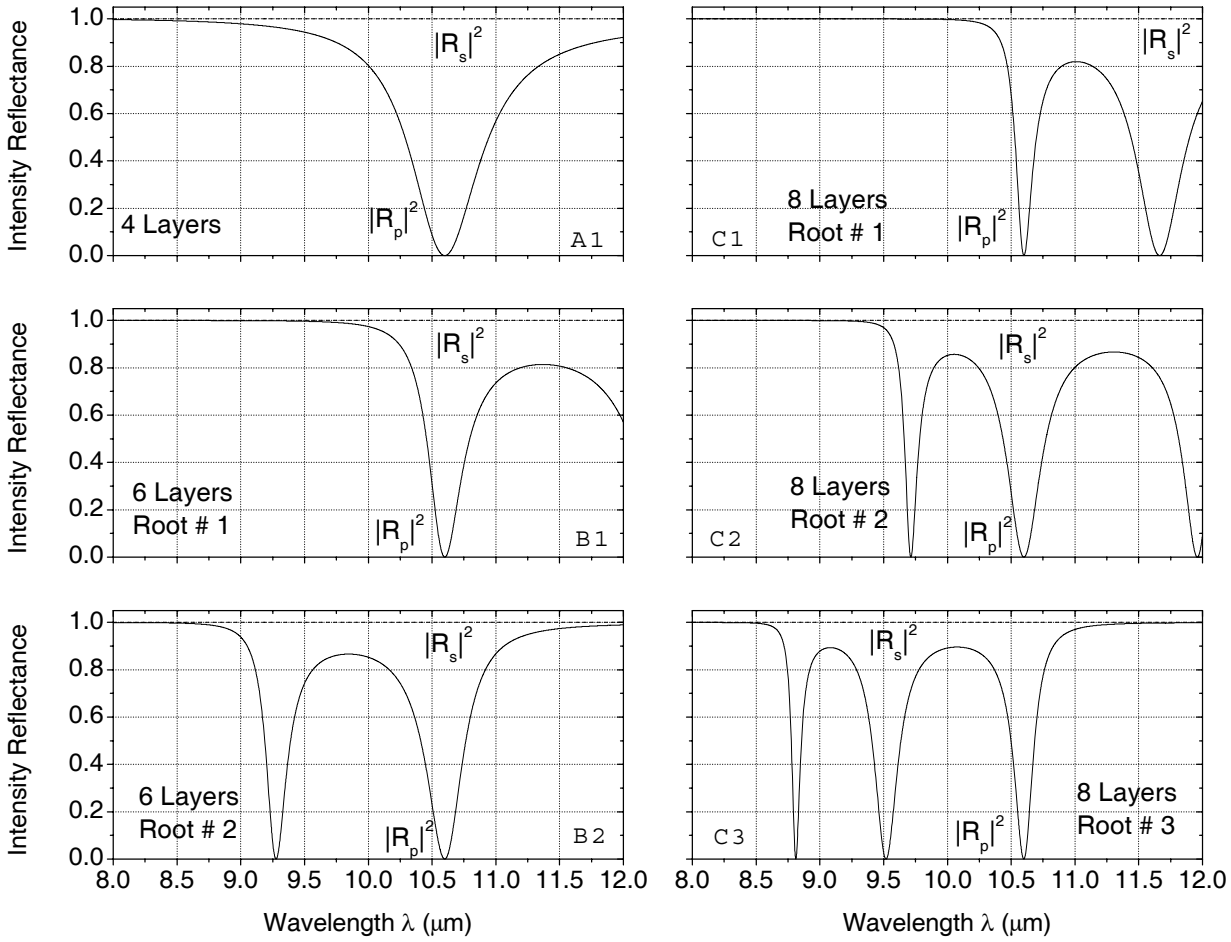

Figure 32 Reflectances $|R_p|^2$ and $|R_s|^2$ are plotted versus the wavelength 8 $\leq \lambda \leq$ 12 μm for periodic multilayer stacks with 4, 6 and 8 layers. Panel A1 corresponds to the 4-layer design, Panels B1 and B2 correspond to the 6-layer design while Panels C1, C2, and C3 correspond to the 8-layer design. The material system is the same as given in the caption of Fig. 20 and the metric film thicknesses associated with different multilayer stack designs are listed in Table 8.

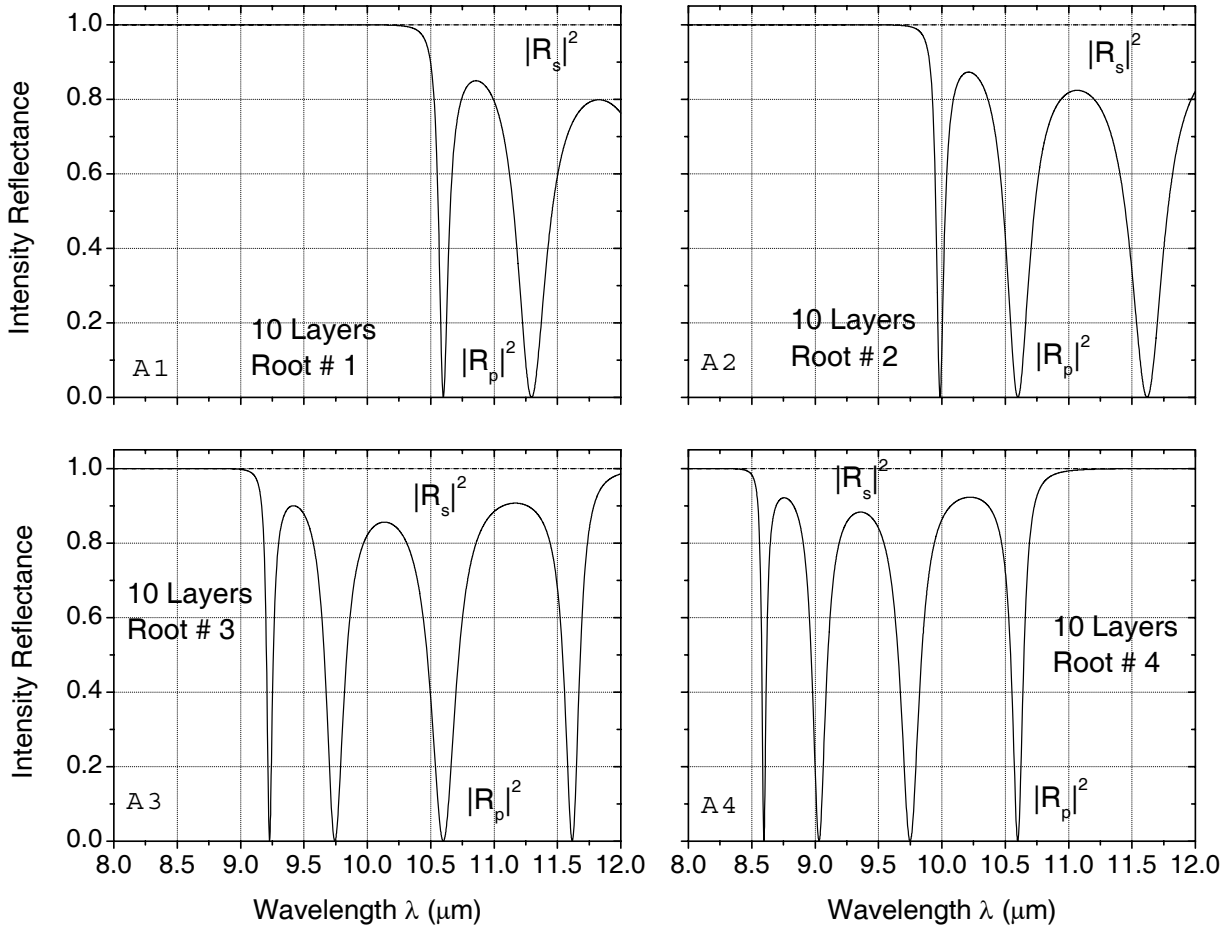

Figure 33 Reflectances $|R_p|^2$ and $|R_s|^2$ are plotted versus the wavelength $8 \leq \lambda \leq 12$ μm for a 10-layer periodic multilayer design. The material system is the same as given in the caption of Fig. 20 and the associated metric film thicknesses are listed in Table 8

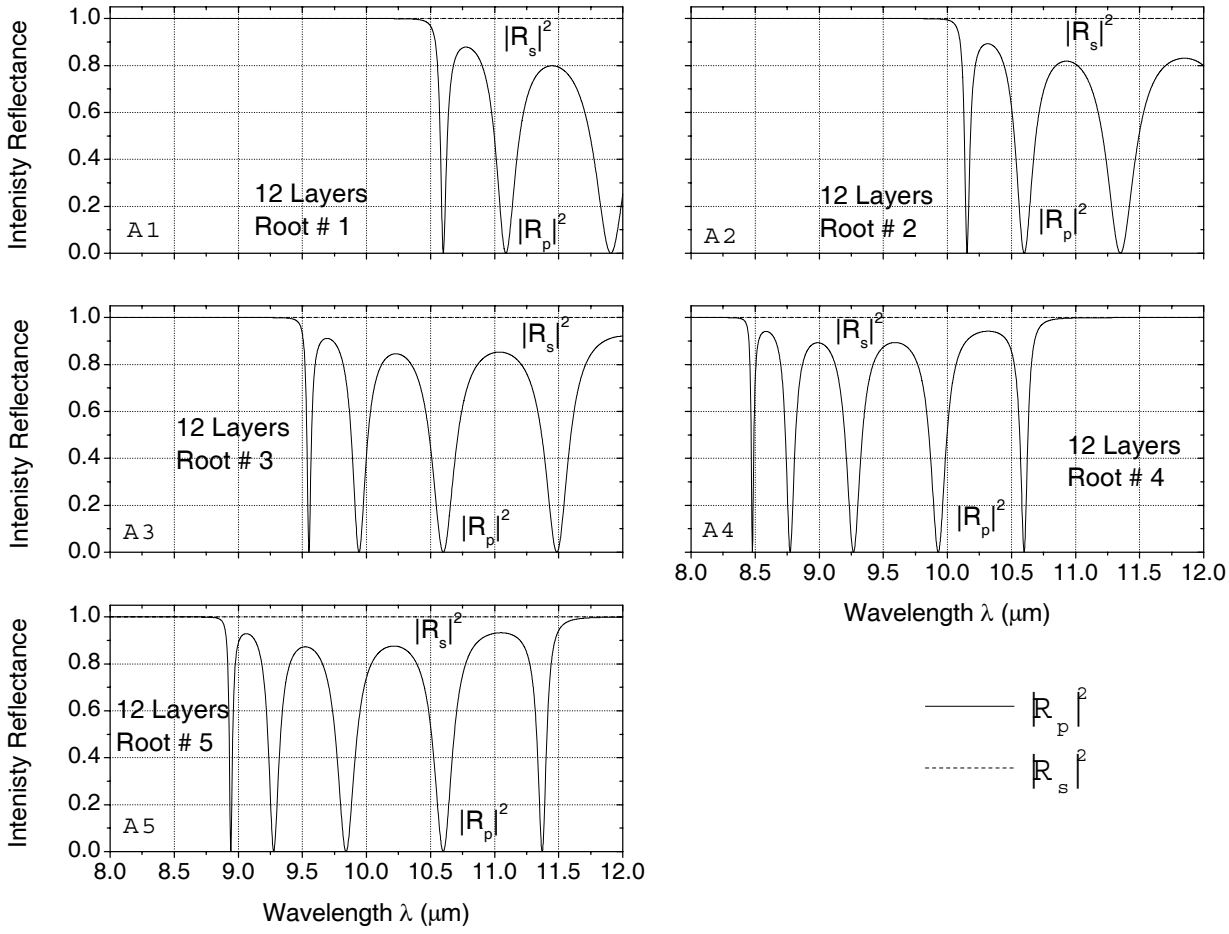

Figure 34 Reflectances $|R_p|^2$ and $|R_s|^2$ are plotted versus the wavelength $8 \leq \lambda \leq 12$ μm for a 12-layer periodic multilayer design. The material system is the same as given in the caption of Fig. 20 and the associated metric film thicknesses are listed in Table 8

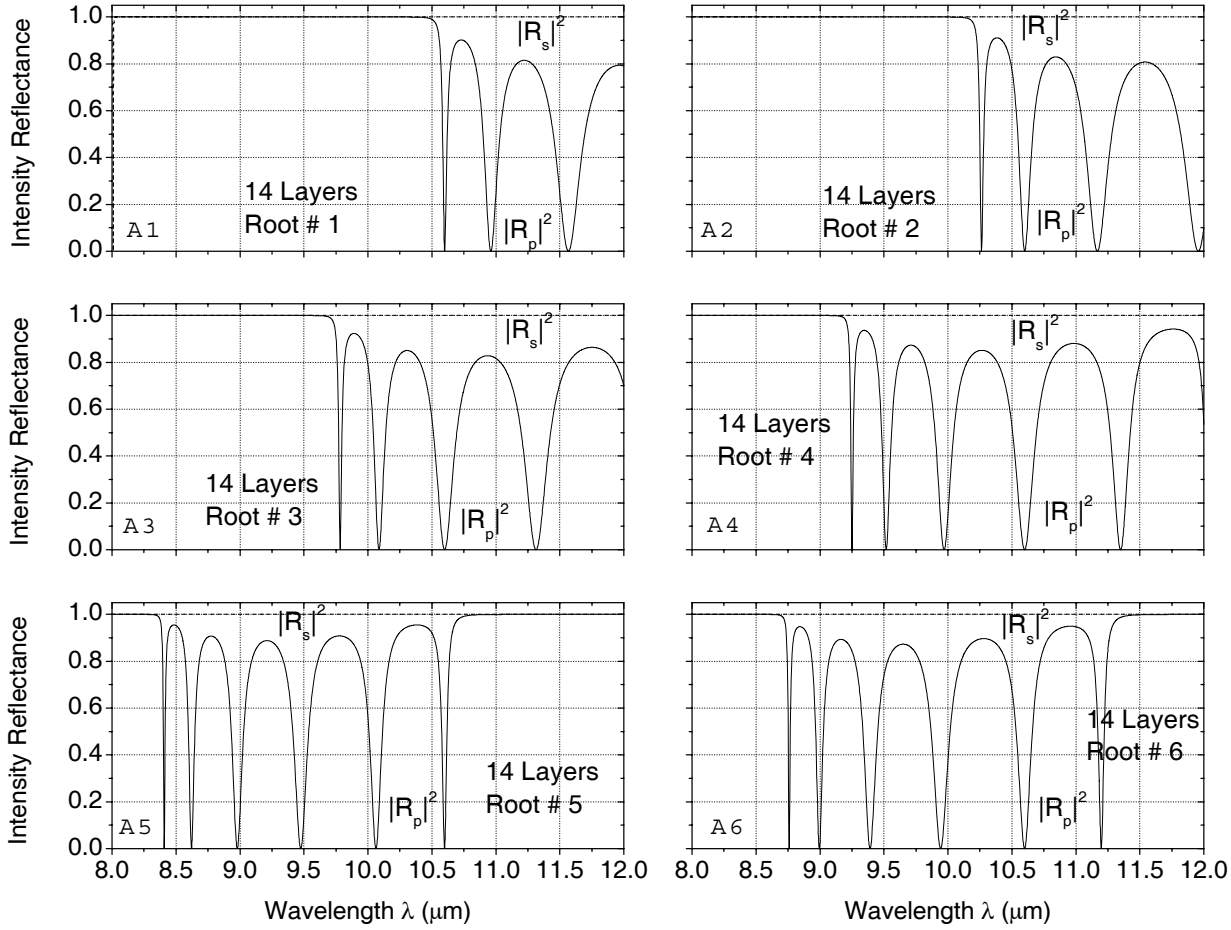

Figure 35 Reflectances $|R_p|^2$ and $|R_s|^2$ are plotted versus the wavelength $8 \leq \lambda \leq 12$ μm for a 14-layer periodic multilayer design. The material system is the same as given in the caption of Fig. 20 and the associated metric film thicknesses are listed in Table 8.

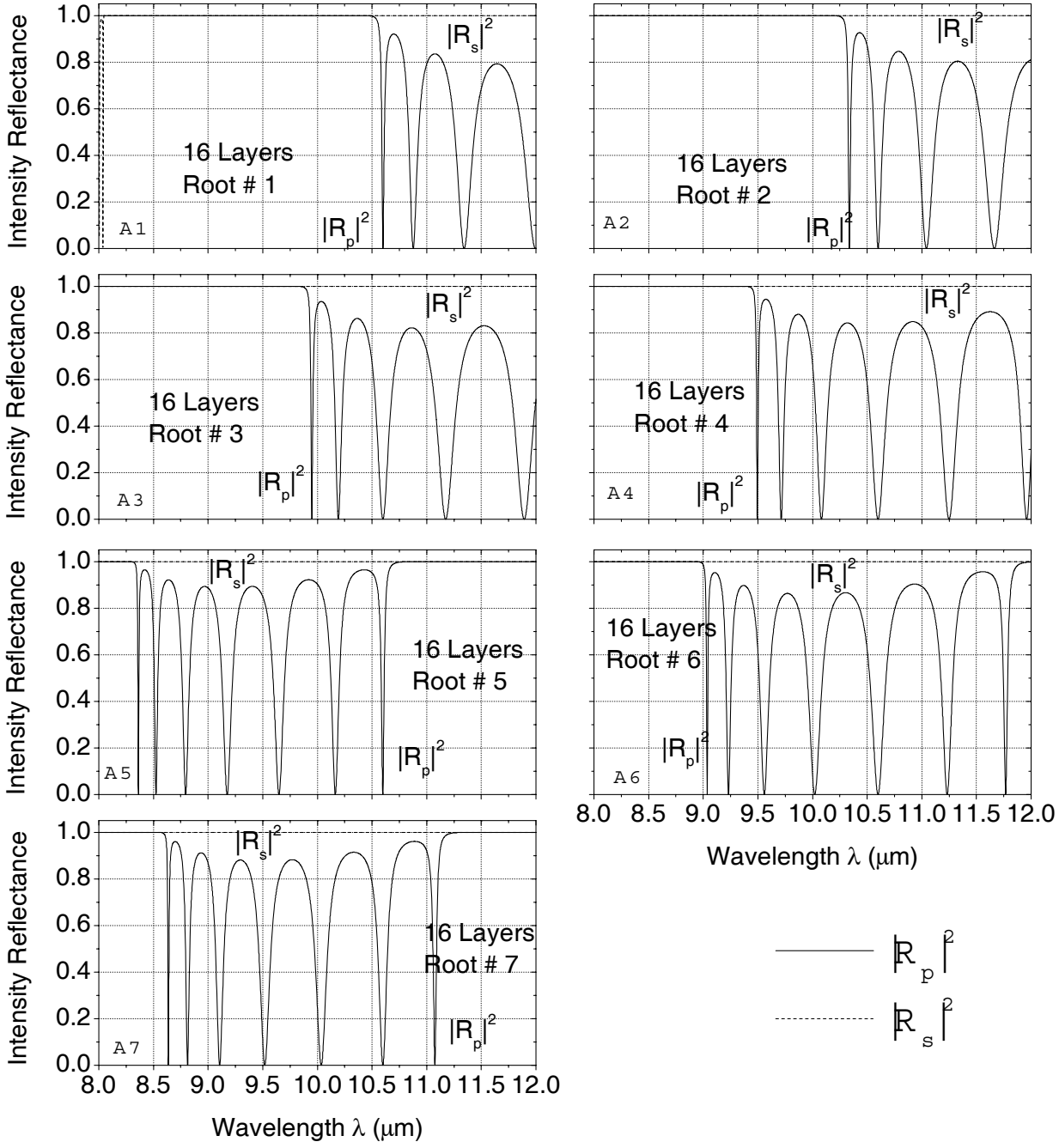

Figure 36 Reflectances $|R_p|^2$ and $|R_s|^2$ are plotted versus the wavelength $8 \leq \lambda \leq 12$ μm for a 16-layer periodic multilayer design. The material system is the same as given in the caption of Fig. 20 and the associated metric film thicknesses are listed in Table 8.

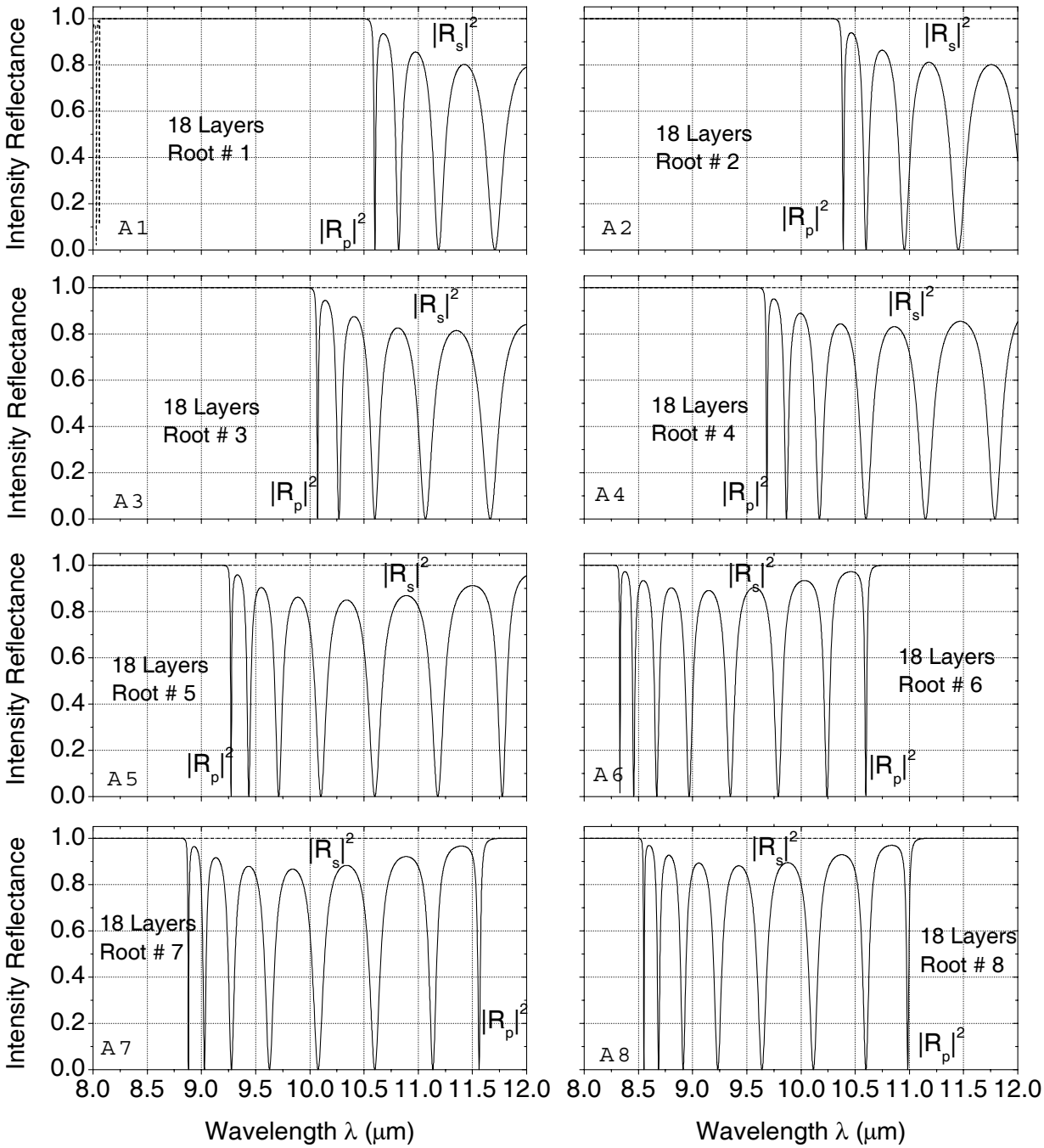

Figure 37 Reflectances $|R_p|^2$ and $|R_s|^2$ are plotted versus the wavelength $8 \leq \lambda \leq 12$ μm for a 18-layer periodic multilayer design. The material system is the same as given in the caption of Fig. 20 and the associated metric film thicknesses are listed in Table 8

Table 10 Discrete wavelengths at which $|R_p|^2$ or $|R_s|^2$ in each panel in Figs. 32 to 37 dip to zero.

# of Layers	Root #	λ (μm)	ER_r (dB)	ER_t (dB)
4	1	10.600	60.14	65.78
6	1	10.600	60.14	65.78
	2	9.277	51.72	72.05
		10.600	75.00	69.34
8	1	10.600	62.14	88.05
		11.664	53.58	87.35
	2	9.713	44.68	93.69
		10.600	51.60	92.52
		11.959	54.55	88.45
	3	8.812	40.10	100.32
		9.519	52.80	98.75
		10.600	50.23	94.71
10	1	10.600	67.63	110.43
		11.296	64.69	110.51
	2	9.985	46.60	115.33
		10.600	53.24	115.04
		11.619	58.81	112.47
	3	9.228	36.29	122.04
		9.744	60.28	121.33
		10.600	57.54	118.55
		11.617	46.08	113.88
	4	8.596	53.44	128.36
		9.031	54.53	127.33
		9.749	73.85	124.42
		10.600	41.75	119.92
12	1	10.600	73.31	132.91
		11.088	63.23	133.35
		11.907	54.92	132.21
	2	10.153	33.89	137.19
		10.600	54.12	137.36
		11.35	54.29	136.00
	3	9.551	34.25	143.44
		9.942	54.00	143.25
		10.600	48.08	141.59
		11.485	49.66	137.80
	4	8.479	31.19	156.22
		8.773	43.50	155.49
		9.267	49.87	153.41
		9.928	42.23	149.60
		10.600	35.89	145.06

Table 10 continued…

12	5	8.941	30.28	150.42
		9.277	45.70	149.90
		9.840	43.32	148.00
		10.600	68.97	144.16
		11.371	40.69	139.44
14	1	8.010	-33.91	-120.73
		10.600	58.54	155.47
		10.961	44.34	156.06
		11.567	65.71	155.67
	2	10.263	34.88	159.25
		10.600	54.94	159.64
		11.168	54.52	159.05
		11.957	48.90	156.55
	3	9.783	35.71	164.96
		10.087	49.54	165.08
		10.600	49.32	164.21
		11.314	49.63	161.54
	4	9.250	38.64	171.82
		9.518	47.82	171.65
		9.970	47.73	170.50
		10.600	51.53	167.68
		11.350	49.70	163.19
	5	8.408	41.83	184.00
		8.621	45.48	183.43
		8.979	77.84	181.88
		9.475	54.04	178.89
		10.063	64.88	174.56
		10.600	31.28	170.18
	6	8.759	32.19	178.69
		8.995	40.98	178.28
		9.392	41.28	176.88
		9.943	68.04	173.96
		10.600	51.09	169.55
		11.199	33.04	165.00
16	1	8.004	-12.10	-139.06
		8.039	-24.39	-138.29
		10.600	51.86	178.08
		10.877	53.92	178.73
		11.343	65.00	178.80
		11.996	53.10	177.37
	2	10.337	61.64	181.46
		10.600	56.11	181.96
		11.042	45.73	181.86
		11.664	47.56	180.30

Table 10 continued…

16	3	9.949	28.24	186.66
		10.192	39.12	186.95
		10.600	50.00	186.62
		11.174	52.41	184.88
		11.892	48.62	181.35
	4	9.495	40.96	193.18
		9.713	38.66	193.23
		10.081	42.18	192.62
		10.600	45.58	190.67
		11.294	46.75	187.07
		11.959	48.53	182.20
	5	8.362	37.01	211.70
		8.523	37.59	211.23
		8.794	40.17	210.03
		9.174	42.60	207.69
		9.648	42.14	204.03
		10.164	61.16	199.45
		10.600	60.45	195.25
	6	9.036	36.06	200.24
		9.231	37.48	200.07
		9.559	48.83	199.20
		10.020	41.49	197.08
		10.600	58.04	193.43
		11.232	65.27	188.63
		11.767	48.12	184.19
	7	8.637	30.10	206.85
		8.812	34.08	206.50
		9.106	41.07	205.43
		9.519	46.77	203.17
		10.035	44.19	199.50
		10.600	44.21	194.82
		11.075	37.57	190.53
18	1	8.031	-16.83	-156.76
		8.059	-9.57	-155.43
		10.600	47.15	200.73
		10.819	37.82	201.39
		11.188	59.63	201.74
		11.707	46.33	200.98
	2	10.390	24.08	203.75
		10.600	58.00	204.33
		10.954	43.56	204.53
		11.452	55.86	203.65

Table 10 continued…

18	3	10.072	25.33	208.53
		10.269	34.85	208.93
		10.600	50.59	208.93
		11.067	62.21	207.88
		11.663	45.27	205.28
	4	9.685	26.03	214.63
		9.866	59.19	214.84
		10.170	44.17	214.60
		10.600	46.58	213.35
		11.149	45.75	210.62
		11.789	53.25	206.40
	5	9.273	26.03	221.56
		9.437	47.93	221.56
		9.713	42.63	221.09
		10.102	47.43	219.62
		10.600	48.08	216.79
		11.180	51.06	212.56
		11.775	47.56	207.56
	6	8.330	17.87	239.26
		8.457	38.50	238.94
		8.669	40.49	237.98
		8.968	49.54	236.11
		9.349	39.74	233.08
		9.790	44.15	228.96
		10.241	36.66	224.29
		10.600	24.15	220.36
	7	8.880	32.13	228.62
		9.028	42.10	228.45
		9.277	42.18	227.75
		9.628	46.54	226.11
		10.076	53.97	223.18
		10.600	65.46	218.97
		11.135	40.52	214.08
		11.562	43.54	209.91
	8	8.551	37.49	234.90
		8.686	53.71	235.60
		8.913	45.91	233.74
		9.232	39.51	231.95
		9.640	71.60	228.96
		10.114	57.32	224.79
		10.600	39.47	220.03
		10.985	34.50	216.00

5. Summary and Conclusions

Polarizers and PBS that employ centro-symmetric multilayer stacks embedded in a high-index prism are thoroughly examined by using analytical and numerical calculations. All possible solutions (infinite in number) that suppress the *p* or *s* polarization in reflection are determined. Conditions for good operation of these devices over an extended range of incidence angles are demonstrated.

It has been demonstrated that embedded centro-symmetric multilayer structure that operates under FTIR conditions can achieve QWR or HWR with near-complete transmission for the *p* and *s* polarizations with good spectral response and limited angular sensitivity. The sensitivity of these devices to film thickness errors is also considered.

Also, it has been demonstrated that FTIR by an embedded centro-symmetric multilayer stack can achieve various 50%-50% beam splitters listed in Table 1. Monochromatic 50%-50% cube beam splitters operating at visible, lightwave communications range and at the CO_2-laser wavelength are designed. The angular and spectral sensitivities of some of these devices are also considered.

Polarizers and PBS that employ periodic multilayer stacks embedded in a high-index prism operating under FTIR conditions are also designed. All possible solutions (infinite in number) that suppress the *p* or *s* polarization in reflection are determined. These devices act as multi-angle and multi-wavelength polarizing beam splitters in the IR.

References

1. P. B. Clapham, M. J. Downs, and R. J. King, “Some applications of thin films to polarization devices,” Appl. Opt. **8**, 1965-1974 (1969).

2. W. W. Buchman, S. J. Holmes, and F. J. Woodberry, “Single-wavelength thin-film polarizers,” J. of Opt. Soc. of Am. **61**, 1604-1606 (1971).

3. D. Lees and P. Baumeister, “Versatile frustrated-total-reflection polarizer for the infrared,” Opt. Lett. **4**, 66-67 (1979).

4. J. A. Dobrowolski and A. Waldorf, "High-Performance Thin Film Polarizer for the UV and Visible Spectral Regions," Appl. Opt. **20**, 111-116 (1981).

5. H. A. Macleod, *Thin Film Optical Filters*, 2nd edition (McGraw-Hill, New York, 1986).

6. R. M. A. Azzam, “Polarizing beam splitters for infrared and millimeter waves using single-layer-coated dielectric slab or unbacked films,” Appl. Opt. **25**, 4225-4227 (1986).

7. M. Gilo and K. Rabinovitch, “Design parameters of thin-film cubic-type polarizers for high power lasers,” Appl. Opt. **26**, 2518-2521 (1987).

8. B. V. Blanckenhagen, “Practical layer design for polarizing beam-splitter cubes,” Appl. Opt. **45**, 1539-1543 (2006).

9. J. Mouchart, J. Begel, and E. Duda, “Modified MacNeille cube polarizer for a wide angular field,” Appl. Opt. **28**, 2847-2853 (1989)

10. S. M. MacNeille, “Beam splitter,” U.S. patent 2,403,731 (6 July 1946).

11. M. Banning, “Practical methods of making and using multi-layer filters,” J. Opt. Soc. Am. **37**, 792-797 (1947).

12. L. Li and J.A. Dobrowolski, “Visible broadband, wide-angle, thin-film multilayer polarizing beam splitter,” Appl. Opt. **35**, 2221-2225 (1996).

13. L. Li and J. A. Dobrowolski, "High-performance thin film polarizing beam splitter operating at angles greater than the critical angle," Appl. Opt. **39**, 2754-2771 (2000).

14. L. I. Epstein, "The design of optical filters," J. Opt. Soc. Am. **42**, 806-810 (1952).

15. M. C. Ohmer, "Design of three-layer equivalent films," J. Opt. Soc. Am. **68**, 137-139 (1978).

16. R. M. A. Azzam and N. M. Bashara, *Ellipsometry and Polarized Light* (North-Holland, 1987).

17. D. Clarke and J. F. Grainger, *Polarized Light and Optical Measurement* (Pergamon, 1971).

18. J. M. Bennett, "A critical evaluation of rhomb-type quarterwave retarders," Appl. Opt. **9**, 2123-2129 (1970).

19. R. M. A. Azzam and C. L. Spinu, "Achromatic angle-insensitive infrared quarter-wave retarder based on total internal reflection at the Si-SiO_2 interface," J. Opt. Soc. Am. A **21**, 2019-2022 (2004).

20. E. Spiller, "Totally reflecting thin-film phase retarders," Appl. Opt. **23**, 3544-3549 (1984).

21. E. Cojocaru, R. Dabu, V. Draganescu, T. Julea, and F. Nichitiu, "Achromatic thin-film totally reflecting quarterwave retarders," Appl. Opt. **28**, 211-212 (1989).

22. E. Cojocaru, T. Julea, and F. Nichitiu, "Infrared thin-film totally reflecting quarter-wave retarders," Appl. Opt. **30**, 4124-4125 (1991).

23. A.-R. M. Zaghloul, R. M. A. Azzam, and N. M. Bashara, "An angle-of-incidence-tunable SiO_2-Si (film-substrate) reflection retarder for the UV mercury line λ = 2537 Å," Opt. Commun. **14**, 260 (1975).

24. S. Kawabata and M. Suzuki, "MgF_2-Ag tunable reflection retrader," Appl. Opt. **19**, 484-486 (1980).

25. R. M. A. Azzam and B. E. Perilloux, "Constraint on the optical constants of a film-substrate system for operation as an external-reflection retarder at a given angle of incidence," Appl. Opt. **24**, 1171-1177 (1985).

26. W. H. Southwell, "Multilayer coating design achieving a broadband 90^o phase shift," Appl. Opt. **19**, 2688-2692 (1980).

27. J. H. Apfel, "Graphical method to design multilayer phase retarders," Appl. Opt. **20**, 1024-1029 (1981).

28. M. M. K. Howlader and R. M. A. Azzam, "Periodic and quasiperiodic nonquarterwave multilayer coatings for 90-deg reflection phase retardance at 45-deg angle of incidence," Opt. Eng. **34**, 869-875 (1995).

29. W. H. Southwell, "Thin film transmissive phase retarders", in *Proceedings of International Conference on Lasers,* C. B. Collins, ed. (STS Press, McLean, VA, 1981), pp. 578-585.

30. R. M. A. Azzam and F. A. Mahmoud, "Tilted bilayer membranes as simple transmission quarter-wave retardation plates", J. Opt. Soc. Am. A **18**, 421-425, (2001).

31. R. M. A. Azzam and A. De, "Circular polarization beam splitter that uses frustrated total internal reflection by an embedded symmetric achiral multilayer coating," Opt. Lett. **28**, 355-357 (2003).

32. R. M. A. Azzam and C. L. Spinu, "Linear-to-circular polarization transformation upon optical tunneling through an embedded low-index film," Opt. Lett. **30**, 3183-3185 (2005).

33. R. H. Muller, "Definitions and conventions in ellipsometry," Surf. Sci. **16**, 14-33 (1996).

34. E. Spiller, "Phase conventions in thin film optics and ellipsometry," Appl. Opt. **23**, 3036-3037 (1984).

35. A. M. Kan'an and R. M. A. Azzam, "In-line quarter-wave retarders for the infrared using total refraction and total internal reflection in a prism," Opt. Eng. **33**, 2029-2033 (1994).

36. CVD, Inc., 35 Industrial Parkway, Woburn, MA 01801.

37. W. J. Tropf, M. E. Thomas, and T. J. Harris, in *Handbook of Optics*, M. Bass, E. W. Van Stryland, D. R. Williams, and W. L. Wolfe, eds. (McGraw Hill, 1995), Vol. II, Chap. 33.

38. M. Herzberger and C. D. Salzberg, "Refractive indices of infrared optical materials and color correction of infrared lenses," J. Opt. Soc. Am. **52**, 420-425 (1962).

39. R. M. A. Azzam "Thin-film beam splitter that reflects light as a half-wave retarder and transmits it without change of polarization: application to Michelson interferometer," J. Opt. Soc. Am. A **3**, 1803-1808 (1986).

VITA

Siva Reddy Perla was born in Hyderabad, India in 1979. He graduated with a Bachelor of Technology degree in Electrical Engineering from Jawaharlal Nehru Technological University, India in 2001 and Master of Science in Electrical Engineering from University of New Orleans in 2003. His areas of interest are thin film optics, ellipsometry, digital signal processing and image processing.